



저작자표시-비영리-변경금지 2.0 대한민국

이용자는 아래의 조건을 따르는 경우에 한하여 자유롭게

- 이 저작물을 복제, 배포, 전송, 전시, 공연 및 방송할 수 있습니다.

다음과 같은 조건을 따라야 합니다:



저작자표시. 귀하는 원저작자를 표시하여야 합니다.



비영리. 귀하는 이 저작물을 영리 목적으로 이용할 수 없습니다.



변경금지. 귀하는 이 저작물을 개작, 변형 또는 가공할 수 없습니다.

- 귀하는, 이 저작물의 재이용이나 배포의 경우, 이 저작물에 적용된 이용허락조건을 명확하게 나타내어야 합니다.
- 저작권자로부터 별도의 허가를 받으면 이러한 조건들은 적용되지 않습니다.

저작권법에 따른 이용자의 권리는 위의 내용에 의하여 영향을 받지 않습니다.

이것은 [이용허락규약\(Legal Code\)](#)을 이해하기 쉽게 요약한 것입니다.

[Disclaimer](#)

공학박사 학위논문

**Study on Macroscale 2D Self-assembly of
Tyrosine-containing Helical Peptide and Proton
Conduction in a Tyrosine/manganese Oxide
Hybrid Nanofilm**

타이로신을 함유한 나선형 펩타이드의 2차원 대면적
자기조립과 타이로신-망간 산화물 하이브리드 박막의 수
소이온전도에 대한 연구

2018년 8월

서울대학교 대학원

재료공학부

이재훈

Abstract

Study on Macroscale 2D Self-assembly of Tyrosine-containing Helical Peptide and Proton Conduction in a Tyrosine/manganese Oxide Hybrid Nanofilm

Jaehun Lee

Department of Materials Science and Engineering

The Graduate School

Seoul National University

One of the important challenges in the development of protein-mimetic materials is to understand the sequence specific assembly behavior and the dynamic folding change. The discovery of laterally extended, untwisted, two-dimensional assembled structures in pure water is fundamentally challenging in peptide-based systems. Until now, most of the previous approaches for preparing 2D peptide assembled structures have been based on beta-sheet-like assembly or fibril-aggregated structures. In this study we present the assembly of a designed tyrosine-rich 5-mer peptide at the air/water interface, displaying facet formation of a water droplet. The identified peptides had a strong driving force to flatten the rounded top of droplet into a plane

with a macroscopic 2D structure. The facet formation is driven by interactions of tyrosine and cross-linked stabilization by cysteine. We revealed the helical conformation of the peptide was stabilized by a disulfide bond, which was confirmed by circular dichroism and 2D-nuclear magnetic resonance spectroscopy. Furthermore, we created giant nanosheets decorated with gold nanoparticles at the air/water interface by introducing gold ion into the peptide. Due to the gold ions as an oxidant to rapidly induce a disulfide bridge between cysteines, the peptide assembled into the nanosheet and Au^{3+} were reduced to gold nanoparticles on the peptide sheet in the absence of other reducing agents simultaneously.

In an effort to investigate the potential of tyrosine-rich peptide with redox active functions, we examine proton conductivity of the peptide films hybridized with manganese oxides. Proton conduction in biological systems has been an important issue for a better understanding of fundamental life mechanism. To understand and manipulate proton conduction in bio-system, several studies have investigated bulk proton conduction of biomaterials. However, little is known about the bulk proton conductivity of short peptides and their sequence-dependent behavior. We focus on tyrosine-rich peptide which has redox-active and crosslinkable phenol. Tyrosine has been known to play a critical role in PCET interplaying with a Ca-Mn cluster in the photosystem II. Moreover, it can be polymerized into cross-linked polymers, melanin, possessing a semiconductor-like behavior dependent on hydration. Inspired from this, we made proton conductor with tyrosine containing 2D peptide material by hybridization with manganese oxide (MnO_x) via the tyrosine oxidation reaction. The peptide/ MnO_x hybrid films can efficiently transport proton and proton conductivity was 18.6 mS cm^{-1} . The value is

much higher than that of biomaterials and comparable with synthetic materials. These results suggest that peptide-based hybrid material can be a promising new class of proton conductor. In perspective of bioelectronics and further applications, it would be a good example for designing versatile platforms for bio-functionalized devices with biocompatible materials.

Keywords: Peptide, Self-assembly, 2-Dimensional Materials, Helix, Disulfide bond, Proton conductor, Hybrid Material

Student number: 2012-23150

Contents

Abstract.....	ii
Contents.....	v
List of Tables.....	ix
List of Figures.....	x
Chapter 1. Introduction.....	1
1.1 Bio-inspired peptide-based nanomaterials.....	1
1.2 The role of tyrosine in natural system.....	5
1.3 Molecular tyrosine as a redox-active link.....	15
1.4 Biomaterials developed by dityrosine cross-linking.....	23
1.5 Self-assembly of tyrosine-rich short peptide.....	29
1.6 Tyrosine-rich peptide-based hybrid functional materials.....	39
1.7 Objective of the thesis.....	44
1.8 References.....	48
Chapter 2. Macroscale 2D self-assembly of tyrosine-containing helical peptide.....	62

2.1	Introduction	62
2.2	Experimental Procedure.....	68
2.2.1	Chemicals	68
2.2.2	Peptide dimerization and facet formation.....	68
2.2.3	Facet formation time measurement	69
2.2.4	Characterization.....	70
2.2.3.1	Atomic force microscopy (AFM) analysis.....	70
2.2.3.2	Scanning electron microscopy (SEM) analysis.....	71
2.2.3.3	Transmission electron microscopy (TEM) analysis.....	71
2.2.3.4	High-performance liquid chromatography (HPLC).....	71
2.2.3.5	Electrospray ionization mass spectrometer (ESI-MS).....	73
2.2.3.6	Fourier transform infrared spectroscopy (FT-IR).....	74
2.2.3.7	Raman spectroscopy analysis.....	74
2.2.3.8	Circular dichroism (CD) spectroscopy.....	75
2.2.3.9	2-dimensional nuclear magnetic resonance spectroscopy.....	76
2.3	Results and Discussions.....	77
2.3.1	Self-assembly of YFCFY peptide	77
2.3.2	Facet formation kinetics.....	84
2.3.3	Building block of 2D self-assembly.....	88
2.3.4	Molecular conformation of YFCFY peptide.....	91
2.3.5	Hybrid 2D self-assembly of YYCYY peptide using gold ion.....	101
2.3.6	Chemical structure of YYCYY after reaction with gold ion.....	109

2.3.7	Molecular conformation of YYCYY peptide.....	112
2.4	Conclusion.....	117
2.5	References.....	119

Chapter 3. Proton conduction in a tyrosine-rich peptide/manganese oxide hybrid nanofilm.....131

3.1	Introduction	131
3.2	Experimental Procedure.....	136
3.2.1	Chemicals.....	136
3.2.2	Fabrication of peptide/MnO _x hybrid nanofilm devices.....	136
3.2.3	Characterization.....	138
3.2.3.1	Electrical Characterization	138
3.2.3.2	Atomic force microscopy (AFM) analysis.....	138
3.2.3.3	Transmission electron microscopy (TEM) analysis.....	139
3.2.3.4	X-ray photoelectron spectroscopy (XPS).....	139
3.2.3.5	Inductively coupled plasma mass spectroscopy (ICP-ms)...	139
3.2.3.6	X-ray absorption near edge structure (XANES) analysis....	140
3.2.3.7	Fourier transform infrared spectroscopy (FT-IR) analysis...141	
3.2.3.8	Thermal gravimetric analysis (TGA)	141
3.3	Results and Discussions.....	142
3.3.1	Morphology and structural analysis of the hybrid film.....	142

3.3.2	Characterizations of manganese oxides.....	147
3.3.3	Characterizations of peptide in hybrid films.....	155
3.3.4	Electrical property of hybrid films depending on humidity.....	159
3.3.5	Electrochemical impedance spectroscopy analysis.....	163
3.3.6	Deuterium kinetic isotope effect on conductivity.....	168
3.3.7	Transient current measurements	170
3.3.8	Synergistic effect on proton conduction of peptide and manganese oxides.....	174
3.4	Conclusion.....	182
3.5	References.....	185
Chapter 4. Concluding remarks.....		197
국문 초록.....		201

List of tables

Table 1.1	Facet formation of dimer depending on buffer conditions.....	80
Table 2.1	The concentration of elements in peptide/manganese oxide hybrid film.....	153

List of figures

Figure 1.1	Proton-coupled electron transfer of tyrosine.....	8
Figure 1.2	Native proteins employing dityrosine bonds.....	11
Figure 1.3	Examples of conformation formed by tyrosine in protein...	14
Figure 1.4	Thermodynamic of PCET of tyrosine.....	21
Figure 1.5	Biomimetic model system utilizing PCET.....	22
Figure 1.6	Dityrosine formation through cross-linking.....	28
Figure 1.7	Facet formation of water droplets by 2D peptide sheets.....	36
Figure 1.8	Structural analysis of the 2D assembly.....	37
Figure 1.9	Sequence-dependent polymeric peptide assembly.....	38
Figure 1.10	Self-assembling peptide scaffolds for catalysis.....	43
Figure 1.11	Tyrosine peptide-based biomimetic systems.....	47
Figure 2.1	SEM images for self-assembled structures of each peptide sequences and optical images for droplets of 80°C heated peptides.....	67
Figure 2.2	Facet formation of water droplets by 2D peptide sheets.....	79
Figure 2.3	Morphology of dimer sheets and monomer films.....	81
Figure 2.4	TEM images of the peptide sheets.....	82
Figure 2.5	Methods for transferring to substrate	83
Figure 2.6	High Performance Liquid Chromatography results.....	85
Figure 2.7	Electrospray Ionization Mass spectrum of peptide.....	86
Figure 2.8	Effect of dimer on facet formation kinetics.....	87

Figure 2.9	Raman analysis of peptide sheets.....	90
Figure 2.10	Circular dichroism analysis of YFCFY peptide.....	97
Figure 2.11	2D TOCSY NMR spectra.....	98
Figure 2.12	2D NOESY NMR spectra.....	99
Figure 2.13	NMR solution structure of YFCFY dimer peptide.....	100
Figure 2.14	Facet formation of water droplets by 2D peptide sheets and morphology of the sheets.....	105
Figure 2.15	SEM/EDS mapping images of gold nanoparticles and peptide hybrid film.....	106
Figure 2.16	Effect of gold ion concentration of facet formation.....	107
Figure 2.17	Optical image of fibrillar aggregations.....	108
Figure 2.18	Presence of oxidized tyrosines and dimer analyzed by LC/MS.....	111
Figure 2.19	Circular dichroism analysis of YYCYY peptide.....	115
Figure 2.20	FT-IR spectra of monomer peptide and film.....	116
Figure 3.1	Scheme for polymerizing process of eumelanin.....	135
Figure 3.2	Synthesis of dityrosine using KMnO_4	144
Figure 3.3	Fabrication process of hybrid film.....	145
Figure 3.4	A before-and-after comparison with KMnO_4 treatment...	146
Figure 3.5	HRTEM images of the hybrid film.....	150
Figure 3.6	X-ray absorption near edge structure spectra.....	151
Figure 3.7	Energy-dispersive X-ray spectroscopy mapping.....	152
Figure 3.8	UV-VIS spectra of peptide film and hybrid film.....	154
Figure 3.9	Photoluminescence spectra.....	157

Figure 3.10	FT-IR spectra of the peptide film and hybrid film.....	158
Figure 3.11	IV sweep plots of the hybrid film.....	161
Figure 3.12	Palladium hydride formation by H ₂ gas exposure.....	162
Figure 3.13	Typical Nyquist plots by relative humidity.....	165
Figure 3.14	Nyquist plots of the hybrid film.....	166
Figure 3.15	Calculated conductivity of the devices.....	167
Figure 3.16	Nyquist plots in the presence of water vapor or deuterium oxide vapor (RH of 80%).....	169
Figure 3.17	Transient current measurement of the devices with gold and palladium hydride electrode.....	173
Figure 3.18	Thickness of pristine peptide films and hybrid films of various concentration of KMnO ₄ solution by treatment time...	177
Figure 3.19	Conductivity of the films treated with various conditions.....	178
Figure 3.20	Result of TGA for peptide/Manganese oxide.....	179
Figure 3.21	IV sweep plots of films from YYACAYY or YFACAFY peptides at 80 %RH and calculated conductivity of hybrid films from YYACAYY or YFACAFY peptides through EIS measurements as a function of humidity.....	180
Figure 3.22	Cross-section TEM images and EDX mapping.....	181
Figure 3.23	Comparison chart about proton conductivity	184

Chapter 1. Introduction

1.1 Bio-inspired peptide-based nanomaterials

Proteins/peptides are one of the minimal biological machines which of functions are widely ranging and include molecular recognition, catalysis, replication, and mechanical responsiveness. Most peptides are encoded by DNA sequences in the genome and are constructed from 20 natural amino acids. For example, organisms such as diatoms and marine sponges use self-assembled peptides, proteins, and organic-inorganic suprastructures as templates to control nucleation and the amorphous-to-crystal phase transformation, which leads to the generation of crystals with unusual shapes and complexity in controlled size, orientation, composition and hierarchical structure from nanoscale to microscale.^{1,2,3} In the last two decades, there has been an increasing research effort focused on production of new functional structures based on peptides and their derivatives, either by copying the functions of peptide and proteins or by using totally new design rules. The resulting nanoscale materials are expected to find applications in many areas, including biomedical biomaterials and nanotechnological applications.⁴ Peptide materials have been successfully employed as a fundamental component in biomembrane, functional nanodevices, hydrogels for cell culture

and drug delivery, biosensors, functional materials with unique bio-recognition ability and as energy conversion materials. All the above functions and applications of peptide-based materials arise due to their unique structural/chemical features, enabling them to serve in an extremely vast context of fundamental and applied sciences, crossing biology to materials science and nanotechnology.⁵

The field of peptide-based materials has started in early 1990s since Zhang *et al* discovered ion complementary peptide EAK16 sequence (E:glutamic acid, K:lysine, A:alanine) that can assemble into interwoven filaments.⁶ Ion pairs present in the same chain simultaneously formed hydrophilic face while alanine residues made hydrophobic face, leading to a β -sheet structures. In 2001, Stupp's group explored a new assembling motif called peptide amphiphiles which have a hydrophilic amino acid sequence attached to a hydrophobic alkyl tail.⁷ The distinct hydrophobic interaction enabled to use a broad range choice of peptide sequences and most of the peptide amphiphiles self-assemble into cylindrical nanofibers with a β -sheet conformation. A very short assembling motif, diphenylalanine (FF), which can maximize the advantages of both easy synthesis and direct control of assembled structures was reported by Gazit's group.⁸ Aromatic FF sequence can organize into highly stable tubular nanostructures by strong pi-pi interaction. The versatility of the peptide motifs, in conjunction with their ability to form specific secondary

structures provided a unique platform for the design of nanomaterials with controllable structural features.

A number of peptide-based building blocks, such as peptide amphiphiles, ionic complementary peptides, copolypeptides, cyclic peptides, surfactant-like oligopeptides, and short dipeptide, have been designed and developed for generating supramolecular structures.⁹ Among them, FF dipeptide have drawn much attention due to unusual chemical, physical properties and a very short length of the sequence that can facilitate the expandability towards hybridization with other motif. Studies on FF sequence were inspired from the key motif of amyloid- β peptides that assemble to form amyloid plaques in the brains of Alzheimer's patients. Two consecutive phenylalanine residues in amyloid- β peptides are known as the core recognition motif due to their strong hydrophobic interactions through pi-pi stacking. The stacking interactions of FF induce highly stable nanostructures leading to unexpected features such as remarkable mechanical, electrochemical, electronic, and photochemical properties along with high thermal and chemical robustness and environmental compatibility.¹⁰ Up to now, the majority of short peptide-based materials are centered on the self-assembling of FF-based peptide sequence into a nanostructure such as fiber, tube, vesicle and hydrogels, and there are several excellent reviews that have outlined the design aspects, self-assembled morphologies and applications of such systems.

Recently, our group and Lee's group discovered a new class of assembling motif from tyrosine(Y)-rich short peptides that can assemble into macroscopic 2D nanosheets.¹¹ Being slightly different from phenylalanine having a benzene ring, tyrosine has a phenolic –OH group as a side chain functional group. In nature, tyrosine is a versatile amino acid that plays an important role in regulating the structural conformation transition of proteins and has redox-active property facilitating the interaction between metal ion in active center of enzymes and the transport of electron along with a proton simultaneously.^{12,13} In addition, it was observed that tyrosine-rich regions among all possible 7-mer sequence domains occurring in an amyloidogenic protein, β_2 -microglobulin, shows the highest assembling propensities.¹⁴ This result suggested that the tyrosine residue acts as a key motif in self-assembly process. Inspired from the fascinating characteristic of tyrosine, for the first time in 2014, we systematically constructed a peptide library comprised of short peptides with repeating tyrosine units to study the assembly behaviors and their potential applications. The exploration and evaluation of supramolecular structures with unique features based on the tyrosine-rich peptides are opening a new avenue for sequence-specific peptide-based functional materials. In this review, we will introduce the roles of tyrosine motif in natural system first and discuss several approaches adopted to mimic or utilize the function of designed tyrosine-based peptide sequences. The first section of the review will deal with the role of tyrosine in nature in aspect of electrochemical, chemical, and

structural properties. In the second category, interesting biomimetic molecular designs focused on proton-coupled electron transfer (PCET) mechanisms of tyrosine will be considered. Then, the use of chemical crosslinking between tyrosine residues towards biomaterials will be presented. We will substantially detail the tyrosine peptide-based materials from self-assembled structures to peptide/inorganic hybrid systems. Finally, a brief account of the opportunities and future challenges in design optimization and applications of tyrosine peptide-based biomimetic systems will be provided.

1.2 The role of tyrosine in natural system

1.2.1 Tyrosine as redox cofactor

Precisely controlled electron transfer processes are essential for all living organisms. In respiration and photosynthesis, electrons should be transferred long distances between proteins or across a membrane for productions of adenosine triphosphate and the conversion of carbon dioxide into carbohydrates. Complex protein/peptide assemblies manipulate the electron transfer reactions and commonly couple them to proton translocation processes to facilitate efficient charge transport. Such coupling of electron and proton transfers between donors and acceptors in proteins can avoid high energy intermediates and is designated as proton-coupled electron transfer (PCET). PCET has been introduced in 1981 to explain the basic process in which electrons and protons are transported together in a disproportionation reaction between $\text{Ru}^{\text{IV}}(\text{bpy})_2(\text{py})(\text{O})^{2+}$ and $\text{Ru}^{\text{II}}(\text{bpy})_2(\text{py})(\text{OH}_2)^{2+}$.¹⁵ Since then, the PCET mechanism has been extensively used for all reactions and half reactions that carry electrons and protons together. (Figure 1.1a)

Redox-cofactors embedded in the protein matrix are transiently oxidized and reduced, and guide a radical transport pathway. Several amino acids and their derivatives have been implicated in such processes, but the key

player is redox-active amino acid, tyrosine. Tyrosine having a redox-active phenol group has been proposed to play important roles in several kinds of enzymes including photosystem II (PS2),¹⁶ ribonucleotide reductase,¹⁷ prostaglandin synthase,¹⁸ cytochrome c oxidase,¹³ and galactose oxidase.¹⁹ (Figure 1.1b,c) In case of photosystem II, the light-induced charge separation reactions are coupled to the Mn₄Ca cluster catalyst via a tyrosine which denoted Tyr_z. (Figure 1.1b) It has a critical role as redox intermediate between the Mn₄Ca cluster and the central chlorophylls, denoted as P₆₈₀ from their lowest absorption maximum at 680 nm. Tyr_z transfers electron from the Mn₄Ca cluster to P₆₈₀ in a process of steady state oxygen evolution. When Tyr_z is oxidized, a neutral tyrosyl radical is formed by accompanying deprotonation of the phenolic oxygen. Nearby histidine (His_z) acts as a proton acceptor that is hydrogen bonded to the phenolic proton. In other words, Tyr_z prevents the recombination of excited electrons and holes in P₆₈₀ and efficiently transfers electrons from water molecule to P₆₈₀. (Figure 1.1b) When the hydrogen bond between Tyr_z and His_z is destroyed by mutational replacement, the function of Tyr_z is severely varied and often it loses the functionality. This illustrates the importance of PCET nature of tyrosine.

Inspired from the role of the tyrosine in enzymatic system and photosynthesis, numerous model studies have been conducted using the structurally defined biomimetic peptide, such as a β -hairpin Tyr-containing peptide designed de novo,²⁰ and Tyr-conjugated metal-ligand complex.²¹

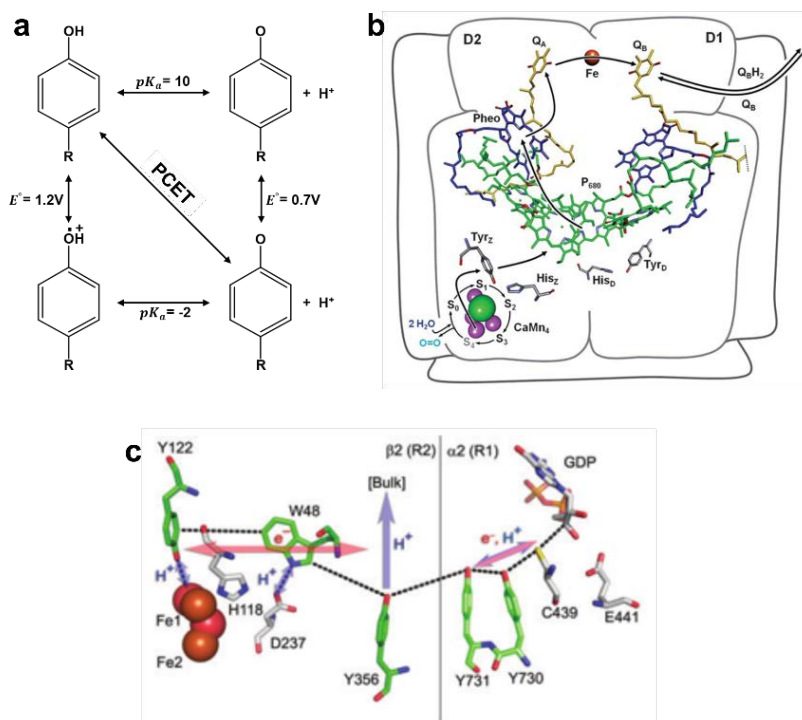


Figure 1.1 Proton-coupled electron transfer of tyrosine (a) Thermodynamic cycle for tyrosine in aqueous media (b) When light is absorbed by P680, the chain electron transfer occurs. The electron from CaMn₄ cluster is effectively transferred by redox active Tyr_z, which is coupled to its deprotonation as phenolic group becomes acidic after the oxidation so that Tyr_z forms neutral radical. (c) Residues of class 1 ribonucleotide reductase compose the PCET pathway to transport radical from Y122 in β2 to C439 in the α2 active site. Proton transfer between diiron oxo/hydroxo cofactor is coupled to orthogonal, long distance electron transfer. In addition, collinear PCET is included in the α2 active site.

1.2.2 Dityrosine as cross-linker

The phenolic chain of tyrosine and its unique chemical reactivity enable its involvement into many molecular interactions and biosynthetic transformations. This reactivity provides an efficient way to affect protein activity, including the ability to transfer electrons and to chemically graft phenol groups forming dityrosine. Such cross-linking reactions can be readily accomplished by special enzyme reactions,²² interaction with the redox active metal complex,^{23,24} radiolysis,²⁵ or photolysis.²⁶ The oxidative binding propensity of tyrosine residues has essential functions in organisms, but it also results in the pathogenic conjugation of proteins.^{26,27} These pathologies are usually part of the natural aging process, oxidative stress, and diverse pathological conditions. In biological systems, free dityrosine is not incorporated in de novo protein synthesis and has high chemical stability (unreactive to changes in oxygen/pH). Owing to these features, dityrosine has been used as an efficient biomarker that has characteristic fluorescence at 420 nm.²⁸ In spite of such potential of detrimental influences, evolution has utilized the disposition of this reaction to form a number of unique and highly specialized extracellular matrices that settle tissue structure and function.

Dityrosine chemical cross-linking stabilizes the structure of proteins and strengthens the mechanical properties in several structural tissues. (Figure

1.2) Resilin is part of a broad family of elastic proteins that includes elastin, gluten, and gliadin and provides a low stiffness, energy storage domain in areas of the cuticle that require high strains and rapid energy release.^{29,30} The elasticity, mechanical properties, and energy storage properties of resilin were first investigated due to the studies to determine the mechanism of flight of desert locusts and dragonflies.^{31,32} Weis-Fogh proposed a model that randomly coiled protein chains were covalently cross-linked and went through a substantial decrease in entropy upon straining. The theoretically proposed chemical cross-links were discovered in form of dityrosine and trityrosine polypeptides.³⁰ In addition to resilin, dityrosine residues have also been found in the structural and connective tissue such as elastin from chick aorta,³³ rabbit skin,³⁴ human aorta³⁵ and bovine skin.³⁶ and silk fibroin from caddisfly and silkworm. The prevalence of naturally occurring dityrosine in structural proteins suggests that it is the important stabilizing motif and thus worth utilizing in the development of novel biomaterials. Therefore, there have been several attempts to introduce these mechanical and structural properties into material engineering.³⁷⁻³⁹

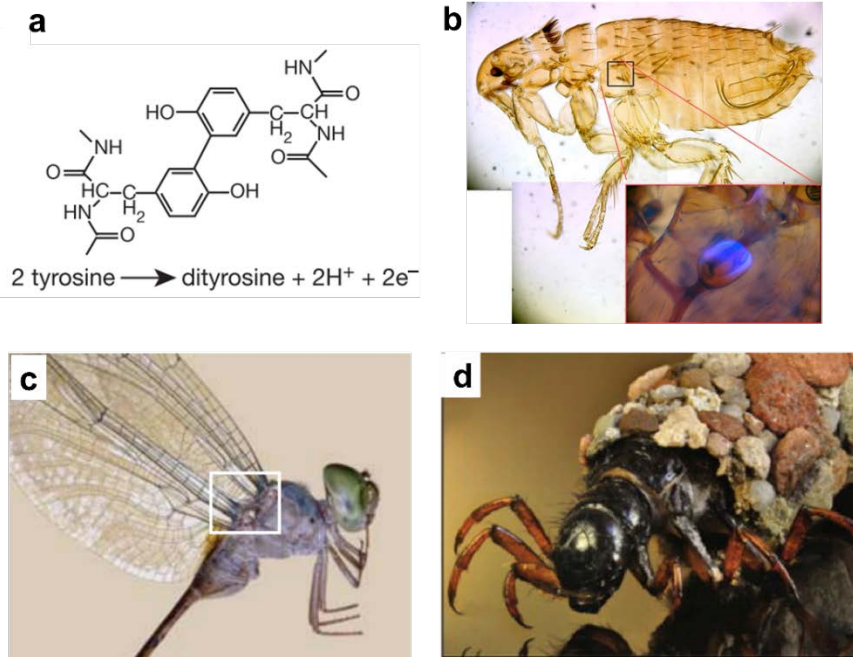


Figure 1.2 Native proteins employing dityrosine bonds. (a) Chemical structure of a dityrosine bond. (b) Highlight of location of resilin in the flea, the elastomeric protein allows the flea to jump up to 38 times of its body length (Image courtesy of CSIRO Science Images). (c) The wing tendon from adult dragonfly (*Zygomma* sp.) contains a significant amount of dityrosine rich resilin. (d) Casemaker *Hesperophylax occidentalis* fifth instar larvae within its natural stone case. The caddisfly larvae build composite shelters from adhesive silk fiber containing dityrosine-crosslinking.

1.2.3 Tyrosine as structural motif

For the process of protein folding and the determination of 3-dimensional architecture, specific sequence motif and long-range pattern of hydrophobic/hydrophilic moieties are extremely important. There has been reported particular local arrangements of sequence that prefer certain secondary structures. For example, residues that strongly prefer the N-terminal, N+1 positions at the start of a α -helix, general turn-inducing sequences, and repeat of the heptad leucine which favors the coiled-coil or leucine zipper interaction. Out of the 20 amino acids found in protein structures, tyrosine, phenylalanine, tryptophan, and histidine have aromatic as a functional group. The interactions between these aromatic residues within a protein are integral for the proper structure and function of proteins.¹⁴ Recently, sheet-forming propensities of all possible 7-mer sequence domains occurring in an amyloidogenic protein, β 2-microglobulin (β 2m), were studied and an important role in tyrosine-rich regions was discovered.⁴⁰ Interestingly, the sequences containing more tyrosine residues exhibited higher Tango score which is a well-validated algorithm to evaluate propensity of amyloid assemblies. Moreover, tyrosine cross-strand ladder influences the conformation and the rigidity of multi-layer stacking in β sheet forming protein through the pi-pi interaction between the aromatic side chain.⁴¹ (Figure 1.3a) These observation suggests the important role of tyrosine

in self-assembly process. Being different from phenylalanine, tyrosine has a phenolic –OH group that can also induce hydrogen bond. In this context, various proteins such as Greek key β -barrel protein, immunoglobulin, and fibronectin type III have the tyrosine-containing local motif called ‘tyrosine corner’. (Figure 1.3b,c) The tyrosine corner is a conformation in which a tyrosine near the beginning or end of an antiparallel β -strand makes a hydrogen bond from its phenolic –OH group to the backbone amide of tyrosine residues in nearby connection, resulting in formation of nucleus folding and its stabilization.^{12,42–44}

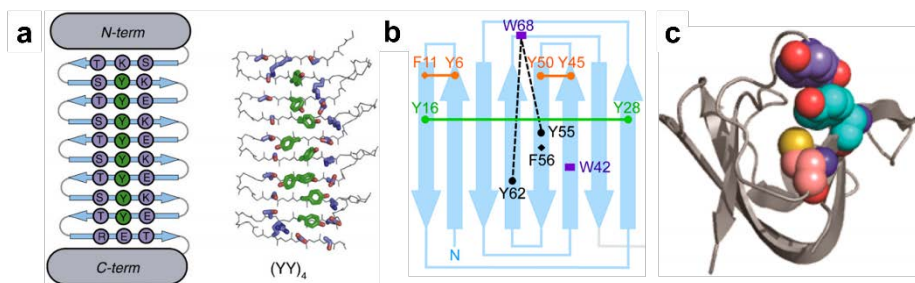


Figure 1.3 Examples of conformation formed by tyrosine in protein. (a) β -sheet conformation induced by tyrosine ladder at a large scaffold peptide self-assembly (b) Schematic of aromatic residues in γ D-Crystalline. (c) Three-dimensional structure of γ D-Crystalline N-terminal domain highlighting Y16, Y28, and C18. Ribbon structure of the N-terminal domain of γ D-Crystalline highlighting the identified key residues

1.3 Molecular tyrosine as a redox-active link

1.3.1 Proton-coupled electron transfer of tyrosine

Among various amino acids, tyrosine plays essential roles as high potential redox active cofactor in nature, for example, a hopping site for long distance electron transfer. In particular, phenol residue in tyrosine can mediate PCET process of many biological systems. PCET process in nature couples long distance electron transfer from active center of enzymes and short distance proton transfer to surrounding base. Figure 1.4 shows the thermodynamic cycle of PCET of tyrosine radical formation and the reaction diagram for both consecutive and concerted pathways. As shown in the figure, pK_a in every tyrosine oxidation pathways shows the value from 10 to -2, meaning that at most pH values, oxidation of tyrosine is coupled to proton transfer.⁴⁵

In general, PCET includes consecutive steps 'PTET (Proton Transfer Electron Transfer)' or vice versa (ETPT) and concerted proton and electron transfer (CPET). Among these, CPET is much effective due to the lower energy, single step reaction which avoids the formation of charged tyrosine species. In analogy to electron transfer reaction, CPET can be also viewed as tunneling of electron and proton at the same transition state and the rate constant can be described Eqn(1) in the same manner with Marcus theory.

$$k_{CPET} = \frac{1}{h} V_{CPET}^2 (4\pi\lambda RT)^{-1/2} \exp\left(-\frac{(\Delta G_{CPET}^\circ + \lambda)^2}{4\lambda RT}\right) \text{ where } V_{CPET} \approx V_{ET} \times V_{PT} \quad (1)$$

In Eqn(1), ΔG_{CPET}° is the reaction free energy of CPET reaction and λ is the reorganization energy of nuclear configuration to form transition state from the equilibrium state in the reaction diagram of figure 1.4b. Compared to pure electron transfer, every parameter is affected by the proton. For example, V_{CPET} is combined vibronic coupling for CPET process which is the product of electronic coupling V_{ET} and proton coupling V_{PT} .⁴⁶

Hydrogen bonding of tyrosine residue with surroundings is the key of proton transfer reaction in many biological systems and the overlap between the donor and acceptor proton vibrational wave functions strongly depends on the proton transfer distance.⁴⁷ Therefore, the mechanism of PCET strongly depends on noncovalent interactions in proteins that can modify the overall geometry.⁴⁸

PCET reactions mediated by tyrosine exist in biological systems such as PS2 and blue light receptor proteins. In both cases, hydrogen bonding is the key to determine the decay rate of tyrosine radical and if it is changed or destroyed, the nature of electron transfer significantly change. In PS2, there are two redox active tyrosines, Y161(Tyr_Z) and Y160(Tyr_D) in each D1 and D2 subunits. They have two different surrounding protein environments, making two distinct roles in electron transfer reaction. Y_Z act as redox intermediate to transfers electrons from the Mn₄Ca cluster to P₆₈₀₊ while Y_D act as a side path

electron donor at night and does not participate in electron transfer under continuous light. Both oxidation of tyrosines are coupled to proton transfer to a histidine residue. Due to extensive hydrogen bonding of Tyr_z, the electron transfer rate is much faster in Tyr_z compared to Tyr_D.^{46,48}

Importance of hydrogen bonding of tyrosine in PCET process can also be found in Blue light receptor proteins. With blue light excitation, PCET from tyrosine to Flavin form neutral Flavin/tyrosine radical pair. The reconfiguration of hydrogen bond around Flavin occurs with surrounding light and gives altered nature of PCET. In dark-adapted state, ETPT process occur where electron transfer is lagged by proton transfer while fast CPET occurs with light adapted state by increased basicity of the nearby nitrogen atom.⁴⁹

1.3.2 Biomimetic model study of PCET

It is not easy to study the detailed mechanism of PCET process in nature due to the complexity of large biological systems. However, the mechanistic insight into PCET can be a powerful tool for effective design of the powerful catalysts for water splitting and solar fuels generation by artificial photosynthesis.⁴⁷ The hydrogen bond distance and geometry are also required to be carefully controlled to optimize reaction rates at a given reaction free energy.⁴⁵ Therefore, diverse biomimetic models as a more structurally well-defined system to define a PCET reaction mechanism have been investigated.⁴⁸

As shown in figure 1.4, formation and decay of neutral tyrosine radical occurs by PCET process. At very high pH where tyrosine radical decay becomes only due to electron transfer, tyrosine radical decay rate becomes significantly faster than at lower pH. Not only surrounding pH, but also specific noncovalent interactions can control the tyrosine decay rate. Most well-known simple model to study the effect of protein environment on tyrosine radical decay rate is β hairpin maquette 'Peptide A', structure described in figure 3a. Peptide A is a designed 18-mer peptide inspired by PS2, showing pK_a of tyrosine in the strand similar to that of tyrosine in solution. Due to the peptide folding in figure 1.5a, pi-pi stacking and hydrogen bonding of tyrosine and histidine occurs, exhibiting much faster orthogonal PCET for the decay of tyrosine radical than molecular tyrosine itself. This suggest the increased electronic coupling due to noncovalent interactions between tyrosine and histidine in peptide A.⁴⁸

Many of the biomimetic model study of PCET utilize the simple platform, tyrosine attached to photosensitizer which is mostly $Ru(bpy)_3^{2+}$. As MLCT excited state Ru^{2+} is formed upon irradiation of UV light of 460 nm, it can be oxidized by oxidants in solution to form Ru^{3+} intermediate. Due to high reduction potential (1.26V vs. NHE) of Ru^{3+} , tyrosine can be oxidized to form tyrosine radical by PCET process. There are various studies using the platform, for example, to investigate the rate dependence on factors like intramolecular proton transfer distance by variety of nearby base which can alter the hydrogen

bonding nature. All of the biomimetic models suggest the stronger proton coupling and reduced reorganization energy by strong hydrogen bonding and shorter proton transfer distances facilitate the PCET reaction to form tyrosine radical and the rate can be dramatically change by small geometric differences.^{47,50}

1.3.3 Artificial photosynthesis inspired from tyrosine

A significant number of artificial photosynthetic systems inspired by high quantum efficiency of water oxidation in nature has been developed for optimization of solar energy conversion process. Not surprisingly, the key component of these structures is a phenol moiety which is the moiety in tyrosine, playing essential role in PCET process. Figure 1.5b shows one example of artificial photosynthesis reaction center with practical application of PCET of phenol moiety in water oxidizing catalyst. This bioinspired triad-1 consists of three covalently linked redox subunits and mimics both the short internal hydrogen bond and the thermal relaxation that accompanies PCET in PS2. Upon irradiation of porphyrin, electron transfer to the nanoparticle such as SnO₂ or TiO₂ in the figure 1.5b whose the dye radical cations is competent to P₆₈₀⁺ and second electron transfer from phenol moiety of benzimidazole-phenol(BiP) to porphyrin radical cation occurs. The incorporation of BiP and formation of a neutral phenoxyl radical in the artificial system significantly

improved the quantum yield for electron transfers to TiO₂ nanoparticle.^{51,52}

In Part 1.3, we summarized the role of tyrosine as redox active link. Inspired by high quantum yield of electron transfer by PCET process mediated by tyrosine, analysis on biomimetic model with the long-term goal of forming an experimental and theoretical platform for PCET process have been investigated. Moreover, for practical application of utilizing the lesson from the tyrosine PCET process in nature, lot of efforts on energy conversion field such as solar fuel cells and electrochemical devices are currently ongoing worldwide. These recent advances in constructing artificial photosynthesis reaction center inspired by tyrosine may guide more efficient catalysts design for energy production.

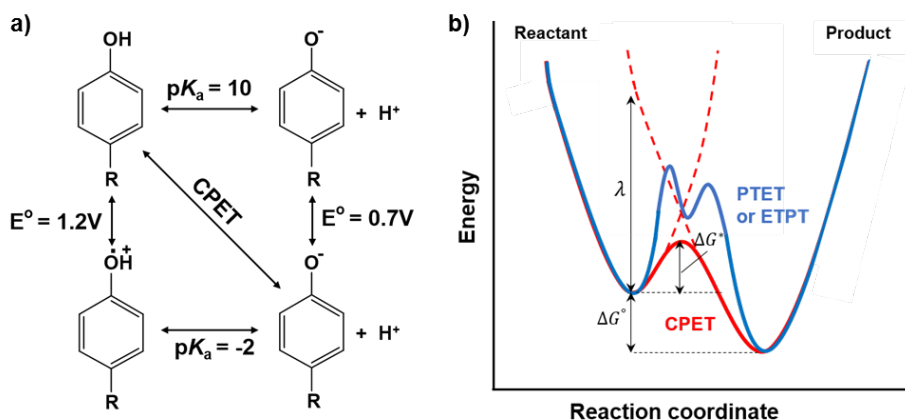


Figure 1.4. PCET system of tyrosine. (a) Thermodynamic cycle of PCET for tyrosine radical formation. The vertical and horizontal pathways show stepwise ETPT and PTET mechanisms while diagonal pathway shows the concerted proton and electron transfer which undergo directly from TyrOH to TyrO^{*}. The CPET pathway avoid charged intermediates which is advantage in low dielectric media, for example, the interior of proteins. (b) Conceptual reaction coordinate diagram for PCET process. The CPET in red line has a single transition state while PTET and ETPT in blue line have multiple transition state and high energy intermediate.

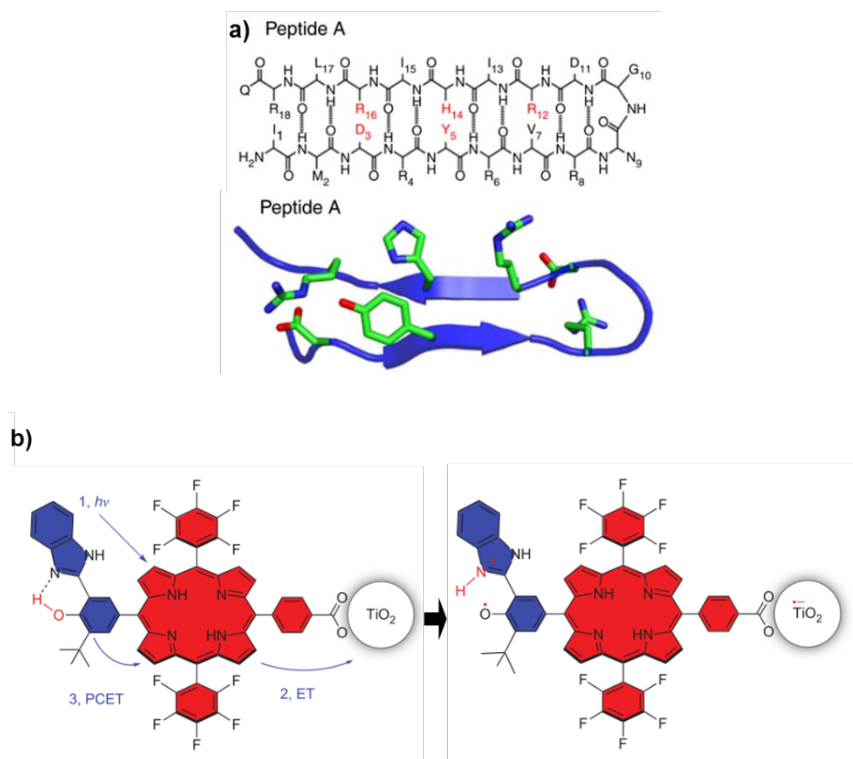


Figure 1.5. Biomimetic model system utilizing PCET. (a) Structure of β hairpin maquette Peptide A: Backbone sequence and peptide folding induces pi-pi stacking of tyrosine and histidine and indirect hydrogen bonding through water molecules. (b) Artificial system *triad-1* inspired by high quantum efficiency of water oxidation in P₆₈₀ in PS II. Upon irradiation, the system undergo a primary electron transfer and a PCET reaction.

1.4 Biomaterials developed by dityrosine cross-linking

1.4.1. Dityrosine cross-linking

Another representative potential use of tyrosine is the oxidation chemistry of the phenolic side chain. The phenol side chain of tyrosine can be oxidized to various forms such as 3,4-dihydroxyphenylalanine or eumelanin, or can participate in oxidative cross-linking with another tyrosine residue, resulting in dityrosine. Dityrosine cross-linking is frequently found in many different natural materials, such as resilin, silk, alginate, collagen, etc. The dityrosine cross-linking in these natural materials gives enhanced structural properties to the system such as resilience and high fatigue lifetime.

Resilin, which is found in the wings of dragonflies and the legs of fleas, is a representative example of dityrosine bonding utilized to increase structural stability. (Figure 1.6a) Elvin *et al* in 2005, through a photo-initiated process, showed that the cross-linking between tyrosine residues in resilin can be quantitatively controlled through a photo-initiated process, and that the cross-linking gave resilience to the protein measured through stress-strain measurements.⁵³

There have been many developments on different methods to induce dityrosine cross-linking. The usage of enzymes such as tyrosinase and

peroxidase have been developed due to their selectivity regarding side reactions and their mild reaction conditions, such as pH and temperature. The Horseradish peroxidase enzyme contain a heme group with a Fe^{3+} core, and is activated through hydrogen peroxide to form a Fe^{4+} species, which then reacts with the phenolic side chain of tyrosine, forming a tyrosine radical. The tyrosine radicals react with each other to form dityrosine bonds. Tyrosinase instead uses a complex of two copper atoms that can bind with the phenolic $-\text{OH}$, which then oxidizes into diphenyl or quinone form, forming tyrosine radical that is cross-linked with another tyrosine. The effectiveness of enzyme-base reactions sometimes stands as a drawback, for the reaction which is uncontrollably fast and so the method has limited value for casting into materials with desired dimensions.

On the other hand, many synthetic catalysts to promote cross-linking have been developed, such as Fenton-related reactions using peroxide interactions with iron ions, or photo-initiated reactions using visible light with ruthenium tris-bipyridyl ions as a catalyst.⁵⁴ The latter method has many applications in material designing due to the fact that it is driven through visible light, giving versatility to the cross-linking process into various systems. As a result, the ruthenium catalyst is widely used for the design of dityrosine-based biomaterial.

Relating to photo activation, tyrosine is oxidized upon UV irradiation through hydrogen abstraction, radical recombination, and isomerization. This

is a convenient method of preparing dityrosine without any additives, but the UV process can degrade other chromophores such as tryptophan or result in side products of tyrosine oxidation. The exact oxidation products vary in different systems and are outside the range of this review, but it is needless to say that in specific systems such as short peptides, UV irradiation is a strong tool to form tyrosine cross-linking.^{55,56}

The formation of dityrosine bonds result in significant spectroscopic changes, making the detection of tyrosine cross-linking a convenient task. Tyrosine originally has a characteristic absorption at ca. 280 nm and fluorescence emission at ca. 305 nm, due to the phenolic side group. After cross-linking, the absorption shifts to ca. 320 nm, and the emission shifts to a ca. 410 nm wavelength.⁵⁷ Although exact quantification is difficult, the fluorescence emission of dityrosine is non-destructive and convenient to detect in various situations such as in-situ, and determination of the degree of cross-linking is possible.

3.2. Material design using dityrosine cross-linking

Many material scientists have utilized dityrosine cross-linking to develop many different materials with various applications, mostly regarding mechanical properties. This approach is actively utilized in peptide-based

hydrogels, participating as a gelation factor itself or as a technique to increasing mechanical stability and functionality.

Fang *et al.*, through photochemical cross-linking a ferredoxin-like protein, constructed hydrogels with high mechanical properties and unique negative swelling behavior.⁵⁸ The method can be also utilized for short peptide-based system, and Ding *et al.* designed a peptide containing tyrosine residues with gel-forming motifs and showed that the tyrosine cross-linking resulted in increased mechanical stability.³⁷ Protein derivatives inspired from nature gives more applications and properties to the materials. Jeon *et al.* designed a light-activated mussel protein based hydrogel that can be cross-linked into hydrogels with controllable physical properties depending on the degree of cross-linking.⁵⁹ (Figure 1.6b)

The application of dityrosine cross-linking is not limited to pure peptides, but to composite biopolymers as well. For example, chitosan and hyaluronic acids can be conjugated with tyramine, a derivative of tyrosine, to form cross-linking, resulting in hydrogels that have synergetic properties such as *in vivo* gelation or tissue adhesion.^{60,61}

Many different peptide sequences are known to participate in unique self-assemblies with often ordering to the molecular level. Dityrosine cross linking can form covalent bonds between the self-assembled residues, giving it stability and functionality without destroying the orderliness of the system. Min *et al.* showed that the tyrosine-rich short peptide YYAYY can undergo cross-

linking through UV irradiation in different solvent conditions resulted in different nanostructures, a nanocapsule in aqueous media and lamella in methanol.⁶² They also showed that YYAYY can undergo photochemical cross-linking with ruthenium catalyst, resulting in nanogels that can act as a template for biomineralization through UV irradiation with metal ions.⁶³ Another usage of dityrosine cross-linking is that it can be polymerized in the self-assembled state that the peptides make. Jan et al utilized the nature of amphiphilic peptides to create self-assembled micelles, which were then cross-linked through UV irradiation, forming vesicles that are functionally applicable in various biomedical fields.⁶⁴

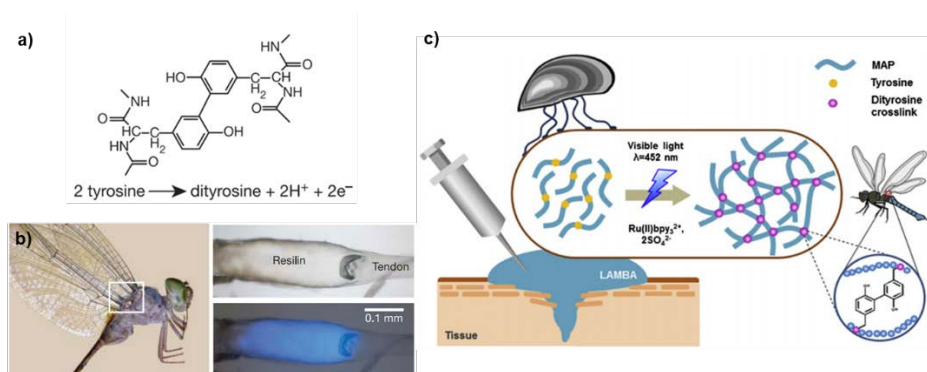


Figure 1.6. Dityrosine formation through cross-linking. (a) Chemical structure of the dityrosine. (b) Fluorescence of resilin in the wing tendon from adult dragonfly. The right panels show photomicrographs of the tendon under white light (up) and ultraviolet light (down). (c) Schematic representation of recombinant mussel adhesive proteins-based bio-adhesive formation via dityrosine bond using visible light.

1.5 Self-assembly of tyrosine-rich short peptide

1.5.1 Macroscale 2D assembly at the air/water interface

A construction of atomically defined nanoscale structures from their components represent an important challenge for the development of advanced materials. In this regard, advantages of peptide assembly to synthesize these materials are becoming more prominent in that the desired bulk properties can be exquisitely adjusted by the individual building blocks. Various peptides and their derivatives have been identified as achieving interesting hierarchical architectures, including tubes, fibers, planes, ribbons and 3D networks.^{5,65,66} The design principles mainly rely on controlling amphiphilicity, sequence periodicity, aromatic interaction and charge distribution in the assembling units. However, identifying the key amino acids for a designed assembly is a goal that is made even more difficult by structural chirality and chemical complexity. In 2014, for the first time, our group and Lee's group systematically incorporated multiple tyrosine units into peptides of various lengths (2-7 amino acids) as a design element for the construction of short peptide library to investigate the impact of tyrosine residues on self-assembly.⁶⁷ Additionally, cysteine was also inserted to confer folding stability through disulfide bridge. These peptides were self-assembled into supramolecular structures of different morphology.

Most of the screened sequences formed one dimensional fibrillar structures in aqueous solution. However, YYACAYY sequence can assemble into nanosheet in the solution. Interestingly, it was found that a facet was formed at an air/water interface of the water droplet containing YYACAYY peptide.

The faceting of a water droplet could be seen with the naked eye, and its dynamic behavior was monitored using optical camera side view observations in figure 1.7. Immediately after a water droplet containing YYACAYY was placed on a hydrophobic siliconized glass, a very thin transparent film was form on the entire surface of the droplet within a few seconds. Then, the top of the droplet was continuously flattened by the rigid sheets. The sheets could be easily transferred to a carbon grid or a silicon substrate for structural analysis by stamping the upper side of the faceted droplet. TEM analysis showed the presence of 2D nanostructures, which grew in the both lateral x-y dimensions. (Figure 1.8) AFM analysis revealed that the assembled sheets were macroscopically homogeneous and comprised of multiply stacked nanosheets with a height of 1.4 nm, confirmed by X-ray diffraction analysis. Flattening of water droplet require very high mechanical energy, which indicates that the peptide sheet was mechanically strong enough to overcome the surface pressure of the droplet. They calculated the elastic modulus of the peptide sheet using finite element analysis by counter balancing the deformation energy from the final shape of the flattened droplet. The calculated elastic modulus was at least larger than 8.0 GPa and the

nanoindentation analysis of the transferred peptide sheets showed that the measured elastic modulus was 8.4 GPa, which is stiffer than cancellous bones.

The disulfide bridge by cysteine group in YYACAYY was essential for 2D assembly. Both electrospray ionization (ESI) mass analysis and Raman spectroscopy analysis showed that the dimerization of YYACAYY was occurred during sheet assembly, implying that the building block of the assembly is a disulfide bonded dimer. The detailed molecular structure of the dimer was determined by 2D nuclear magnetic resonance (NMR) spectroscopy. The conformation of YYACAYY change from monomer to dimer was monitored and it was found that the dimer adopts a right handed alpha helical secondary structure whereas the monomer remains unfolded. As shown in figure 1.8c, the eight phenolic group of tyrosines were faced towards solvent. Additionally, the height of the dimer was ~1.4 nm, the distance from Tyr2 and Tyr6', which was close to the thickness of the sheet observed from AFM. The results also suggested that the dimers acted as building blocks.

The discovery of laterally extended and untwisted 2D assembled structures is fundamentally difficult in peptide-based system. Due to the intrinsic chirality of peptides, the backbone of peptide is mainly represented by only a single rotational state, resulting in a twist in each strand of the peptide.⁶⁸ Macroscale flatness of assembled structure constructed by β sheet motif is also restrained by propeller-like twist each β -strand. Even sheet-forming sequences can only assemble into tape-like structures without being laterally extended

over a few tens of micrometers.⁶⁹ However, the studies provide a new strategy for macroscopic peptide 2D assembly by stabilizing helical building blocks with tyrosine-rich units and disulfide bond.

1.5.2 Self-assembled nanostructures using tyrosine cross-linking

The unique feature of tyrosine-tyrosine crosslink network found in natural enzymes offers several opportunities to impart structural integrity to supramolecular assembled structure. Kim and co-workers presented a single-step covalent self-assembly of tyrosine-rich short peptide by UV irradiation.⁶² They adopted the YYAYY sequence having symmetrical tyrosine pairs at both ends to provides a high density of covalent bonds with neighboring tyrosines in proximate peptides. The morphology of the supramolecular assembled nanostructures was modulated by the selection of the reaction medium. For the synthesis of the nanocapsules, YYAYY dissolved in pH 10 buffer were irradiated with UV for 20 h. The average diameter of the assembled hollow capsules was 155.1 ± 46.13 nm and the thickness of the shell was 2.5 ± 1.3 nm, which was analyzed by dynamic light scattering and TEM respectively. When the reaction medium was changed into methanol with 0.1 M NaOH, YYAYY formed free-standing thin film after UV treatment. The assembled films were wrinkle-free, several micrometers long along lateral direction, and

4 nm thick. The evidences of crosslinking and dityrosine formation were investigated by various spectroscopic and imaging techniques. As explained in the previous chapter, the dityrosine is known to have absorption at ~330 nm and emission at ~410 nm. When the UV irradiation was kept on the solution containing YYAYY, the absorption intensity at ~330 nm and blue fluorescence at 410 nm gradually increased. It is noteworthy that the formation of tyrosyl radical increases with higher pH and crosslinking of tyrosine by UV irradiation occurs only after the deprotonation of phenol residue ($pK_a \sim 10.0$).⁵⁶ The mechanical properties of this covalently self-assembled film were investigated through nanoindentation measurement. The measured elastic modulus of ~30 GPa is higher than previously reported tyrosine-mediated assembled nanosheets and several biological proteinaceous materials.⁷⁰⁻⁷² The peptide films retained their structure ever after exposure to harsh acidic condition of 1 M HCl for a day. These chemical and mechanical stability of the assembled structure would be originated from the existence of the dityrosine cross-link, which allows the protein to be mechanically stable, elastic and resistant to proteolysis in natural system.

In addition to the UV induced-crosslinking chemistry, enzymatic catalysis of tyrosine provides not only dityrosine formation but further polymerization reaction into melanin-like supramolecular polymeric materials. Recently, Ulijn and co-workers reported the use of tyrosine-containing tripeptides as tunable precursor for self-assembly and polymeric materials.⁷³

(Figure 1.9) They first designed tripeptides composed of tyrosine, phenylalanine, and aspartic acid (D) to investigate the sequence-dependent assembly behavior. After heating the aqueous solution containing each peptide and subsequent cooling to room temperature, the six peptides show distinctive assembled structures such as needle-like crystalline fibers, nano-fibrils, and amorphous aggregates. Then, they directly introduced tyrosinase which can oxidize tyrosine into eumelanin to the assembled structures for the synthesis of polymeric pigment materials.⁷⁴ Interestingly, color changes appear for all tripeptides and the products shows very different colors, suggesting that the degree of polymerization varies greatly depending on the sequences and morphologies. The most of the resulting polymeric materials maintained their own structural frame like fiber and amorphous aggregates except the size and surface morphology. However, as shown in Figure 1.9b,c, DFY sequence was first assembled into a dense network of nanofibrils while DFY_{ox} (after enzyme treatment) polymerized into extended 2D sheets. Based on the single crystal x-ray diffraction analysis, they proposed that the anti conformation of aromatic side chains is favorable for enzymatic polymerization along the length of the β sheet but laterally between nearby fibrils, leading to destruction of fibrils and formation of extended 2D sheets. The oxidized peptides displayed variable electrochemical properties originated from tyrosine moiety. The charge storage capacity of each oxidized peptides was analyzed by electrochemical measurement to estimate the concentration of redox-active components. DFY_{ox}

2D sheets showed the highest specific charge storage capacity and this value was comparable to natural eumelanin, which is ascribed to an increase in the concentration of redox-active tyrosine-based derivatives.

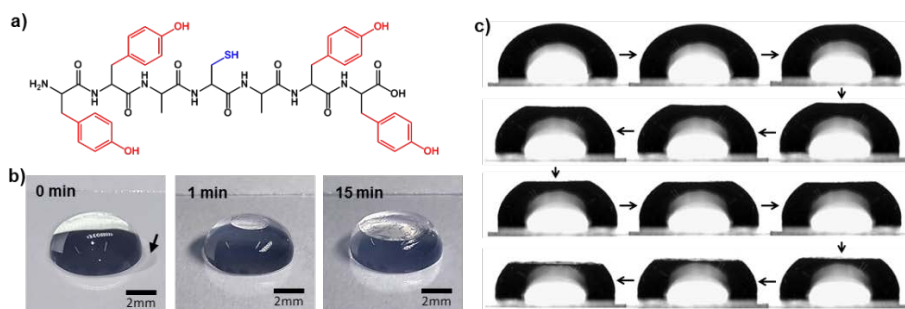


Figure 1.7. Facet formation of water droplets by 2D peptide sheets. (a) Chemical structure of YYACAYY peptide. (b) Optical images of the water droplet with the passage of time. (c) Optical microscopy images of a water droplet at different incubation times. The shape evolution of the droplet was monitored at the side.

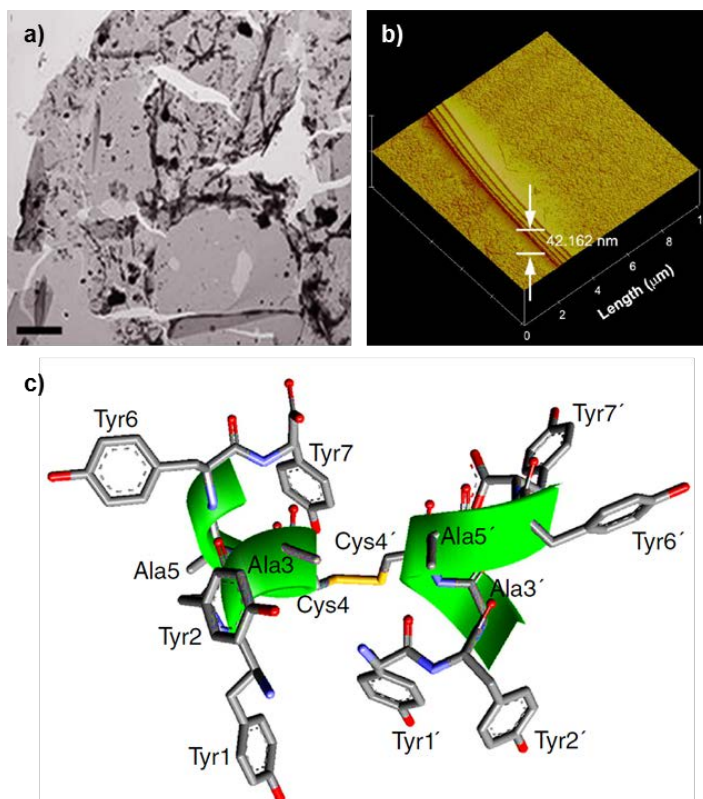


Figure 1.8. Structural analysis of the 2D assembly. (a) TEM and (b) AFM images of macroscale 2D sheets. (c) Lowest energy NMR structure of dimer YYACAYY

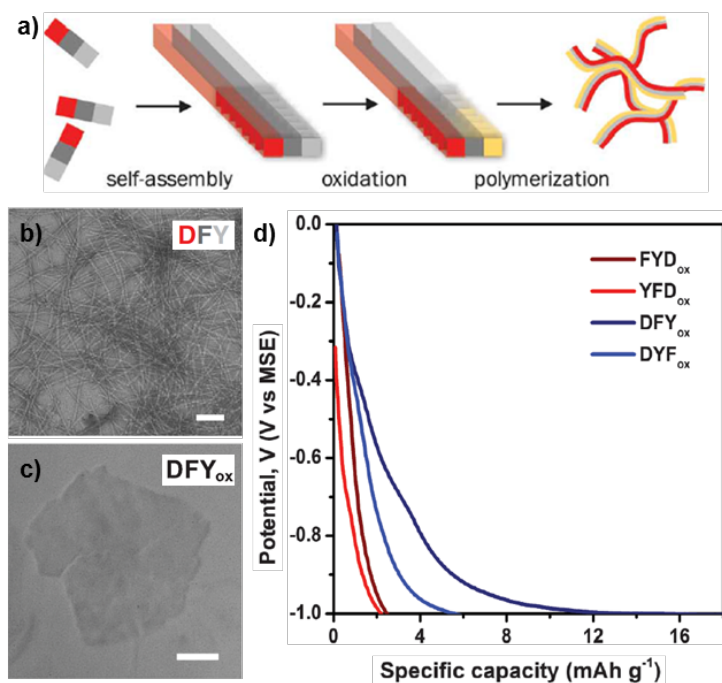


Figure 1.9. Sequence-dependent polymeric peptide assembly. (a) Schematic representation of controlled formation of polymeric peptide pigments by enzymatic oxidation and further polymerization of preorganized tripeptides. TEM images of structures formed by DFY peptide (b) before enzymatic oxidation and (c) after the reaction (d) Electrochemical potential profiles of polymeric peptide pigments.

1.6 Tyrosine-rich peptide-based hybrid functional materials

Owing to their attractive properties in aspect of functional flexibility and atomically defined nanostructures, peptides with specific sequences are gradually being designed to establish new biomaterials. With a view to enrich applications of peptide materials and expect synergetic effects between inorganic and peptide system, several hybrids materials have been developed.⁷⁵⁻⁷⁷ In this part, we will focus on the tyrosine-rich peptide-based hybrid system that can utilize the redox-activity and pi-pi interaction of tyrosine to synthesize functional materials towards catalysis and energy applications.

1.6.1 Self-assembling peptide scaffolds for catalysis and biomineralization

One potential application of tyrosine-containing peptide assembly is to use as redox-active scaffold for enzyme mimetic catalyst. Our group and Lee' explored the possibility to exploit tyrosyl radical and YYACAYY nanosheets for pyrrole polymerization reaction.⁶⁷ At first, the *in-situ* generation of tyrosyl radical in the peptide sheets was confirmed by oxidation peak from cyclic voltammetry curve. Generally pyrrole polymerization can be initiated by applying a potential ~ 0.9 V, but it requires much higher potential to get

macroscale deposition of polypyrrole.⁷⁸ As shown in figure 1.10a, when a potential of 0.9 V was applied constantly to the sheet on a fluorine-doped tin oxide (FTO) substrate and bare FTO substrate respectively, the current density of the peptide sheet/FTO sample significantly increased than that of the pure FTO sample and the macroscale black polypyrrole was synthesized. As a further step, they demonstrated that treatment of the YYACAYY sheet with copper (II) ion could act as a pyrrole polymerization catalyst without any applied electrical potential. However, solutions of copper (II) with tyrosine monomer could not produce polypyrrole. These results indicated that the assembled YYACAYY sheets with metal ion play a critical role in pyrrole oxidation reaction.

Tyrosine usually enables reduction of metal ion precursor due to the high redox potential of phenolic group without chemical reducing agent and a hydroxyl group in the phenol also can interact with metal ion.^{79–81} The interactions have been utilized to construct metal-peptide hybrid structures through biomineralization. Kim and co-workers exploited semi-permeable, fluorescent peptide nanogel with a high density of tyrosine for a nano-bioreactor, allowing the formation of uniform metal-peptide hybrids.⁶³ The peptide nanogel was prepared using YYAYY sequence with UV treatment to induce dityrosine crosslinking chemistry. The average diameter and surface morphology of the nanogel was controlled by the concentration of peptide monomer and irradiation time, from ~130 nm to ~315 nm. The metal-peptide

hybrid nanogel was easily prepared by dispersing the nanogel into aqueous AuCl₃ solution. Scanning transmission electron microscope (STEM) analysis clearly showed that discrete and uniformly sized gold nanoparticles were scattered in the nanogel without aggregation. (Figure 1.10b) Additionally, the hybrid nanogel had catalytic ability to reduce *p*-nitrophenol to *p*-aminophenol. (Figure 1.10c) In a similar way, Paribok *et al* reported that silver nitrate can be reduced to silver nanoparticle without any chemical reductant on the tyrosine-rich peptide nanofilm fabricated by Langmuir-Blodgett or Langmuir-Schaefer deposition methods.⁸²

1.6.2 Tyrosine-rich peptide-based hybrid materials for energy applications

The ability of tyrosine to reduce metal ion, synthesize inorganic nanomaterials, and strongly interact with sp² carbons materials through pi-pi interaction provide fascinating approaches to the tyrosine-based hybrids materials. In particular, assembly of carbon nanoelectrodes with biological components has been drawing much attention for several sensor applications.⁸³⁻
⁸⁵ Self-assembled peptide nanostructures can offer good templates with nondestructive and specific interactions with targeted materials by tuning the functional group of the sequence. On the purpose of fabrication of

nanoelectrodes involving carbon nanotube and silver nanoparticle, self-assembled tyrosine-rich peptide nanofibers (TPF) was synthesized as a versatile biological glue.⁸⁶ The TPF were mixed with aqueous silver nitrate to directly decorate silver nanoparticle (AgNP) on the surface of the nanofibers. Then, the coupling of the AgNP-decorated nanofibers with single wall nanotube (SWNT) was exploited by simply mixing those two components in water with anionic surfactant. During the dialysis process to eliminate unreacted residues, the freestanding composite SWNT-AgNP-decorated film was formed, which were composed of interweaved nanomesh network. Then, they investigated the use of the hybrid films for electrochemical sensor application. The electrochemical catalytic activity was screened by standard redox molecule, $K_3[Fe(CN)_6]$. The oxidation and reduction currents of the redox molecule with the hybrid film were highly increased relative to bare gold electrode and the only SWNT-decorated film. This results can be originated from reduced tunneling length and increased surface area with active site in the presence of grown AgNPs on the films. The study provides new potential applications of tyrosine-rich peptide based hybrid nanostructure as a unique biomaterial for energy device.

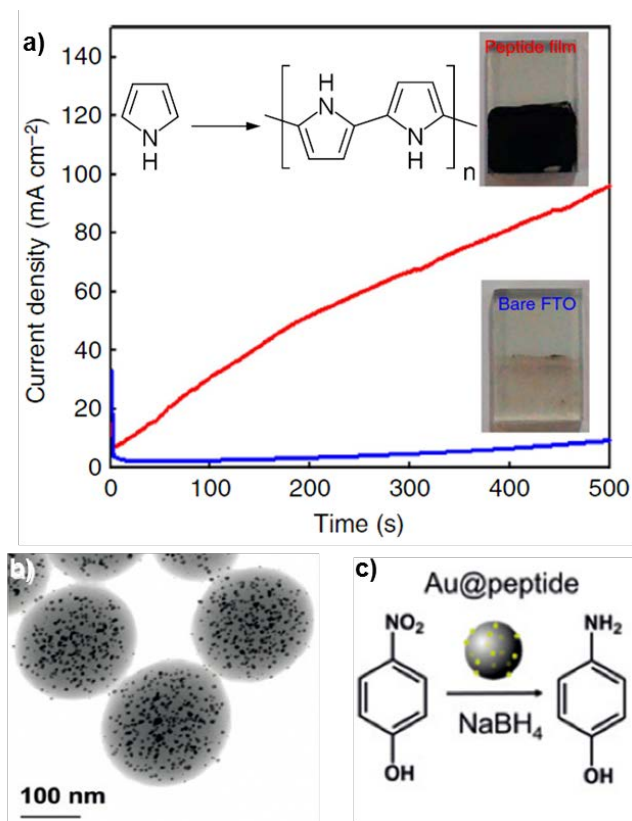


Figure 1.10. Self-assembling peptide scaffolds for catalysis. (a) The current density profiles of the YYACAYY peptide sheet (red) and tyrosine monomer (blue) deposited in FTO substrates during bulk electrolysis at 0.9 V in 0.1 M NaCl containing 50mM pyrrole. After 30 min of electrolysis, remarkably different kinetics in polypyrrole formation could be confirmed by the color change on the substrate (inset). (b) Representative STEM image of the AuNP and YYAYY peptide hybrid nanogel. (c) Catalytic reduction of *p*-nitrophenol to *p*-aminophenol by the hybrid nanogel.

1.7 Objective of the thesis

Biomimetic peptide engineering is a powerful tool to create diversity and functionality for new biomaterials of several nanostructures. In fact, natural systems provide various nanostructures as templates as in the cases of enzymes, viruses, antibodies, and others. The aim of the thesis is the development of biomimetic peptide materials based on short tyrosine-rich peptides. Peptides can offer an excellent alternative to natural protein-based systems due to their ease of synthesis, modular and tunable functionality, ability to associate spontaneously, and biocompatibility and biodegradability. Self-assembled peptide nanostructures have been increasingly exploited as promising functional materials over the past two decades. Various rational design strategies have been investigated and led to an extensive range of self-assembled nanoscale morphologies varying from fibrils to vesicles and 3D hydrogel matrices. These have paved the way for applications in several areas including biomedical sciences, electronics, optics, templates for nanotechnology. Our research has focused on the use of tyrosine, one of the significant amino acids in biological processes. It can store mechanical energy by protein folding, facilitate proton-coupled electron transport in several enzymes, and also strongly influence the assembly behavior by π - π interaction and hydrogen bonding through functional phenolic groups. To mimic the roles

of tyrosine in nature, I concentrated on two subjects; (1) investigation of rational design rule for macroscale 2D self-assembly (2) development of new type of the peptide-based hybrid materials utilizing redox-active tyrosine. We pioneered the field of tyrosine-rich peptide-based materials for generation of macroscale homogeneous 2D nanostructure and proton conducting nanofilm that have never been made before. Inspired by biomolecular interaction between peptide and inorganic components, we also have made a breakthrough in limit of bulk proton conductivity of biomaterials through the synergetic effect between tyrosine and inorganic nanoparticles.

In part I, I demonstrated the 2D self-assembly behaviors of a pentapeptide on the surface of a water droplet. Interestingly, the dimerization process through disulfide bond changes the morphology of the assembled structures from fibrils to giant sheets and also accelerates the facet formation kinetics at the air/water interface. Based on 2D NMR and circular dichroism analysis, it was found that the disulfide bond between the monomers stabilizes the helical conformation, resulting in strong molecular interactions and reinforced mechanical strength of the assembled structure. Our results provide insight into the effect of short peptide folding on macroscale self-assembly. In addition, interaction between tyrosine/cysteine and inorganic ion was investigated. Based on redox chemistry between gold ions and the pentapeptide, we found redox-mediated 2D peptide assembly and by applying this principle, we created giant nanosheets decorated with gold nanoparticles at the air/water

interface. The disulfide bond generated by gold atoms fixed two alpha helix structures and the tyrosine-rich peptide induced further arrangement of the helix, which in turn produced a rigid organic–inorganic hybrid structure.

In part II, new type of the peptide-based hybrid materials has been addressed as a new proton conducting nanofilm. Proton conduction in biological systems has been an important issue for a better understanding of fundamental life processes. Earlier research on proton transfer in bio-systems usually focused on structural components at the molecular scale and suggested that exquisitely assembled water-wires and redox cofactors are indispensable to moving protons efficiently and selectively. In this part, we focused on the role of tyrosine in PCET and hydrophilic manganese oxide particles toward proton conduction when they were hybridized into nanoscale range. Regarding the redox property of tyrosine, high valence manganese component was reacted with spin-coated nanofilm of tyrosine-rich peptide. The redox reaction induced crosslinking of tyrosine and hybridization with manganese oxide simultaneously. The hybrid film showed highly humidity-dependent conductivity. Based on electrochemical impedance spectroscopy analysis and deuterium oxide isotope experiment, it was confirmed that the main charge carrier of the hybrid film was a proton.

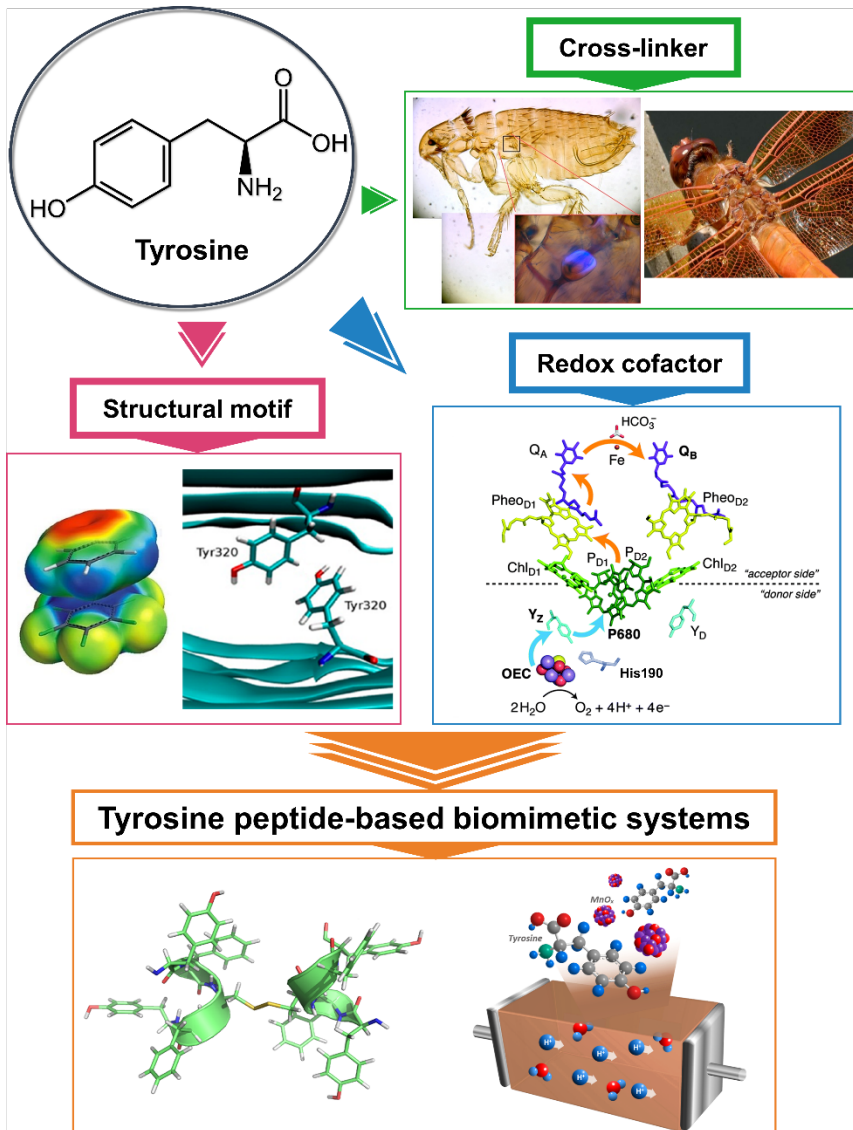


Figure 1.11. Tyrosine peptide-based biomimetic systems.

1.4 References

1. Aizenberg, J. Direct Fabrication of Large Micropatterned Single Crystals. *Science* (80-.). **2003**, *299*, 1205–1208.
2. Losic, D.; Mitchell, J. G.; Voelcker, N. H. Diatomaceous Lessons in Nanotechnology and Advanced Materials. *Adv. Mater.* **2009**, *21*, 2947–2958.
3. De La Rica, R.; Matsui, H. Applications of Peptide and Protein-Based Materials in Bionanotechnology. *Chem. Soc. Rev.* **2010**, *39*, 3499–3509.
4. Cherny, I.; Gazit, E. Amyloids: Not Only Pathological Agents but Also Ordered Nanomaterials. *Angew. Chemie - Int. Ed.* **2008**, *47*, 4062–4069.
5. Wei, G.; Su, Z.; Reynolds, N. P.; Arosio, P.; Hamley, I. W.; Gazit, E.; Mezzenga, R. Self-Assembling Peptide and Protein Amyloids: From Structure to Tailored Function in Nanotechnology. *Chem. Soc. Rev.* **2017**, *46*, 4661–4708.
6. Zhou, J.; Li, J.; Du, X.; Xu, B. Supramolecular Biofunctional Materials. *Biomaterials* **2017**, *129*, 1–27.

7. Kim, S.; Kim, J. H.; Lee, J. S.; Park, C. B. Beta-Sheet-Forming, Self-Assembled Peptide Nanomaterials towards Optical, Energy, and Healthcare Applications. *Small* **2015**, *11*, 3623–3640.
8. Richardson, J. S. β -Sheet Topology and the Relatedness of Proteins. *Nature* **1977**, *268*, 495–500.
9. Sharma, V.; Enkavi, G.; Vattulainen, I.; Róg, T.; Wikström, M. Proton-Coupled Electron Transfer and the Role of Water Molecules in Proton Pumping by Cytochrome *c* Oxidase. *Proc. Natl. Acad. Sci.* **2015**, *112*, 2040–2045.
10. Anjana, R.; Vaishnavi, M. K.; Sherlin, D.; Kumar, S. P.; Naveen, K.; Kanth, P. S.; Sekar, K. Aromatic-Aromatic Interactions in Structures of Proteins and Protein-DNA Complexes: A Study Based on Orientation and Distance. *Bioinformation* **2012**, *8*, 1220–1224.
11. Binstead, R. A.; Meyer, T. J. H-Atom Transfer between Metal Complex Ions in Solution. *J. Am. Chem. Soc.* **1987**, *109*, 3287–3297.
12. Meyer, T. J.; Huynh, M. H. V; Thorp, H. H. The Possible Role of Proton-Coupled Electron Transfer (PCET) in Water Oxidation by Photosystem II. *Angew. Chemie - Int. Ed.* **2007**, *46*, 5284–5304.
13. Argirević, T.; Riplinger, C.; Stubbe, J. A.; Neese, F.; Bennati, M. ENDOR Spectroscopy and DFT Calculations: Evidence for the

- Hydrogen-Bond Network within A2 in the PCET of E. Coli Ribonucleotide Reductase. *J. Am. Chem. Soc.* **2012**, *134*, 17661–17670.
14. Tsai, A. L.; Kulmacz, R. J. Prostaglandin H Synthase: Resolved and Unresolved Mechanistic Issues. *Arch. Biochem. Biophys.* **2010**, *493*, 103–124.
 15. Whittaker, J. W. Free Radical Catalysis by Galactose Oxidase. *Chem. Rev.* **2003**, *103*, 2347–2363.
 16. Pagba, C. V.; McCaslin, T. G.; Veglia, G.; Porcelli, F.; Yohannan, J.; Guo, Z.; McDaniel, M.; Barry, B. A. A Tyrosine-Tryptophan Dyad and Radical-Based Charge Transfer in a Ribonucleotide Reductase-Inspired Maquette. *Nat. Commun.* **2015**, *6*.
 17. Sjödin, M.; Styring, S.; Wolpher, H.; Xu, Y.; Sun, L.; Hammarström, L. Switching the Redox Mechanism: Models for Proton-Coupled Electron Transfer from Tyrosine and Tryptophan. *J. Am. Chem. Soc.* **2005**, *127*, 3855–3863.
 18. Brown, K. C.; Yang, S. H.; Kodadek, T. Highly Specific Oxidative Crosslinking of Proteins Mediated by a Nickel-Peptide Complex. *Biochemistry* **1995**, *34*, 4733–4739.
 19. Atwood, C. S.; Perry, G.; Zeng, H.; Kato, Y.; Jones, W. D.; Ling, K.

- Q.; Huang, X.; Moir, R. D.; Wang, D.; Sayre, L. M.; *et al.* Copper Mediates Dityrosine Cross-Linking of Alzheimer's Amyloid- β . *Biochemistry* **2004**, *43*, 560–568.
20. Yzed, M. Oxidation of Free Amino Acids and Amino Acid Metal-Catal Yzed. **1993**.
21. Lehrer, S. S.; Fasman, G. D. Ultraviolet Irradiation Effects in Poly-L-Tyrosine and Model Compounds. Identification of Bityrosine as a Photoproduct. *Biochemistry* **1967**, *6*, 757–767.
22. Hensley, K.; Maitt, M. L.; Yu, Z.; Sang, H.; Markesbery, W. R.; Floyd, R. A. Electrochemical Analysis of Protein Nitrotyrosine and Dityrosine in the Alzheimer Brain Indicates Region-Specific Accumulation. *J. Neurosci.* **1998**, *18*, 8126–8132.
23. Barber, S. C.; Shaw, P. J. Oxidative Stress in ALS: Key Role in Motor Neuron Injury and Therapeutic Target. *Free Radic. Biol. Med.* **2010**, *48*, 629–641.
24. DiMarco, T.; Giulivi, C. Current Analytical Methods for the Detection of Dityrosine, a Biomarker of Oxidative Stress, in Biological Samples. *Mass Spectrom. Rev.* **2007**, *26*, 108–120.
25. Gosline, J.; Lillie, M.; Carrington, E.; Guerette, P.; Ortlepp, C.; Savage, K. Elastic Proteins: Biological Roles and Mechanical

- Properties. *Philos. Trans. R. Soc. B Biol. Sci.* **2002**, *357*, 121–132.
26. Andersen, S. O. The Cross-Links in Resilin Identified as Dityrosine and Trityrosine. *BBA - Gen. Subj.* **1964**, *93*, 213–215.
27. Weis-Fogh, T. Molecular Interpretation of the Elasticity of Resilin, a Rubber-like Protein. *J. Mol. Biol.* **1961**, *3*, 648–667.
28. Weis-Fogh, T. A Rubber-like Protein in Insect Cuticle. *J. Exp. Biol.* **1960**, *37*, 889–907.
29. Keeley, F. W.; Labella, F. S. Amino Acid Composition of Elastin in the Developing Chick Aorta. *Connect. Tissue Res.* **1972**, *1*, 113–119.
30. Malanik, V.; Ledvina, M. The Content of Dityrosine in Chick and Rabbit Aorta Proteins. *Connect. Tissue Res.* **1979**, *6*, 235–240.
31. Leeuwenburgh, C.; Rasmussen, J. E.; Hsu, F. F.; Mueller, D. M.; Pennathur, S.; Heinecke, J. W. Mass Spectrometric Quantification of Markers for Protein Oxidation by Tyrosyl Radical, Copper, and Hydroxyl Radical in Low Density Lipoprotein Isolated from Human Atherosclerotic Plaques. *J. Biol. Chem.* **1997**, *272*, 3520–3526.
32. Eyre, D. R.; Paz, M. A.; Gallop, P. M. Cross-Linking in Collagen and Elastin. *Annu. Rev. Biochem.* **1984**, *53*, 717–748.
33. Ding, Y.; Li, Y.; Qin, M.; Cao, Y.; Wang, W. Photo-Cross-Linking

- Approach to Engineering Small Tyrosine-Containing Peptide Hydrogels with Enhanced Mechanical Stability. *Langmuir* **2013**, *29*, 13299–13306.
34. Liao, S. W.; Yu, T. Bin; Guan, Z. De Novo Design of Saccharide-Peptide Hydrogels as Synthetic Scaffolds for Tailored Cell Responses. *J. Am. Chem. Soc.* **2009**, *131*, 17638–17646.
35. Jin, R.; Hiemstra, C.; Zhong, Z.; Feijen, J. Enzyme-Mediated Fast in Situ Formation of Hydrogels from Dextran-Tyramine Conjugates. *Biomaterials* **2007**, *28*, 2791–2800.
36. Kang, S.; Yang, J. E.; Kim, J.; Ahn, M.; Koo, H. J.; Kim, M.; Lee, Y. S.; Paik, S. R. Removal of Intact B2-Microglobulin at Neutral Ph by Using Seed-Conjugated Polymer Beads Prepared with B2-Microglobulin-Derived Peptide (58-67). *Biotechnol. Prog.* **2011**, *27*, 521–529.
37. Biancalana, M.; Makabe, K.; Koide, A.; Koide, S. Aromatic Cross-Strand Ladders Control the Structure and Stability of β -Rich Peptide Self-Assembly Mimics. *J. Mol. Biol.* **2008**, *383*, 205–213.
38. Hemmingsen, J. M.; Gernert, K. M.; Richardson, J. S.; Richardson, D. C. The Tyrosine Corner: A Feature of Most Greek Key B-barrel Proteins. *Protein Sci.* **1994**, *3*, 1927–1937.

39. Bagby, S.; Go, S.; Inouye, S.; Ikura, M.; Chakrabartty, A. Equilibrium Folding Intermediates of a Greek Key β -Barrel Protein. *J. Mol. Biol.* **1998**, *276*, 669–681.
40. Hamill, S. J.; Cota, E.; Chothia, C.; Clarke, J. Conservation of Folding and Stability within a Protein Family: The Tyrosine Corner as an Evolutionary Cul-de-Sac. *J. Mol. Biol.* **2000**, *295*, 641–649.
41. Hammarström, L.; Styring, S. Proton-Coupled Electron Transfer of Tyrosines in Photosystem II and Model Systems for Artificial Photosynthesis: The Role of a Redox-Active Link between Catalyst and Photosensitizer. *Energy Environ. Sci.* **2011**, *4*, 2379.
42. Reece, S. Y.; Nocera, D. G. Proton-Coupled Electron Transfer in Biology: Results from Synergistic Studies in Natural and Model Systems. *Annu. Rev. Biochem.* **2009**, *78*, 673–699.
43. Zhang, M. T.; Irebo, T.; Johansson, O.; Hammarström, L. Proton-Coupled Electron Transfer from Tyrosine: A Strong Rate Dependence on Intramolecular Proton Transfer Distance. *J. Am. Chem. Soc.* **2011**, *133*, 13224–13227.
44. Pagba, C. V.; Chi, S. H.; Perry, J.; Barry, B. A. Proton-Coupled Electron Transfer in Tyrosine and a β -Hairpin Maquette: Reaction Dynamics on the Picosecond Time Scale. *J. Phys. Chem. B* **2015**, *119*,

2726–2736.

45. Mathes, T.; Zhu, J.; Van Stokkum, I. H. M.; Groot, M. L.; Hegemann, P.; Kennis, J. T. M. Hydrogen Bond Switching among Flavin and Amino Acids Determines the Nature of Proton-Coupled Electron Transfer in Bluf Photoreceptors. *J. Phys. Chem. Lett.* **2012**, *3*, 203–208.
46. Irebo, T.; Johansson, O.; Hammarström, L. The Rate Ladder of Proton-Coupled Tyrosine Oxidation in Water: A Systematic Dependence on Hydrogen Bonds and Protonation State. *J. Am. Chem. Soc.* **2008**, *130*, 9194–9195.
47. Mora, S. J.; Odella, E.; Moore, G. F.; Gust, D.; Moore, T. A.; Moore, A. L. Proton-Coupled Electron Transfer in Artificial Photosynthetic Systems. *Acc. Chem. Res.* **2018**, *51*, 445–453.
48. Megiatto, J. D.; Méndez-Hernández, D. D.; Tejeda-Ferrari, M. E.; Teillout, A.-L.; Llansola-Portolés, M. J.; Kodis, G.; Poluektov, O. G.; Rajh, T.; Mujica, V.; Groy, T. L.; *et al.* A Bioinspired Redox Relay That Mimics Radical Interactions of the Tyr-His Pairs of Photosystem II. *Nat. Chem.* **2014**, *6*, 423–428.
49. Elvin, C. M.; Carr, A. G.; Huson, M. G.; Maxwell, J. M.; Pearson, R. D.; Vuocolo, T.; Liyou, N. E.; Wong, D. C. C.; Merritt, D. J.; Dixon,

- N. E. Synthesis and Properties of Crosslinked Recombinant Pro-Resilin. *Nature* **2005**, *437*, 999–1002.
50. Fancy, D. A.; Kodadek, T. Chemistry for the Analysis of Protein–protein Interactions: Rapid and Efficient Cross-Linking Triggered by Long Wavelength Light. *Chem. Biochem.* **1999**, *96*, 6020–6024.
51. Giulivi, C.; Traaseth, N. J.; Davies, K. J. A. Tyrosine Oxidation Products: Analysis and Biological Relevance. *Amino Acids* **2003**, *25*, 227–232.
52. Kerwin, B. A.; Remmele, R. L. Protect from Light: Photodegradation and Protein Biologics. *J. Pharm. Sci.* **2007**, *96*, 1468–1479.
53. Harms, G. S.; Pauls, S. W.; Hedstrom, J. F.; Johnson, C. K. Fluorescence and Rotational Dynamics of Dityrosine. *J. Fluoresc.* **1997**, *7*, 283–292.
54. Fang, J.; Mehlich, A.; Koga, N.; Huang, J.; Koga, R.; Gao, X.; Hu, C.; Jin, C.; Rief, M.; Kast, J.; *et al.* Forced Protein Unfolding Leads to Highly Elastic and Tough Protein Hydrogels. *Nat. Commun.* **2013**, *4*, 1–10.
55. Jeon, E. Y.; Hwang, B. H.; Yang, Y. J.; Kim, B. J.; Choi, B. H.; Jung, G. Y.; Cha, H. J. Rapidly Light-Activated Surgical Protein Glue Inspired by Mussel Adhesion and Insect Structural Crosslinking.

Biomaterials **2015**, *67*, 11–19.

56. Lih, E.; Lee, J. S.; Park, K. M.; Park, K. D. Rapidly Curable Chitosan-PEG Hydrogels as Tissue Adhesives for Hemostasis and Wound Healing. *Acta Biomater.* **2012**, *8*, 3261–3269.
57. Kurisawa, M.; Chung, J. E.; Yang, Y. Y.; Gao, S. J.; Uyama, H. Injectable Biodegradable Hydrogels Composed of Hyaluronic Acid-Tyramine Conjugates for Drug Delivery and Tissue Engineering. *Chem. Commun.* **2005**, 4312–4314.
58. Min, K. I.; Yun, G.; Jang, Y.; Kim, K. R.; Ko, Y. H.; Jang, H. S.; Lee, Y. S.; Kim, K.; Kim, D. P. Covalent Self-Assembly and One-Step Photocrosslinking of Tyrosine-Rich Oligopeptides to Form Diverse Nanostructures. *Angew. Chemie - Int. Ed.* **2016**, *55*, 6925–6928.
59. Min, K. I.; Kim, D. H.; Lee, H. J.; Lin, L.; Kim, D. P. Direct Synthesis of a Covalently Self-Assembled Peptide Nanogel from a Tyrosine-Rich Peptide Monomer and Its Biomineralized Hybrids. *Angew. Chemie - Int. Ed.* **2018**, *57*, 5630–5634.
60. Huang, Y. C.; Yang, Y. S.; Lai, T. Y.; Jan, J. S. Lysine-Block-Tyrosine Block Copolypeptides: Self-Assembly, Cross-Linking, and Conjugation of Targeted Ligand for Drug Encapsulation. *Polym. (United Kingdom)* **2012**, *53*, 913–922.

61. Zhao, Y.; Yang, W.; Chen, C.; Wang, J.; Zhang, L.; Xu, H. Rational Design and Self-Assembly of Short Amphiphilic Peptides and Applications. *Curr. Opin. Colloid Interface Sci.* **2018**, *35*, 112–123.
62. Raymond, D. M.; Nilsson, B. L. Multicomponent Peptide Assemblies. *Chem. Soc. Rev.* **2018**, *47*, 3659–3720.
63. Jang, H.-S.; Lee, J.-H.; Park, Y.-S.; Kim, Y.-O.; Park, J.; Yang, T.-Y.; Jin, K.; Lee, J.; Park, S.; You, J. M.; *et al.* Tyrosine-Mediated Two-Dimensional Peptide Assembly and Its Role as a Bio-Inspired Catalytic Scaffold. *Nat. Commun.* **2014**, *5*, 3665.
64. Mannige, R. V.; Haxton, T. K.; Proulx, C.; Robertson, E. J.; Battigelli, A.; Butterfoss, G. L.; Zuckermann, R. N.; Whitelam, S. Peptoid Nanosheets Exhibit a New Secondary-Structure Motif. *Nature* **2015**, 2–9.
65. Lee, H.-E.; Lee, J.; Ju, M.; Ahn, H.-Y.; Lee, Y. Y.; Jang, H.-S.; Nam, K. T. Identifying Peptide Sequences That Can Control the Assembly of Gold Nanostructures. *Mol. Syst. Des. Eng.* **2018**, *3*, 581–590.
66. Knowles, T. P. J.; Buehler, M. J. Nanomechanics of Functional and Pathological Amyloid Materials. *Nat. Nanotechnol.* **2011**, *6*, 469–479.
67. Zhang, Y. N.; Avery, R. K.; Vallmajó-Martin, Q.; Assmann, A.; Vegh, A.; Memic, A.; Olsen, B. D.; Annabi, N.; Khademhosseini, A. A

- Highly Elastic and Rapidly Crosslinkable Elastin-Like Polypeptide-Based Hydrogel for Biomedical Applications. *Adv. Funct. Mater.* **2015**, *25*, 4814–4826.
68. Rubin, D. J.; Amini, S.; Zhou, F.; Su, H.; Miserez, A.; Joshi, N. S. Structural, Nanomechanical, and Computational Characterization of D,L-Cyclic Peptide Assemblies. *ACS Nano* **2015**, *9*, 3360–3368.
69. Scott, A.; Doeke, R.; Pim, W. J. M.; Rinat, R.; Steven, G.; Lampel, A.; Mcphee, S.; Park, H.; Scott, G. G.; Humagain, S. Polymeric Peptide Pigments with Sequence- Encoded Properties. **2017**, *1068*, 1064–1068.
70. Gao, J.; Zheng, W.; Kong, D.; Yang, Z. Dual Enzymes Regulate the Molecular Self-Assembly of Tetra-Peptide Derivatives. *Soft Matter* **2011**, *7*, 10443–10448.
71. Slocik, J. M.; Naik, R. R. Sequenced Defined Biomolecules for Nanomaterial Synthesis, Functionalization, and Assembly. *Curr. Opin. Biotechnol.* **2017**, *46*, 7–13.
72. Wang, W.; Anderson, C. F.; Wang, Z.; Wu, W.; Cui, H.; Liu, C. J. Peptide-Templated Noble Metal Catalysts: Syntheses and Applications. *Chem. Sci.* **2017**, *8*, 3310–3324.
73. Mikhalevich, V.; Craciun, I.; Kyropoulou, M.; Palivan, C. G.; Meier, W. Amphiphilic Peptide Self-Assembly: Expansion to Hybrid

- Materials. *Biomacromolecules* **2017**, *18*, 3471–3480.
74. Asavapiriyant, S.; Chandler, G. K.; Gunawardena, G. A.; Pletcher, D. The Electrodeposition of Polypyrrole Films from Aqueous Solutions. *J. Electroanal. Chem.* **1984**, *177*, 229–244.
75. Selvakannan, P. R.; Swami, A.; Srisathiyarayanan, D.; Shirude, P. S.; Pasricha, R.; Mandale, A. B.; Sastry, M. Synthesis of Aqueous Au Core-Ag Shell Nanoparticles Using Tyrosine as a PH-Dependent Reducing Agent and Assembling Phase-Transferred Silver Nanoparticles at the Air-Water Interface. *Langmuir* **2004**, *20*, 7825–7836.
76. Xie, J.; Lee, J. Y.; Wang, D. I. C.; Ting, Y. P. Silver Nanoplates: From Biological to Biomimetic Synthesis. *ACS Nano* **2007**, *1*, 429–439.
77. Si, S.; Bhattacharjee, R. R.; Banerjee, A.; Mandal, T. K. A Mechanistic and Kinetic Study of the Formation of Metal Nanoparticles by Using Synthetic Tyrosine-Based Oligopeptides. *Chem. - A Eur. J.* **2006**, *12*, 1256–1265.
78. Paribok, I. V.; Kim, Y.-O.; Choi, S. K.; Jung, B. Y.; Lee, J.; Nam, K. T.; Agabekov, V. E.; Lee, Y.-S. Tailoring a Tyrosine-Rich Peptide into Size-and Thickness- Controllable Nanofilms. **2018**, 4–10.
79. Kostianen, M. A.; Hiekkataipale, P.; Laiho, A.; Lemieux, V.;

- Seitsonen, J.; Ruokolainen, J.; Ceci, P. Electrostatic Assembly of Binary Nanoparticle Superlattices Using Protein Cages. *Nat. Nanotechnol.* **2013**, *8*, 52–56.
80. Maune, H. T.; Han, S. P.; Barish, R. D.; Bockrath, M.; Iii, W. A. G.; Rothmund, P. W. K.; Winfree, E. Self-Assembly of Carbon Nanotubes into Two-Dimensional Geometries Using DNA Origami Templates. *Nat. Nanotechnol.* **2010**, *5*, 61–66.
81. Yan, X.; Zhu, P.; Li, J. Self-Assembly and Application of Diphenylalanine-Based Nanostructures. *Chem. Soc. Rev.* **2010**, *39*, 1877.
82. Min, K. I.; Lee, S. W.; Lee, E. H.; Lee, Y. S.; Yi, H.; Kim, D. P. Facile Nondestructive Assembly of Tyrosine-Rich Peptide Nanofibers as a Biological Glue for Multicomponent-Based Nanoelectrode Applications. *Adv. Funct. Mater.* **2018**, *28*, 1–8.

Chapter 2. Macroscale 2D self-assembly of tyrosine-containing helical peptide

2.1 Introduction

The ability to design and arrange peptides with a controllable structure and chemical diversity would provide a new class of self-assembled materials with sophisticated functions. One benefits of employing peptide assembly to construct these materials is that the desired bulk properties of the materials can be adjusted by the individual building blocks.^{1,2} The range of amino acids allows for tuning to specific applications by varying the primary structure, which influences the physical/chemical properties.³ Various peptides and their analogues have been employed to prepare interesting nanostructures including fibers,⁴⁻⁷ tubes,⁸⁻¹¹ ribbons,^{12,13} vesicle,¹⁴⁻¹⁶ films,¹⁷⁻²¹ and three-dimensional networks²²⁻²⁴. The discovery of a general strategy for organizing functional peptides into stable nanostructures with desired dimension and shape is an important focus in developing peptide-based self-assembled materials.

The development of 2D soft nanomaterials occupies a fundamentally important field in materials science because they possess great advantages for lightweight, unique optoelectronic properties, and device fabrication. These

advantages offer 2D soft nanomaterials a wide range of potential applications in membrane mimetics, sensing, optoelectronics, catalysis, and biotechnology.²⁵⁻²⁷ There are some examples of such materials like graphene,²⁸ 2D polymer,^{20, 29, 30} highly anisotropic colloid,³¹ or bilayer membrane³². However, it is very difficult to get scalable nanosheets by the peptide self-assembly and transfer the sheets to other substrates. Although polypeptide-based macroscopic membranes²¹ and amyloid-protein fibril-based rigid films³³ exhibit large scale 2D structures, the former possesses inhomogeneous structures composed of bundled fibrils, and the latter can be produced only with a micrometer-scale thickness. Therefore, the development of novel peptide sequences is needed to build scalable, homogeneous 2D nanostructures and explore potential applications of peptide platforms.

Peptide is intrinsically difficult to utilize for constructing flat, macroscopic, two-dimensional structures because of its chirality. The intrinsic chirality of amino acids is regarded as critical factor tuning the handedness of their folding and supramolecular structure. For instance, peptides comprised of L-amino acid mostly form right-handed α -helix and right-handed twisted β -sheet because the left-handed ones are energetically unfavorable. Owing to the intrinsic chirality of amino acids and peptides, the backbones of peptide secondary structures are mainly represented by only single rotational state, leading to twist in each strand of peptide.³⁵ Even sheet-forming sequences can only lead to tape-like structures without being extended laterally over a few

tens of micrometers. Instead, they tend to form twisted films. For example, a peptide amphiphile containing three phenylalanine residues,³⁶ a Fmoc-FF peptide,³⁷ and α S β 1 peptide,³⁸ a fragment of α -synuclein, assemble into twisted tapes. Two-fold periodicity of hydrophobic and hydrophilic side chains is known to be a key determinant for β -sheet-forming sequences but can only produce a fiber, tube, or tape.³⁹ It is interesting that chirality of the side chain-appended α carbon plays a role in inducing a macroscopic twist in the 2D assembled structures.

As a new platform to only understand the contribution of the sequence by removing the intrinsic chirality, the Zuckermann group designed peptoid sequences with two-fold periodicity of phenyl as the hydrophobic part and amine/carboxylic acid as the hydrophilic part.²⁰ Peptoid is the peptide mimetic polymer whose side chain is located at the nitrogen atom instead of the α carbon while maintaining the peptide backbone structure. Surprisingly, atomically flat, macroscopically large, three-nanometer-thin sheet structures were assembled from the designed peptoid. Such a large and thin two-dimensional structure had never been observed for any other peptide sequence. The peptoid-based approach demonstrated that removal of the intrinsic backbone chirality is required for laterally extended assembly.⁴⁰

Previously, as an effort to control the backbone chirality and folding for 2D assembly, we explored the possibility to use α -helical sequences and disulfide-bridged dimer structures.⁴⁰ We showed that the YYACAYY sequence

can assembly into flat sheets at the air/water interface and simultaneously flatten the top of a water droplet (called faceting). According to modeling and measurements, the elastic modulus of the peptide sheets is approximately 8 GPa, which is stiffer than cancellous bones. In a previous study, we suggested that a tyrosine interaction played an important role in assembly and disulfide formation contributed to the stabilization of the secondary structure based on nuclear magnetic resonance (NMR) analysis. In an effort to understand the detailed mechanism and further generalize the assembly strategy in other peptide sequences, we added phenylalanine, which has been widely used as an assembly motif for various nanostructures. In the peptide sequence design, we intended to maximize synergistic effect of the 2D forming motif (tyrosine, Y), the strong π - π interaction motif (phenylalanine, F), and the dimer formation motif (cysteine, C). Based on the importance of cysteine in the middle of sequences and two tyrosines at the end of each sequence for facet formation, we designed five sequences (*i.e.*, YFCFY, FYCYF, YFCYF, FYCFY, FFCFF) (Figure 2.1). These five sequences were investigated, and their assembly behaviors and structures were compared.

In addition, we expanded the 2D assembly system and further hybridize with gold nanoparticles by introducing redox-mediated 2D assembly using Au^{3+} . The disulfide bond between above peptide sequences was induced by mild oxidation processes such as simple aeration or incubation in dimethyl sulfoxide at first. However, Au^{3+} can also induce disulfide bond and be reduced

by tyrosine and cysteine in a few minute, which is much faster methodology than previous mild oxidation methods.

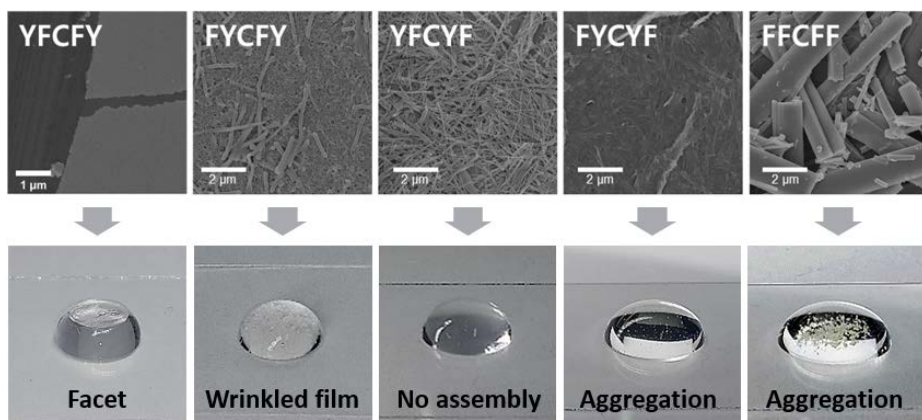


Figure 2.1 SEM images for self-assembled structures of each peptide sequences (upper) and optical images for droplets of 80°C heated peptide solutions (pictures in 10 minutes after drop, lower). Before making solutions all peptide was oxidized for 4 days to make disulfide bond between cysteines.

2.2 Experimental Procedure

2.2.1 Chemicals

All peptides (98 % purity) were purchased from GL Biochem (Shanghai, China) and used without further purifications. Other solvents were purchased from Sigma-Aldrich.

2.2.2 Peptide dimerization and facet formation

Monomer YFCFY peptide was dissolved in deionized water and its concentration was 2 mM. After the solutions in 2 ml Eppendorf tubes rendered uniformly by tip sonicating for 2 min, they were placed in a heat block at 80 °C for air oxidation. After incubation for hours the disulfide bonding was formed from sulfhydryl residues of cysteine in monomer peptides. No faceting phenomenon was observed with samples incubating time of less than 20 hours. After an extracted aliquot (80 μ L) from the enough oxidized solution was dropped on siliconized glass, faceting started within a few minutes. The average diameter of droplet was 6.4 mm.

Several concentrations of H_{Au}Cl₄ stock solution were prepared with deionized water. Monomer YYCYY peptide was dissolved in deionized water,

and its concentration was 1.6 mM. The peptide solution was placed in a heat block at 80 °C for 20 min to completely dissolve small aggregates. After incubation, different concentrations of H_{Au}Cl₄ solution were directly added to the peptide solution respectively and the final concentration of the peptide was 1.5 mM. An instantly extracted aliquot (100 μL) from the mixed solution was dropped on siliconized glass, faceting started within a few minutes. No faceting was observed under H_{Au}Cl₄ concentrations of 1 mM or above than the concentrations of 10 mM.

2.2.3 Facet formation time measurement.

As extracted 100 μL of peptide solution in certain aging time, the droplet was placed onto siliconized glass. In form of video, the faceting process was recorded immediately after dropped the solution. Facet formation time was checked when the distance between bottom (glass substrate) and film reached 2 mm.

2.2.4 Characterization

2.2.3.1 Atomic force microscopy (AFM) analysis

2 mM solutions of monomer peptides were incubated in 80 °C for air oxidation. After 4 days of incubation, an 80 µL of the solution was used for making an air/water interface film. The droplet was placed on siliconized glass for over 30 min to form a larger planar part of the peptide film. As enough time passed, film at the top part of the droplet was broken with a tweezer. Right after then surface was carefully transferred to SiO₂ coated silicon wafer (1 cm x 1 cm). This sample was immersed slowly in deionized water for washing out aggregations, and remained water on the film was removed by flowing N₂ gas gently with blower. Images of large area were observed from optical microscope (Axio Imager, Carl Zeiss, Germany) at various magnification. AFM analysis were carried out with Bruker AFM multimode 8. The used probes for AFM were Antimony doped (n) silicon cantilevers with a spring constant of 40 Nm⁻¹ (Bruker) and the resonance frequency of 300 kHz. The observation condition was tapping mode and a scan rate was 0.9 Hz. After acquiring AFM images, the thickness of film analyzed with the NanoScope Analysis program.

2.2.3.2 Scanning electron microscopy (SEM) analysis

A Zeiss Supra 55 VP (Zeiss, Oberkochen, Germany) instrument was used for SEM. Samples were prepared by stamping the water droplets containing peptide onto a silicon wafer (1 cm x 1 cm) and immediately washed with deionized water. The remaining solution was wicked out by filter paper and dried at room temperature. The samples were then coated with platinum using a Polaron SC7640 sputter coater.

2.2.3.3 Transmission electron microscopy (TEM) analysis

TEM images and selected area electron diffraction (SAED) patterns were obtained using a high resolution transmission electron microscope (JEM-3000F, JEOL, Japan) with an acceleration voltage of 200 kV. The TEM samples were collected from a faceted water droplet containing peptide.

2.2.3.4 High-performance liquid chromatography (HPLC)

For measuring a conversion degree of dimer by oxidation time, a high performance liquid chromatography (HPLC) was performed by various aging time. After preparing 2mM monomeric peptide solutions, they were placed in the 80 °C heat block. An aliquot (500 µL) of the solution was extracted every

20 hours since an oxidizing reaction started. The extracted solution was dried up by lyophilization. An instrument for chromatographic separation was HP Agilent 1100 Series (Agilent Technologies, Germany) and the experiments was carried on SunFire C-18 analytical column (100 Å, 4.6 x 250 mm, 5 µm, Waters, Milford, MA) with steady changes of the mobile phase composition during the run. Started with 90 % water and 10 % acetonitrile containing 0.1 % trifluoroacetic acid, the eluent mixing gradient linearly changed to 100 % acetonitrile in 30 minutes. The mixed eluent pumped at a flow rate of 1 mL/min. For injection, lyophilized samples dissolved in pure methanol (2mM) and injection volume was 20 µL. The retention times of monomeric and dimerized peptide were about 13.3 and 14.3 min respectively.

Sample mixtures were prepared as same as described in facet formation procedure. After mixing the YYCYY peptide solution and H₂AuCl₄ solution, the mixture solution was incubated for 10 min. An aliquot of the solution was directly injected after eliminating large aggregations with 0.22 µm syringe filter. LC-MS data sets were acquired with a liquid chromatograph (Ultimate 3000 RS system, Thermo fisher scientific Inc.) and electrospray ionization mass spectrometer (LTQ XL, Thermo fisher scientific Inc.) Analytical-scale chromatographic separations were performed with a 50.0 × 2.0 mm reversed-phase column (U-VDSpher Pur C18-E, 1.8 µm, 50 × 2.0 mm, VDS optilab), and binary solvent system made up of deionized water with 0.1% formic acid (solvent A) and acetonitrile with 0.1% formic acid (solvent B). A

linear gradient program was used that changed composition of solvent from 80% A to 0% A over 30 min at a constant flow rate 0.2 ml/min. An injection volume of 5 μ l was used. Negative mode electrospray ionization was performed using a capillary temperature of 300 °C and a source voltage of 2.7 kV.

2.2.3.5 Electrospray ionization mass spectrometer (ESI-MS)

The monomeric peptide and 4 days air oxidized peptide (2 mM, lyophilized) was dissolved in pure methanol. Equipped with autosampler and PDA-UV detector, a Thermo-Finnigan Surveyor (Thermo Scientific, USA) and ThermoFinnigan LCQ Deca XP plus ion trap mass spectrometer with ESI interface were used for the mass analysis. Ionization of analytes was carried out using electrospray ionization at 275°C of capillary temperature. The capillary voltage was set at 45 V in positive mode and -15 V in negative ionization mode with 5kV of ion source voltage. The sheath and Aux gas was set at 30 and 5units. The average scan time was 0.01 min while the average time to change polarity was 0.02 min. In order to maintain 35% abundance of the precursor ion, the collision energy (CE) level was set general value.

2.2.3.6 Fourier transform infrared spectroscopy (FT-IR)

FT-IR spectra of YYCYY (monomer or peptide films) were analyzed with a Thermo Nicolet 6,700 FT-IR spectrometer equipped with an attenuated total reflection accessory. The scanned wave numbers ranged from 750 to 3,750 cm^{-1} at a resolution of 1.93 cm^{-1} . The spectra were scanned 4 times. The peptide films on the droplet was transferred on a silicon wafer, air dried for 24 h and placed on a ZnSe/diamond. To obtain sufficient signal, 40 batches under the same condition were transferred to the substrate.

2.2.3.7 Raman spectroscopy analysis

Raman data were measured by Horiba Jobin-Yvon LabRam Aramis Raman spectrometer. A 785 nm Ar-ion laser was used as the excitation source and substrate plate was stainless steel which had no Raman signal and guaranteed a free fluorescence background. Wave numbers ranged from 200 cm^{-1} to 3000 cm^{-1} was scanned and each spectrum was accumulated for 60 seconds. The analysis was executed more than 3 points in each sample for reproducibility and reliability. To get the data of peptide film, it was transferred to the substrate and just single transfer of film provided enough signals for interpreting the Raman peaks.

2.2.3.8 Circular dichroism (CD) spectroscopy

Circular dichroism spectra of peptide solutions and peptide films were measured with J-815 spectropolarimeter (Jasco, Tokyo, Japan) at 25 °C. Spectra were collected from 260 nm to 180 nm by using a 0.1 cm path length quartz cuvette during keeping HT voltage less than 500 V for reliability. The experiment conditions were a 0.5 nm data pitch, a 20 nm/min scan speed, 16 sec response time and a 1 nm bandwidth. The data were accumulated from 3 repeated runs for reproducibility and smoothing process was done. In order to acquire conformational information of peptide films, solid circular dichroism was carried with same conditions. After faceting of a droplet was almost saturated, peptide films were transferred to quartz cuvette surface and rinsed with deionized water.

2.2.3.9 2-dimensional nuclear magnetic resonance spectroscopy

All NMR spectra were measured at 298K on Agilent DD2 600 MHz spectrometer at Korea Institute of Science and Technology. Dimethylsulfoxide (DMSO) was used to detect the gamma protons of cysteine. DMSO can also oxidize cysteines to form a disulfide bridge. The 3 mM of YFCFY peptide dissolved in 100% DMSO-d₆ was used for NMR experiments. For the assignments of amide and alpha protons, identification of sequential connectivity, and the secondary structure prediction of YFCFY, 2D COSY, 2D TOCSY, and 2D NOESY experiments were performed. For TOCSY, an MLEV-17 spinlock pulse with a mixing time of 80 ms was used. For NOESY, the mixing times of 200 and 450 ms were used. All NMR spectra were processed with VnmrJ3.2 (Agilent Technologies, Inc.), TOPSPIN 3.52 (Bruker) and NMRpipe, and visualized with Sparky software. For structural calculations of the YFCFY dimer peptide model in 100% DMSO condition, the 2D DQF-COSY (double quantum filtered correlation spectroscopy) spectrum was used for dihedral angle prediction and the 2D TOCSY and 2D NOESY spectra were used for proton assignments. The NOE restraints for structure calculation were manually obtained from the 2D NOESY spectra. The homo-dimeric YFCFY structure was calculated using CYANA 3.0 Linux software. Each monomer was linked with invisible linker residues and inter and intra NOE restraints were used for structure calculation.

2.3 Results and Discussions

2.3.1 Self-assembly of YFCFY peptide

Importantly only the YFCFY (Figure 2.2a) sequence can assemble into giant sheets with faceting (Figure 2.2b) in a similar manner to that of the previous YYACAYY sequence. Immediately after a water droplet containing the peptides was placed on a hydrophobic siliconized glass, a very thin transparent peptide film was formed on the entire surface of the droplet within a few seconds. Then, the top of the droplet was gradually flattened by rigid peptide sheets (Figures 2.2c-e). It is important to note that YFCFY can assemble in pure water but YYACAYY requires buffering conditions (Table 2.1). Additionally, one of the interesting features of YFCFY is that either a fibril-aggregated, rough film or uniformly packed, flat sheet can be formed depending on the initial status of the peptide prior to assembly.

Dimerization between YFCFY monomer was a critical parameter for determining the assembled structures and facet formation. In the sample preparation procedures, the YFCFY monomer was dissolved in deionized water, and the solution was incubated at 80°C. The incubation of the peptides promoted an oxidative reaction, resulting in the formation of YFCFY dimer due to the formation of a disulfide bond between the cysteines. Moreover, the dimer

to monomer ratio could be easily controlled by adjusting the aging time. After 20 hours of incubation, a droplet from the peptide solution produced a clear faceted surface with rigid sheets, which was influenced by the newly formed dimer. However, the YFCFY monomer only produced bumpy films at the interface (Figure 2.3f). To observe the surface of the assembled structure, the samples were prepared using a stamping method (Figure 2.4a). The sample showing rigid sheets at the interface showed 2D homogeneous structure, and the monomer films exhibited a non-uniform, wrinkled morphology (Figure 2.3d). TEM images in Figure 2.4 show macroscopically uniform morphology of dimer sheets. Direct imaging of the dimer sheet on a holey carbon grid at high magnification clearly resolved its structural integrity showing that it is not composed of entangled networks of bundled fibrils. The AFM analysis more clearly showed the differences. The dimer sheets are flat and uniform with a thickness of 10 nm. However, the monomer films are composed of bundled fibrillar fragments (Figures 2.3b,e). To estimate the actual thickness of the dimer sheets on the droplet, the sample was prepared by an extraction method (Figure 2.5b), and its thickness was determined to be nearly 150 nm (Figure 2.3c). Based on these observations, we tried to elucidate the assembly kinetics of YFCFY depending on the dimer ratio and obtain structural information.

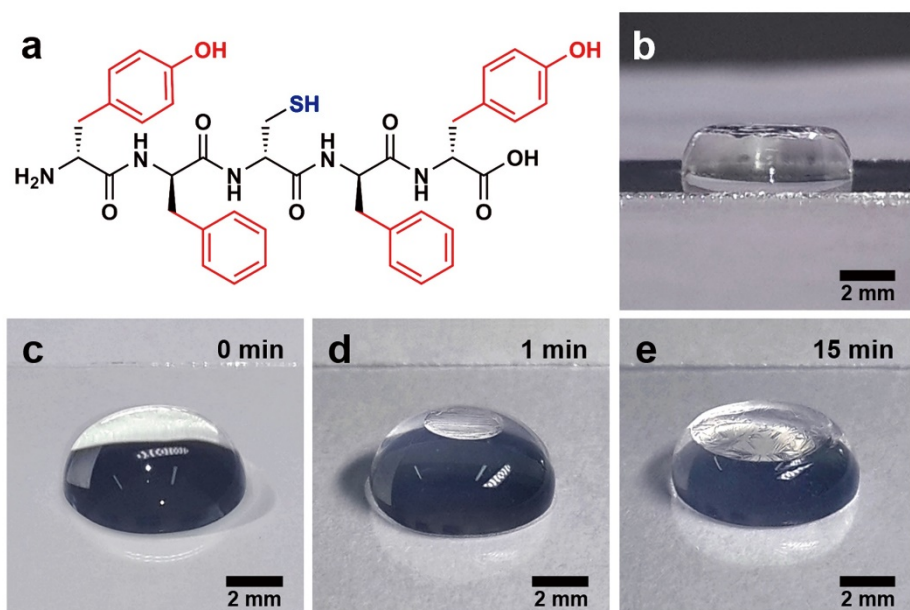


Figure 2.2 Facet formation of water droplets by 2D peptide sheets. (a) Chemical structure of YFCFY. (b) Side view of a faceted water droplet on a siliconized glass. (c-e) Optical images of a water droplet containing YFCFY peptides with the passage of time

Buffer (pH 7)	Concentration			
	50 mM	100 mM	300 mM	500 mM
HEPES	Faceting	Faceting	Faceting	No faceting
Sodium phosphates	Faceting	Faceting	Faceting	No faceting
Sodium citrates	Faceting	Faceting	No faceting	No faceting

Table 2.1 Facet formation of YFCFY dimer depending on buffer conditions. Monomer YFCFY was fully oxidized into dimer form in pure water, then the solution was dried up by lyophilization to get pure dimer peptide. Dimer peptides was dissolved in each buffer solution and concentration was 0.5 mM. As shown in Table, faceting phenomenon does not occur when the buffer concentration is too high. It means that the ions in the buffer partially screen charges of the peptide, resulting inhibition of the self-assembly into large sheets. However, YFCFY can assemble into rigid sheets in several kinds of buffers over a wide range of buffer concentration.

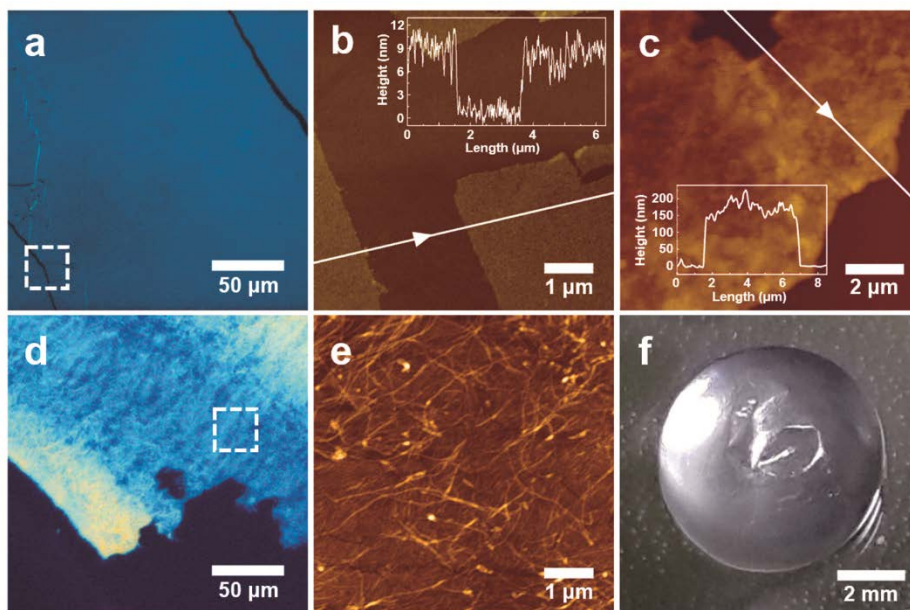


Figure 2.3 Morphology of dimer sheets and monomer films. (a) Optical microscopy image of dimer sheets (b) Atomic force microscopy (AFM) image highlighted with a white box in (a). (c) AFM image of dimer sheets prepared by an extraction method. (d) Optical microscopy image of monomer films transferred by a stamping method. (e) AFM image highlighted with a white box in (d). (f) Top view of the droplet containing monomer films at the air/water interface.

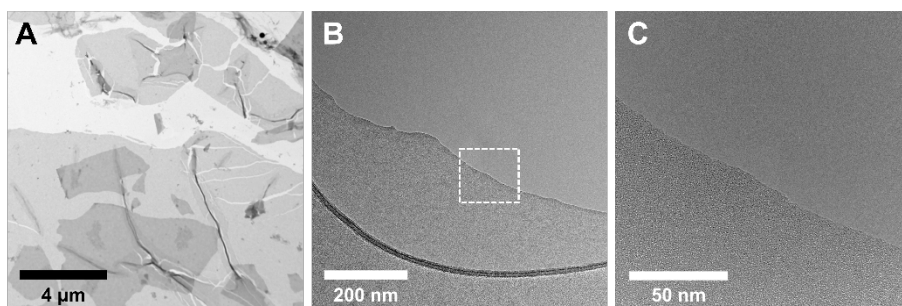
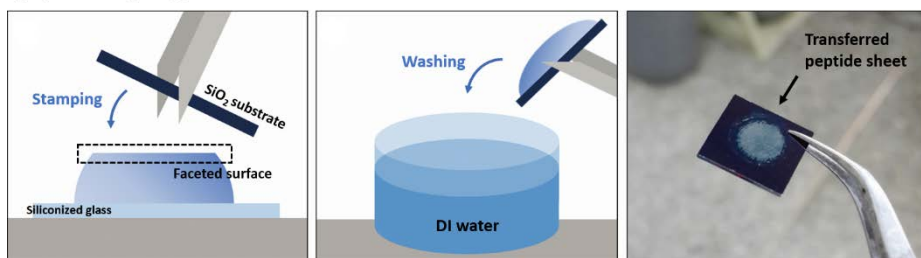


Figure 2.4 Imaging of YFCFY dimer sheets assembled at the air/water interface. (A) TEM image of the sheets (B, C) HR-TEM images of the sheet on a holey carbon grid (D, E) SEM images of the sheets on a silicon oxide substrate.

(a) Stamping method



(b) Extraction method

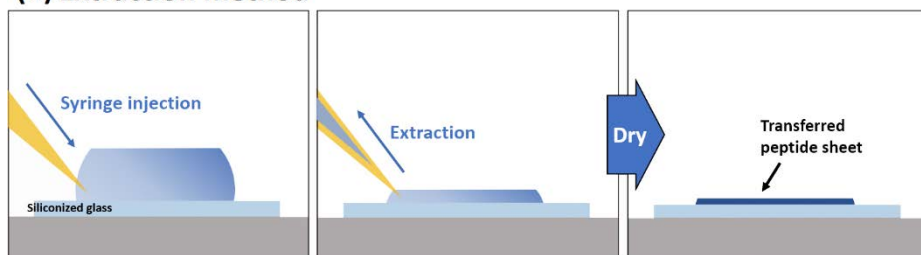


Figure 2.5 (a) Stamping method. Faceted surface was transferred to a silicone oxide substrate by stamping. After that, remaining fibril and fragment were removed by washing the sample with deionized water and dried. (b) Extraction method. A syringe was inserted carefully into faceted droplet. The inner solution of the droplet was extracted slowly as maintaining sheet on the top and dried.

2.3.2 Facet formation kinetics

The assembly kinetics and its dependence on the dimer concentration of the initial solutions were investigated using high performance liquid chromatography (HPLC) (Figure 2.6) and electrospray ionization mass spectrometry (ESI-MS) (Figure 2.7). We carried in-situ chromatography experiments by aging time. As a result, spectra showed monomer peptide gradually converted into oxidized products. In ESI-mass spectroscopy data of the product, there was new significant peak came up at the value of twice of molecular weight of YFCFY monomer. From chromatography results and this mass data, we could confirm oxidized product was YFCFY dimer. As shown in Figure 2.8, the conversion process from monomer to dimer occurred gradually with a rate of approximately 21% per day and the facet formation was accelerated by increasing the proportion of dimer. The facet formation time of samples containing more than 80% of dimer was less than 5 min, while no faceting was observed for samples containing less than 12% of dimer in solutions. These results suggest that the dimer plays an important role in the formation of rigid peptide sheets and the self-assembly kinetics.

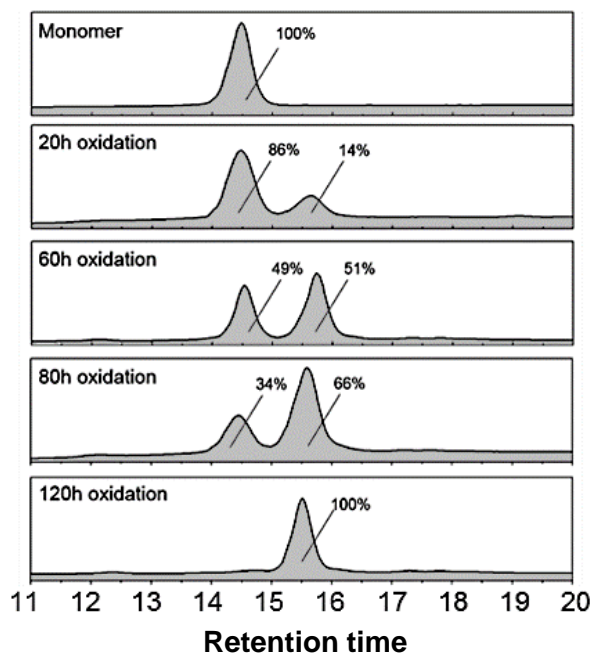


Figure 2.6 High Performance Liquid Chromatography (HPLC) results by the oxidation time for monomer YFCFY

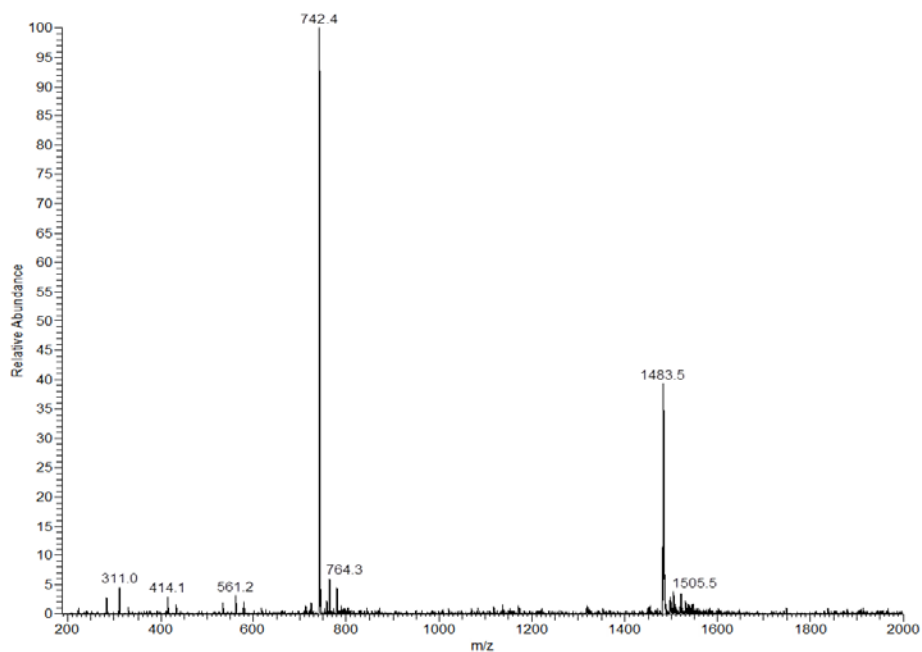


Figure 2.7 Electrospray Ionization Mass Spectrometry (ESI-Mass) data of the second peak (15.5 min) in HPLC. In ESI mass result, the m/z peak at 1483.4 is of dimer YFCFY, the peak at 742.4 is of the monomer YFCFY. Monomer m/z peak was originated from molecules whose disulfide bonding was broken during ionization step in the mass analysis

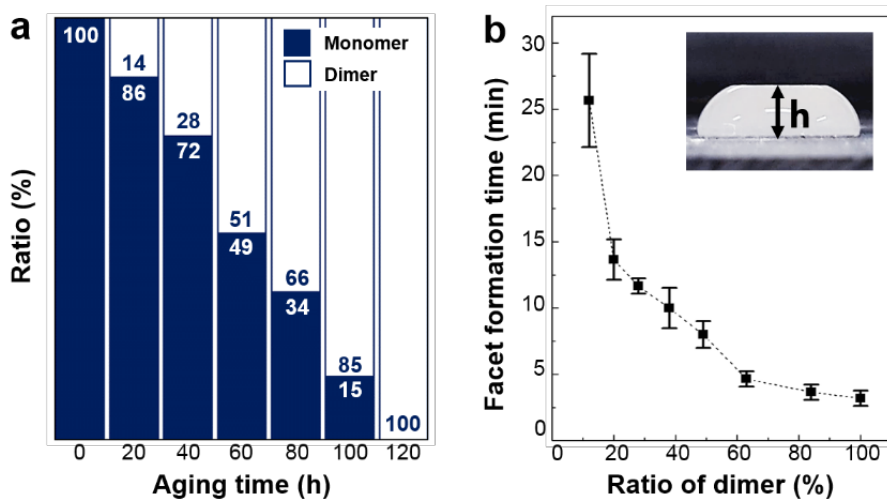


Figure 2.8 Effect of YFCFY dimer on facet formation kinetics. (a) Conversion ratio of monomer to dimer as a function of aging time. (b) Reaction time for facet formation. The time for facet formation of 80 μL droplet was recorded when the distance (=h) between a substrate and the sheet reached 5 mm.

2.3.3 Building block of 2D self-assembly

Raman analysis verified that the dimer is indeed a building block for the peptide sheets. The peptide sheet sample was prepared from a solution that was incubated for 2 days and contained more than 50% monomer (Figure 2.8a). However, as shown in Figure 1.8a, no signal corresponding to the sulfhydryl residues (-SH) at 2570 cm^{-1} was observed in the Raman spectra of the sheets. The sample exhibits a strong signal at 504 cm^{-1} corresponding to a disulfide stretching vibration band, which confirming that dimerization was due to disulfide bond formation between the cysteines.^{41,42} In the Raman data of the monomers, a signal corresponding to -SH stretching vibration from the cysteines was observed at 2570 cm^{-1} . These results indicate that only the dimer exists in the peptide sheets.

The Raman spectra also exhibits the additional information about interactions between tyrosine residues. The peak intensity ratio of 850 cm^{-1} to 830 cm^{-1} of monomer is about 0.8, but it increases into 1.05 in assembled peptide sheets. (Figure 2.9b) Those two outstanding peaks called Fermi resonance doublet are commonly discovered in Raman spectra of molecules containing para-substituted benzenes. The peaks at 830 cm^{-1} and 850 cm^{-1} represent the normal mode ν_1 (in-plane breathing fundamental) and the second harmonic $2\nu_{16a}$ (overtone of an out-of-plane ring bending) respectively⁴³⁻⁴⁵.

Their intensity ratio (I_{850}/I_{830}) has been used as a parameter having information about states of benzene and hydroxyl group in the tyrosine residue. The increased intensity ratio indicates that a substantial portion of the phenolic hydroxyls is strongly hydrogen bonded in the assembled structure⁴⁶. It is known that hydrogen bonding and van der Waals interactions of polar groups including phenols in tightly packed interior of folded protein are more preferred than similar interactions with water in the unfolded state. Those polar groups buried inside of protein contribute to protein stability extensively. Also, hydration state of a hydroxyl group can be changed depending on preferred geometry of a tyrosine⁴⁷. From that it can be suggested that π - π stacking among aromatic residues enabled condensed molecular packing at the air/water interface to make hydrophobic interiors, which can induce strongly hydrogen bonded hydroxyl groups.

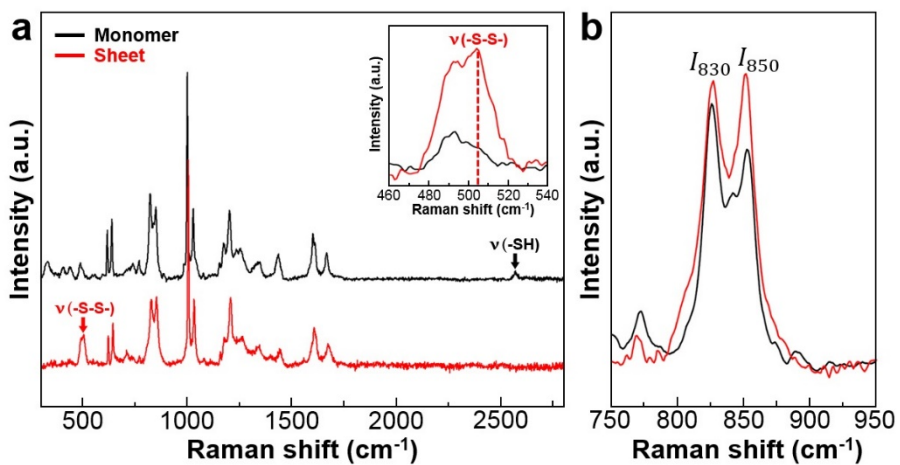


Figure 2.9 Raman analysis of peptide sheets. (a) The Raman spectra of monomers (black line) and peptide sheets (red line). The signal of the range of 460–540cm⁻¹ is magnified as an inset. The peak at 2,570 cm⁻¹ was from sulfhydryl residue of cysteine (-SH) and 504 cm⁻¹ indicated disulfide bonding (-S-S-). (b) The Raman signal from 750 cm⁻¹ to 950 cm⁻¹ range.

2.3.4 Molecular conformation of YFCFY peptide

To investigate the molecular conformations of the 2D assembled structures and solvated peptides, solid circular dichroism (CD) and solution-phase CD analysis were performed. As shown in Figure 2.10a, the solution of monomer and dimer both exhibits two positive peaks at 202 nm and 224 nm. These CD spectra are not similar to typical CD spectra of the conformations such as α -helix, β -sheet, and random coil. The two positive peaks can arise due to contributions from aromatic chromophores, such as phenols and benzenes, which cause interference with the signal from the amides depending on the local environment.⁴⁸ The CD measurements of poly-L-tyrosine (PLT) in a helical conformation revealed that there is the positive Cotton effect from the tyrosine side chain at 225 nm.⁴⁹ In addition, strong positive band contribution from tyrosine side chains at approximately 225 nm has been observed in several proteins.⁵⁰⁻⁵³ The positive peak located at approximately 200 nm originated from the amide π - π^* transition and L_a , L_b transition of tyrosine and phenylalanine.⁵¹ Therefore, the positive peaks located at 202 nm and 224 nm in our systems may arise from tyrosine, phenylalanine, and the amide transition. These strong positive peaks near 202 nm and 225 nm from tyrosine and phenylalanine are overlapped with the negative broad peaks centered on 207 nm and 222 nm from n - π^* transition of the α -helical peptide bonds. As a result,

a relatively weak negative peak near 215 nm, instead of showing two minima at 207 and 222 nm, is considered as one of the characteristics of PLT and tyrosine-rich peptide (TRP) with a right-handed alpha-helical conformation. YFCFY dimer and monomer solution both exhibits strong positive peak around 202 and 225 nm, and only dimer solution shows negative peak at 212 nm which is similar to the reported right-handed α -helical TRP and PLT. With the assumption that the contribution of the peptide chromophores and the aromatic contribution are additive, the spectrum characteristic of a non-aromatic right-handed α -helix is obtained clearly by subtracting the spectra of dimer solution from that of monomer solution. (Figure 2.10a) The resulting spectrum (dashed) shows double minima at 204 and 221 nm. Within this context, the solution CD spectra can support the presence of right-handed α -helical conformation although the CD spectra are different from the typical characteristics of α -helix.

Conformations of the assembled structures were clearly interpreted using solid CD analysis because the positive Cotton effects of the aromatic side chains were relatively minimized. The CD spectra of the dimer sheets shown in Figure 1.10b contains a strong positive peak at 193 nm and minima at 222 nm ($n-\pi^*$ transition) and 207 nm ($\pi-\pi^*$ transition). These results indicate that the dimer sheets have a typical right-handed helical conformation. The relatively weak intensity of the $n-\pi^*$ transition compared to that of the $\pi-\pi^*$ transition may indicate the presence of a 3_{10} -helix conformation. In detail, the ratio of the CD

intensity of the $n\text{-}\pi^*$ transition to that of the $\pi\text{-}\pi^*$ transition ($[\theta]_{222}/[\theta]_{207}$) for the 3_{10} -helix is in the range of 0.15-0.40,⁵⁴⁻⁵⁶ and the value for the α -helix is close to 1.⁵⁷ Because the value for the dimer sheets is 0.68, the two conformations may exist as equilibrium mixtures. The solid CD spectra of the monomer films contain a strong positive peak at 192 nm and two minima (202 nm and 225 nm), which are substantially shifted from those typical of common helical conformations. This result implies that the monomer films have a distorted helical conformation. Additionally, a weak positive peak at 240 nm, which appear in the spectra for the dimer sheets, can be assigned to a disulfide bond transition.^{58,59} According to a previous study, this peak can be detected in far-UV region when dihedral angle of the disulfide bond deviates from 90° .⁶⁰ Therefore, the dihedral angle of the disulfide bond was reorganized during the assembly process.

The structural differences between the monomer and dimer were confirmed by 2D NMR spectroscopic analysis. The YFCFY peptide gradually changes from the monomers to the dimers due to the formation of disulfide bonds between the cysteine residues. The oxidation reaction was monitored by NMR after 0, 24, 48 hours of reaction. Using 2D total correlation spectroscopy (TOCSY) and 2D nuclear Overhauser effect spectroscopy (NOESY), each amide and alpha proton of YFCFY peptide was assigned.^{60,61} The gamma protons of the cysteine were observed at ~ 2 ppm (Figure 2.11 a,b). As a result of the oxidation reaction, new resonances for Cys3, Phe4, and Tyr5 appeared

in both the 2D NOESY and 2D TOCSY spectra (Figure 2.11b and 2.12b), indicating that the YFCFY dimer formed. After 48 hours, complete oxidation of YFCFY was confirmed due to the elimination of the gamma proton peak of Cys3 in the 2D TOCSY spectrum (Figure 2.11c), and only the oxidized form of the peptide exists (Figures 2.11c and 2.12c).

The YFCFY monomer shows sequential NOE connectivities between the neighboring amide and alpha protons and weak NOEs between the neighboring amide and amide protons in the NOESY spectrum (Figure 2.12a, top and bottom), which are observed for a random coil polypeptide. Because YFCFY is rather short and some of the peaks in the 2D NOESY spectra overlap, the non-sequential NOEs are not clearly shown. For example, the resonance for the amide protons of Cys3 and Tyr5 and the alpha protons of Phe2 and Phe4 are too close in the spectrum (Figure 2.12c, top and bottom). Due to these ambiguous NOE constraints, structure calculation was challenging. Therefore, the helicity of the dimer was confirmed by observing the strong sequential NOEs between neighboring amide protons and additional non-sequential NOEs such as those associated with Phe2-Phe4 and Phe2-Tyr5 (Figure 2.12c). These connectivities represent typical conformations of helix.^{62,63} In accordance with our CD data, this result indicates that the YFCFY dimer forms a helical secondary structure.

Additionally, in order to gain a structural insight of the building unit of YFCFY dimer sheet, semi-empirical model structure of YFCYF dimer was

built (Figure 2.13). A structure calculation of the dimer was carried out using the protocol of CYANA 3.0 program in LINUX.⁶⁴ A total of 100 structures were calculated from a set of 33 sequential and 8 non-sequential NOEs and 8 α -helical ϕ and ψ dihedral angles. The 20 lowest energy structures have a backbone r.m.s.d. error of 0.32 Å. Figure 2.13 shows the calculated lowest energy structure of YFCFY dimer, where two monomers are connected through disulfide bond. In accordance with NMR results, each monomer has almost identical structure exhibiting a helical conformation. The distance of 6.4 Å between C α (Tyr1) and C α (Tyr5) is slightly longer than the vertical distance of 5.5 Å between one consecutive turn of α -helix. It is probably caused by short length of the peptide, which cannot be tightly fixed due to lack of intramolecular hydrogen bonding. Interestingly, the dimer shows strained disulfide conformation with a dihedral angle of 165°, which is consistent with solid CD data of dimer sheets.⁵⁹ It is also noteworthy that all phenol and benzene groups in each monomer faced toward solvent. All side chains of tyrosines and phenylalanines are arranged along both vertical and lateral directions. The vertical and lateral length of the building block are 13.2 Å (distance between Phe2 and Tyr5) and 25.6 Å (distance between Tyr1 and Tyr1') respectively. With the assumption that the building block stacks in lateral direction, the transferred dimer sheets with thickness of 10 nm have 4 times stacked layers of YFCFY dimers. Such arrangement of hydrophobic side chains

may contribute to assembly of macroscale 2D structures comprising stacked nanosheets.

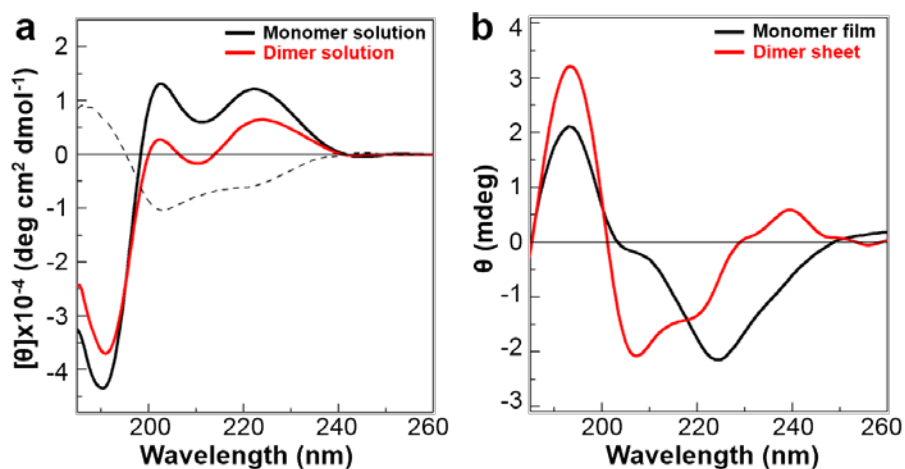


Figure 2.10 Circular dichroism (CD) analysis of YFCFY peptide. (a) The CD spectra of 300 μ M YFCFY monomer and 150 μ M YFCFY dimer in water. The solid CD spectra are expressed in degree of ellipticity (θ) without concentration terms and the solution CD spectrum are expressed in converted molar ellipticity ($[\theta]$). (b) The CD spectra of monomer film and dimer sheet directly transferred to a quartz cuvette by the stamping method.

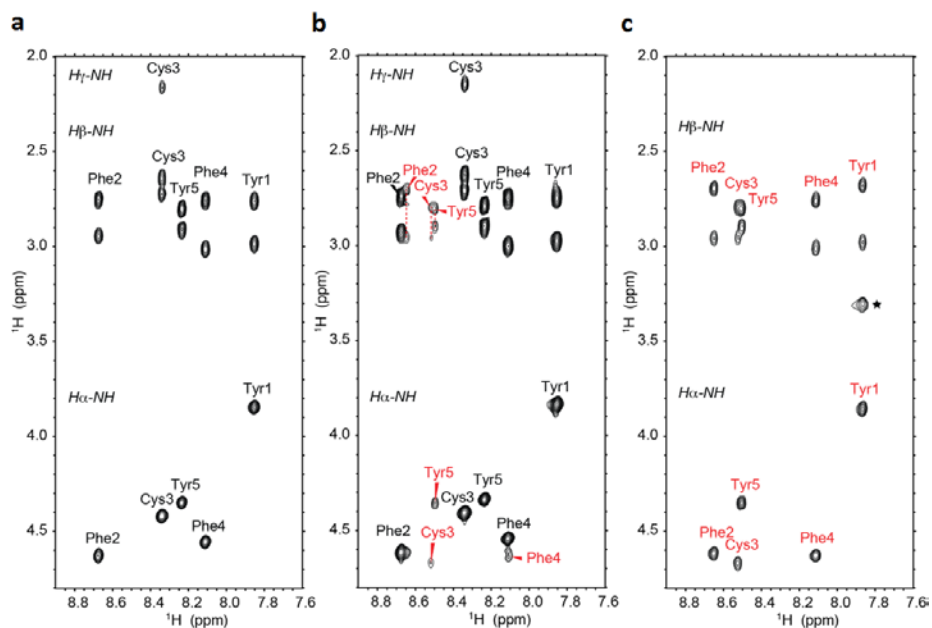


Figure 2.11 2D TOCSY NMR spectra of YFCFY peptide after (a) 0 h, (b) 24h and (c) 48 h of oxidation in DMSO. Spectra show the correlation between alpha, beta, and gamma protons and amide protons. With increasing reaction time, formation of dimeric YFCFY generates new resonances for Cys3, Phe4, and Tyr5 (b, red). No resonance for Cys3 gamma proton clearly proves the formation of a disulfide bond between Cys residues (c). Star is only shown in the dimeric form of YFCFY that is originated from the TOCSY correlation between the amide proton of Tyr1 and its aromatic proton in the phenol ring.

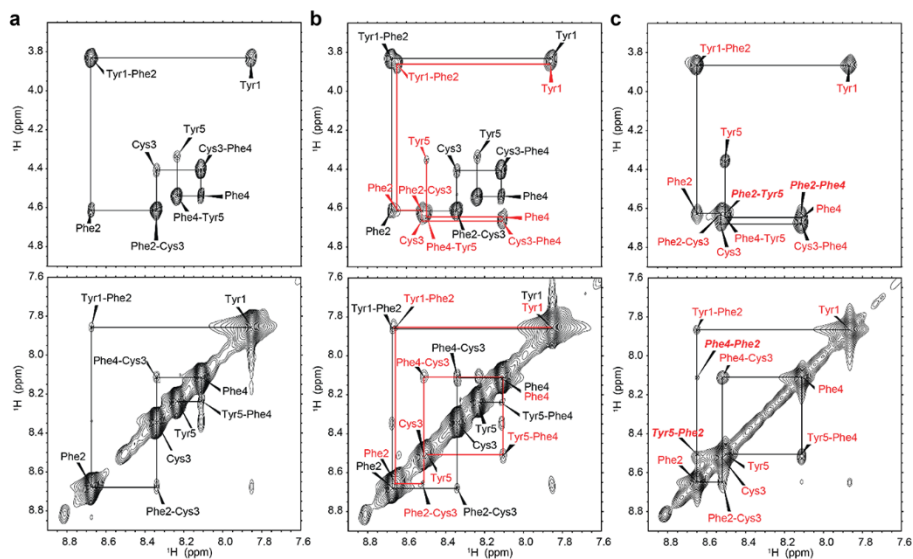


Figure 2.12 2D-NMR analysis of YFCFY peptide. (a-c) NOEs between amide and alpha protons (top) and between amide protons (bottom). Resonances of YFCFY are assigned after (a) 0 h, (b) 24h and (c) 48 h of oxidation in DMSO. With increasing reaction time, largely shifted resonances for Cys3, Phe4, and Tyr5 appear (b), and non-sequential NOE connectivities (c, bold italic) also appear after completion of oxidation, indicating YFCFY dimer formation. Amino acids from dimer are colored in red.

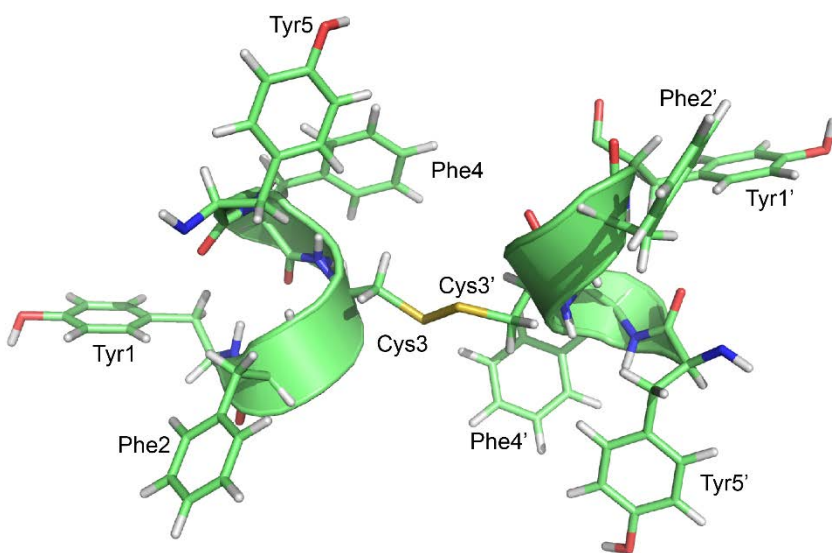


Figure 2.13 NMR solution structure of YFCFY dimer peptide. The model structure consists of two symmetric helical YFCFY monomers connected by a disulfide bond between the cysteine residues. The carbon, oxygen, nitrogen, sulfur and protons are colored in green, red, blue, yellow and white, respectively.

2.3.5 Hybrid 2D self-assembly of YYCYY peptide using gold ion

As an effort to control the backbone chirality and folding for 2D assembly, we explored the possibility to use α -helical sequences and disulfide-bridged dimer structures. It was intended that disulfide bonding stabilizes the local conformation of the monomer helix and thus facilitates the specific interaction for the two-dimensional growth at the air/water interface. Specifically, we identified three peptide sequences—YYCYY, YYACAYY, and YFCFY (Y: tyrosine, C: cysteine, F: phenylalanine)—that spontaneously assemble into film at the air/water interface and surprisingly flatten the top of the water droplet. It was found that the dimer formation by cysteine in each monomer is a key step for effective assembly. As the next step, we demonstrated a new redox-mediated hybrid 2D assembly system using gold ion as an oxidant to induce a disulfide bridge between cysteines.

Herein, we chose a short 5 amino acid peptide (YYCYY) of which the dimer formed by disulfide bonds can assemble into macroscopic nanosheets at the air/water interface of a water droplet (Figure 2.14). The disulfide bond stabilizes the helical conformation of the dimer peptide, leading to strong molecular interactions and enhanced mechanical properties of the assembled structures.⁴⁰ In previous works, the disulfide bond was induced by mild oxidation processes such as simple aeration or incubation in dimethyl sulfoxide

for facet formation. In an effort to expand the 2D assembly system and further hybridize with gold nanoparticles, we introduced redox-mediated 2D assembly using Au^{3+} , which can induce disulfide bonds and be reduced by tyrosine and cysteine.

The clear faceted surface of the water droplet containing YYCYY and HAuCl_4 can be observed with the naked eye (Figure 2.14). In the sample preparation procedures, the YYCYY monomer was dissolved in deionized water, and the solution was incubated at 80°C for 20 min. Then, the solution was directly mixed with a HAuCl_4 solution and a droplet of the mixture was placed on siliconized glass. In a few minutes, a thin transparent film was formed on the surface of the droplet and the top of the droplet was continuously flattened by a rigid peptide sheet. To examine the assembled structures, samples were prepared by directly stamping the droplet with a SiO_2 substrate and washing with deionized water immediately. An optical microscopy image showed an extensively homogeneous 2D structure decorated with aggregated gold particles. (Figure 2.14d) Atomic force microscopy (AFM) analysis clearly revealed that the thickness of the peptide nanosheet was 30 nm, which is 3 times thicker than the previously reported thickness of YFCFY peptide sheets obtained from a faceted droplet.²⁰ (Figure 2.14e) Interestingly, the sheet templated the growth of gold nanoparticles. As shown in Figure 2.14f,g and Figure 2.15, scanning electron microscopy (SEM) images and the EDS mapping images show that a large number of spherical gold nanoparticles, with

sizes ranging from 80 to 230 nm, formed on the peptide nanosheet and no particles on the surface of the substrate, indicating that the gold nanoparticles were selectively reduced and adsorbed on the peptide sheet. The combined results demonstrate that the peptide assembled into the nanosheet at the air/water interface and Au³⁺ were reduced to gold nanoparticles on the peptide sheet in the absence of other reducing agents simultaneously.

In order to further examine the effect of the gold ion concentration on the capability of large 2D peptide assembly, the facet formation time was measured and the droplet was stamped with a SiO₂ substrate to observe the assembled structures. As shown in Figure 2.16a, we could observe faceting phenomena only within a specific concentration range for gold ions (1.5–10 mM). However, there was no tendency of the facet formation time depending on the gold ion concentration. When the concentration of HAuCl₄ was lower than 1 mM, faceting did not occur but only a small amount of fibrillar aggregation was observed on the substrate (Figure 2.17). The results suggest that a gold ion concentration below 1 mM is insufficient to produce the minimum quantity of dimer peptide to assemble into rigid 2D sheets since it has been reported that a critical dimer concentration is required for facet formation. In the case of the gold ion concentration being higher than 10 mM, no faceting was observed. Instead, a rough fibril-aggregated film was formed at the air/water interface at a certain concentration range (20–40 mM). The film exhibited a non-uniform, wrinkled morphology and a fibrillar structure

appeared in the broken part of the film (Figure 2.16b). AFM results showed that the film was composed of bundled fibrillar fragments and there were no gold particles in the large area of the film (Figure 2.16c). It can be inferred that the film had peeled off and detached during the transfer and washing procedures owing to the relatively weak interactions between fibrils. Based on observations, we can conclude that there is an optimum Au^{3+} concentration range for facet formation and too high a concentration of Au^{3+} leads to other assembly pathways producing bundled fibrillar structures.

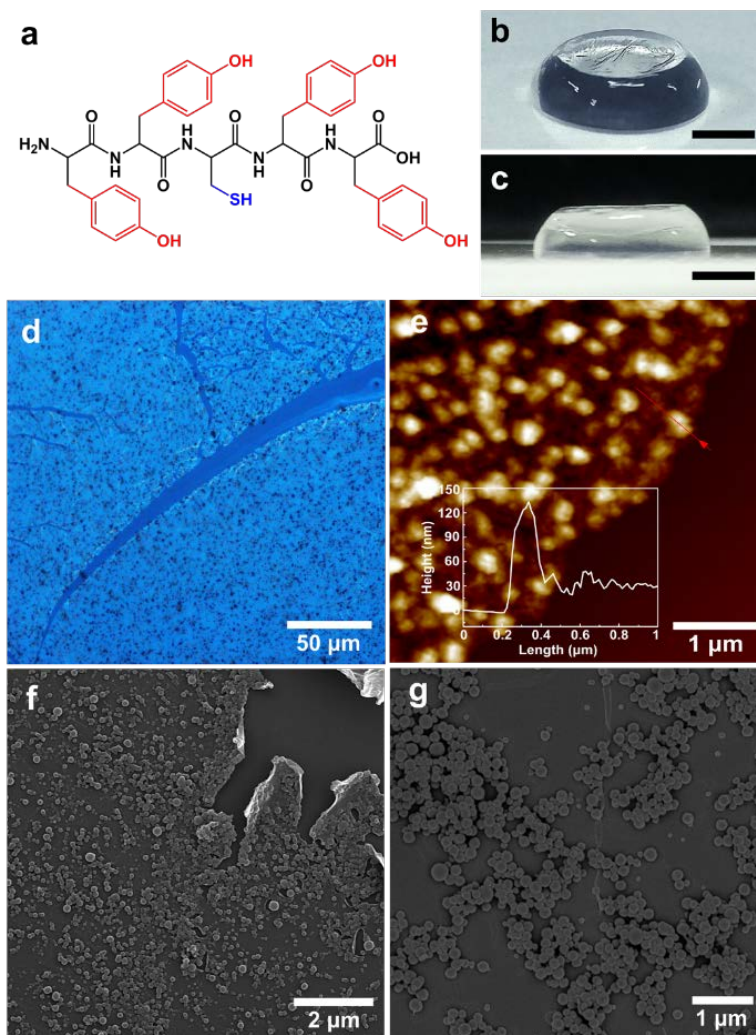


Figure 2.14 Facet formation of water droplets by 2D peptide sheets and morphology of the sheets (a) Chemical structure of YYCYY. (b,c) Optical images of a faceted water droplet on a siliconized glass. Scale bar, 2 mm. (d) Optical microscopy image of the sheets. (e) AFM image of the peptide sheet and gold nanoparticles (f,g) SEM images of the peptide sheets and gold nanoparticles.

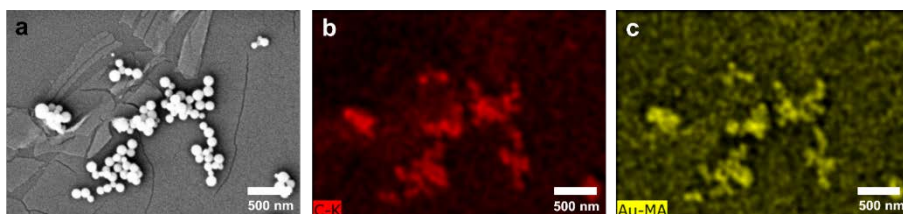


Figure 2.15 SEM/EDS mapping images of gold nanoparticles and peptide hybrid film. (a) SEM image of the peptide sheets and gold nanoparticles. (b, c) EDS mapping images show the elemental distributions of carbon (b) and gold (c).

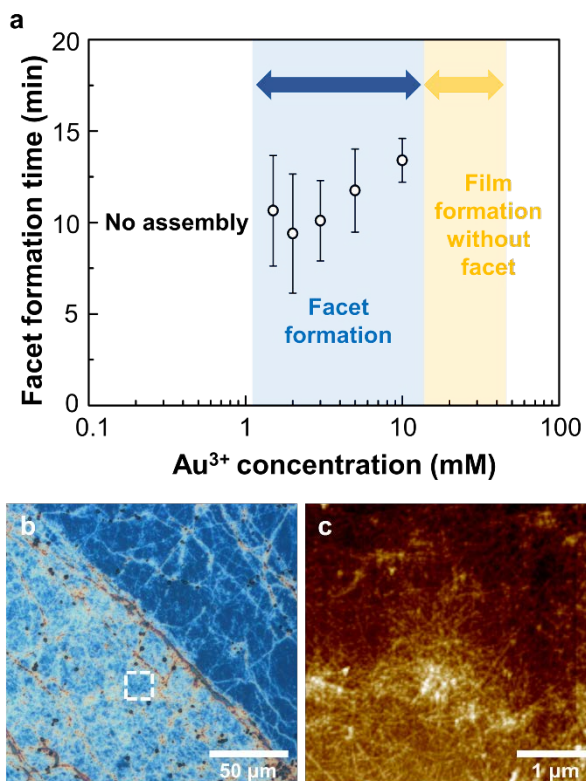


Figure 2.16 Effect of gold ion concentration of facet formation (a) Reaction time for facet formation depending on Au^{3+} concentration. Blue region, facet formation. Yellow region, film formation without facet. (b) Optical microscopy image of a transferred film formed under high concentration of Au^{3+} (20–40 mM). The right upper side of the image is the broken part of the film. (c) AFM image highlighted with a white box in (b).

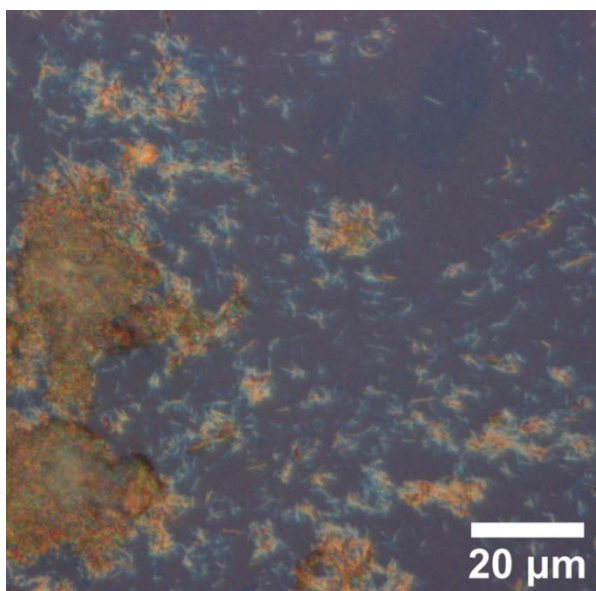


Figure 2.17 Optical image of fibrillar aggregations. The sample was prepared by directly stamping from the water droplet when the concentration of gold was lower than 1 mM.

2.3.6 Chemical structure of YYCYY after reaction with gold ion

Previously, it was reported that Au^{3+} can induce the oxidation of cysteine to cystine having a disulfide bond.⁶⁵⁻⁶⁷ During the reaction, Au^{3+} reduced to Au^{1+} , which formed a polymeric structure where Au^{1+} ions are bridged by the thiolate sulfur of cysteine. Addition of a reductant such as sodium borohydride decomposes the polymeric structure to produce gold nanoparticles. In our YYCYY peptide system, redox-active tyrosine plays a vital role not only in 2D assembly but the growth of gold nanoparticles. It can be derived that at first Au^{3+} rapidly oxidizes cysteine to form the dimer peptide while it is reduced to Au^{1+} . Simultaneously, the dimer peptide assembles into 2D nanosheets at the air/water interface and oxidative phenolic groups in tyrosine produce gold nanoparticles adsorbed onto the peptide sheets. Liquid chromatography/mass spectroscopy (LC/MS) results clearly showed that dimerization of YYCYY and oxidation of tyrosine occurred during the reaction. Figure 2.18 shows LC/MS results obtained from the reaction of YYCYY peptide with HAuCl_4 . In particular, there are four peaks in LC spectra when the added amount of HAuCl_4 was 2 mM where the concentration of facet formation occurs. The highest peak at retention time of 2.48 min corresponds to the unreacted monomer YYCYY, $[\text{M}-\text{H}]^-$, species (m/z 772.7). There was new significant peak came up at retention time of 8.73 min and the m/z 1544.8 of

this peak can be assigned to the mass of the dimer YYCYY. Other m/z values of reaction products were matched with the suggested oxidized forms of tyrosine in Figure 2.18a. In nature, tyrosine is involved in many protein oxidation processes, being one of the most easily oxidized amino acids. It is reported that tyrosine oxidation can occur through several routes, where the dominant pathway brings to the formation of 3,4-dihydroxyphenylalanine.⁶⁸ Besides tyrosine radical can undergo a number of oxidative post-translational modification to form hydroxyl-tyrosine, nitro-tyrosine, crosslinked-tyrosine, and halogenated tyrosine. Such oxidation of tyrosine and nature of the oxidation products depend on the pH, nature of oxidizing agent and the condition of the reaction mixtures. The results clearly showed that tyrosine had a role to reduce gold cation for the formation of gold nanoparticles and tyrosine was oxidized into several forms. Notably, tyrosine in its solubilized form has a reducing ability only in basic conditions or at high temperatures.⁶⁹⁻⁷¹ Thus, we can assume that cysteine and tyrosine in a well-organized peptide nanostructure can cooperatively trigger or enhance redox reactions in a manner similar to that observed in a biological enzyme system.

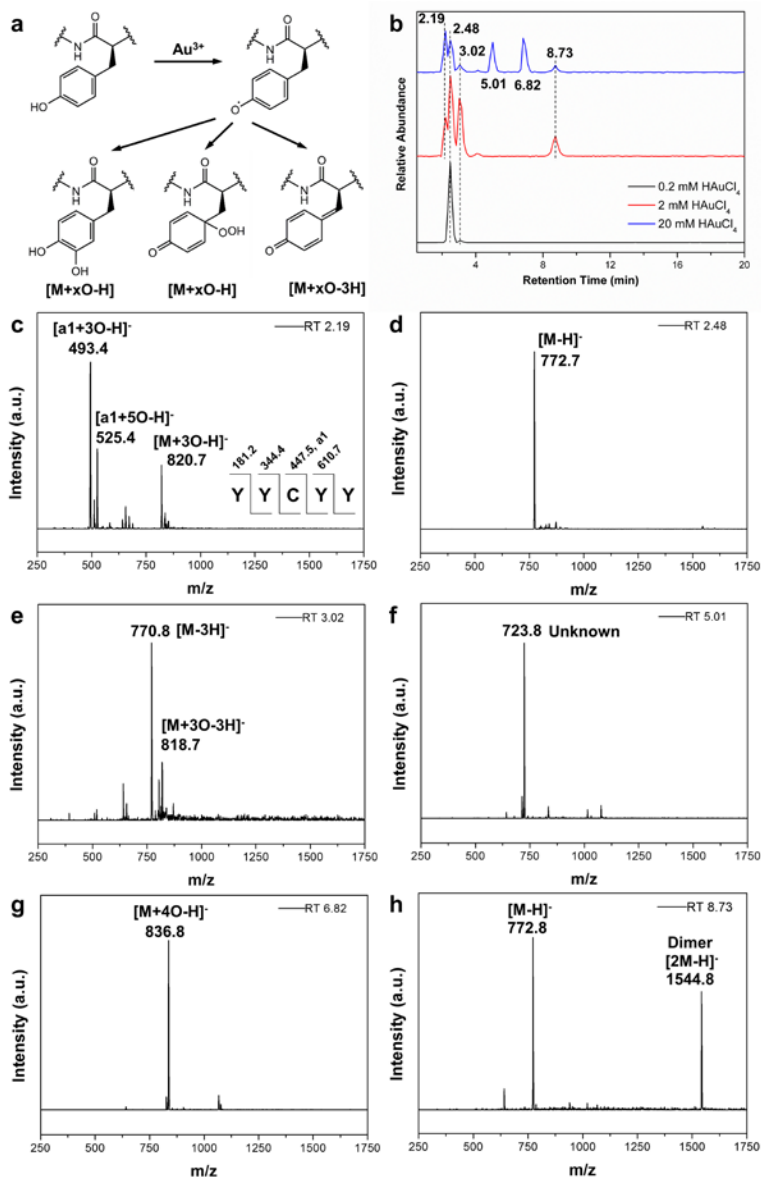


Figure 2.18 Presence of oxidized tyrosines and dimer analyzed by LC/MS. (a) Proposed oxidation pathways of tyrosine in this system. x denotes the number of added oxygen. (b) LC results of reaction products of YYCYY (1.5 mM) and HAuCl_4 (0.2, 2, 20 mM). (c-h) ESI-MS data of each peak in the spectrum.

2.3.7 Molecular conformation of YYCYY peptide

To investigate the difference between the molecular conformations of the peptide before and after reaction with HAuCl_4 , circular dichroism (CD) analysis was performed. As shown in Figure 2.19, the peptide solution exhibited two positive peaks at 203 nm and 226 nm. After mixing with the HAuCl_4 solution, the spectrum showed a relatively weak negative peak near 218 nm and decreased intensity of the positive peaks (203 nm and 226 nm). This result corresponds with a previously reported CD spectrum of facet-forming peptides with an α -helical conformation.⁴⁰ The aqueous solution of the monomer peptides presented two positive peaks near 203 nm and 226 nm and that of the dimer peptides exhibited a negative peak at 218 nm with two positive peaks with decreased intensity. These CD spectra were not similar to the typical CD spectra of conformations such as α -helix, β -sheet, and random coil. The two positive peaks at 203 nm and 226 nm can arise due to contributions from aromatic chromophores such as phenols, which cause interference with the signal from the amides depending on the local environment.⁴⁸ The CD measurements of poly-L-tyrosine in a helical conformation revealed a positive Cotton effect owing to the tyrosine side chain at 225 nm.⁵⁰ The positive peak located at approximately 202 nm originated from the amide π - π^* transition and L_a , L_b transition of tyrosine.⁵¹ Therefore, the positive peaks located at 203 nm

and 226 nm arose from tyrosine and the amide transition. These two strong positive peaks from tyrosine overlapped with the negative broad peaks centered at 207 nm and 222 nm arising from the $n-\pi^*$ transition of the α -helical peptide bonds. As a result, a relatively weak negative peak near 218 nm, instead of two minima at 207 and 222 nm, was considered as one of the characteristics of poly-L-tyrosine with a right-handed α -helical conformation.⁵⁰ Likewise, it can be expected that a YYCYY dimer was formed after reaction with HAuCl_4 , and the CD spectra exhibiting the negative peak at 218 nm indicated that the YYCYY dimer had an α -helical conformation.

The conformational change in solid state after self-assembly was also investigated using Fourier transform infrared spectroscopy (FT-IR). As shows in Figure 2.20, FT-IR spectra of monomer YYCYY displayed prominent absorbance bands at 1603, 1620, 1637, 1667 cm^{-1} in the amide I region. In particular, the spectra of monomer YYCYY and the peptide sheets had bands at 1603 and 1620 cm^{-1} in common, which were originated from C-H bending vibration and C-C in-plane ring stretching vibration of tyrosine.⁷² The bands at 1637 and 1667 cm^{-1} in spectra of monomer were indicative of β -sheet and β -turn respectively. Considering that 5-mer peptide could not possess two conformations due to short length of backbone, both conformational structures would coexist. Interestingly, in the case of self-assembled sheets, the FT-IR spectra displayed the typical characteristics absorption of α -helix at 1655 cm^{-1} .⁷³ This results reflected that the conformation of YYCYY had changed into

helical structure during the reaction with HAuCl_4 and assembly process.

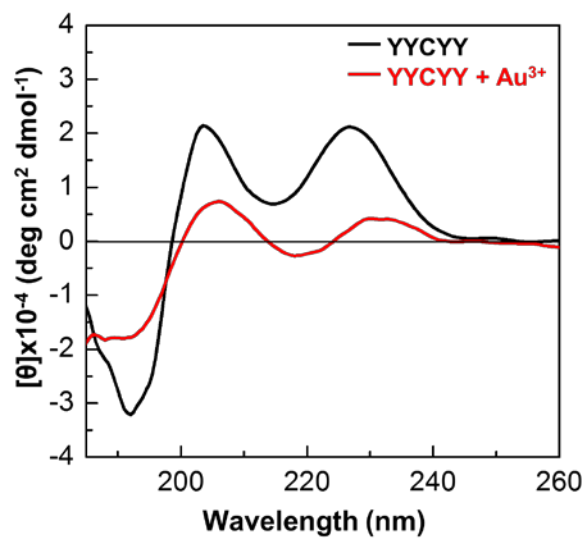


Figure 2.19 CD analysis of YYCYY peptides. CD spectra of 300 μM YYCYY monomer and 300 μM YYCYY with 400 μM Au^{3+} in water.

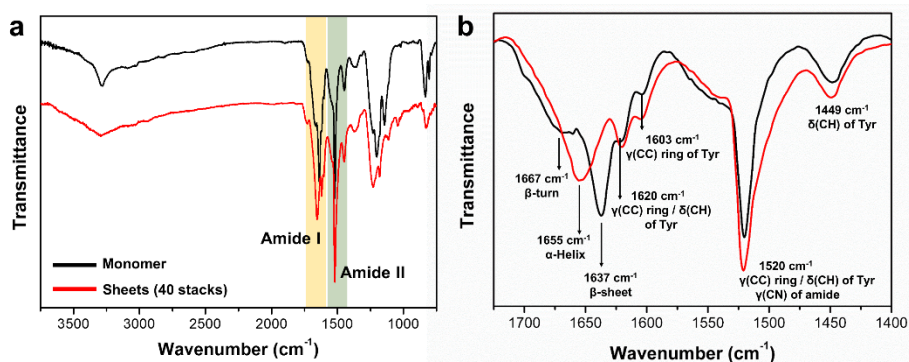


Figure 2.20 FT-IR spectra of monomer peptide (black line) and film (red line). (a) Representative FT-IR spectrum of monomer YYCYY and stacked nanosheets in region of 3750 to 750 cm⁻¹. Vibrational bands of the amide I and amide II regions are indicated with vertical bars. (b) FT-IR spectra in amide I and II regions, highlighted in (a). γ and δ denote stretching vibration and in-plane bending vibration respectively.

2.4 Conclusion

Until now, β -sheet motifs were widely chosen to build 2D nanostructures.^{35,74-78} However, macroscopic flatness of assembled structure with β -sheet arrangement is constrained by propeller-like twist in the shape of each β -strand, which is originated from structural factors such as chirality.³⁵ Interestingly, in peptide mimetic peptoid polymers, it was discovered that newly identified Σ -strands folding enable the atomically flat 2D assembly. In this context, our study can provide a valuable experimental evidence that emphasize the importance of stabilization of helix for the further 2D and 3D assembly. Recently, it was also found that single heptad peptides can assemble into super-helical nanostructures by stabilizing helical conformation.⁷⁹

This study provides the demonstration of the 2D self-assembly behaviors of a pentapeptide on the surface of a water droplet. Interestingly, the dimerization process changes the morphology of the assembled structures from fibrils to giant sheets and also accelerates the facet formation kinetics at the air/water interface. The disulfide bond between the monomers stabilizes the helical conformation, resulting in strong molecular interactions and reinforced mechanical strength of the assembled structure. Our results provide insight into the effect of short peptide folding on macroscale self-assembly. In addition, based on the interactions between gold ions and a pentapeptide, we found

redox-mediated 2D peptide assembly and by applying this principle, we created giant nanosheets decorated with gold nanoparticles at the air/water interface. The disulfide bond generated by gold atoms fixed two alpha helix structures and the tyrosine-rich peptide induced further arrangement of the helix, which in turn produced a rigid organic–inorganic hybrid structure. This work opens the avenue of self-assembling helical peptides that can construct transferable and giant 2D architectures with minimal molecular element.

2.5 References

1. Lee, J.-H.; Lee, J. H.; Lee, Y. J.; Nam, K. T. Protein/peptide Based Nanomaterials for Energy Application. *Curr. Opin. Biotechnol.* **2013**, *24*, 599–605.
2. Kim, S.; Kim, J. H.; Lee, J. S.; Park, C. B. Beta-Sheet-Forming, Self-Assembled Peptide Nanomaterials towards Optical, Energy, and Healthcare Applications. *Small* **2015**, *11*, 3623–3640.
3. Crookes-Goodson, W. J.; Slocik, J. M.; Naik, R. R. Bio-Directed Synthesis and Assembly of Nanomaterials. *Chem. Soc. Rev.* **2008**, *37*, 2403–2412.
4. Hauser, C. A. E.; Deng, R.; Mishra, A.; Loo, Y.; Khoe, U.; Zhuang, F.; Cheong, D. W.; Accardo, A.; Sullivan, M. B.; Riekkel, C.; Ying, J. Y.; Hauser, U. A. Natural Tri- to Hexapeptides Self-Assemble in Water to Amyloid β -Type Fiber Aggregates by Unexpected α -Helical Intermediate Structures. *Proc. Natl. Acad. Sci. U.S.A.* **2011**, *108*, 1361–1366.
5. Sarkar, B.; O’Leary, L. E. R.; Hartgerink, J. D. Self-Assembly of Fiber-Forming Collagen Mimetic Peptides Controlled by Triple-Helical Nucleation. *J. Am. Chem. Soc.* **2014**, *136*, 14417–14424.
6. Li, Q.; Jia, Y.; Dai, L.; Yang, Y.; Li, J. Controlled Rod Nanostructured

- Assembly of Diphenylalanine and Their Optical Waveguide Properties. *ACS Nano* **2015**, *9*, 2689–2695.
7. Hamley, I. W.; Dehsorkhi, A.; Castelletto, V.; Seitsonen, J.; Ruokolainen, J.; Iatrou, H. Self-Assembly of a Model Amphiphilic Oligopeptide Incorporating an Arginine Headgroup. *Soft Matter* **2013**, *9*, 4794.
 8. Mason, T. O.; Chirgadze, D. Y.; Levin, A.; Adler-Abramovich, L.; Gazit, E.; Knowles, T. P. J.; Buell, A. K. Expanding the Solvent Chemical Space for Self-Assembly of Dipeptide Nanostructures. *ACS Nano* **2014**, *8*, 1243–1253.
 9. Sun, L.; Fan, Z.; Wang, Y.; Huang, Y.; Schmidt, M.; Zhang, M. Tunable Synthesis of Self-Assembled Cyclic Peptide Nanotubes and Nanoparticles. *Soft Matter* **2015**, *11*, 3822–3832.
 10. Rubin, D. J.; Amini, S.; Zhou, F.; Su, H.; Miserez, A.; Joshi, N.S. Structural, Nanomechanical, and Computational Characterization of D,L-Cyclic Peptide Assemblies. *ACS Nano* **2015**, *9*, 3360–3368.
 11. Hamley, I. W. Peptide Nanotubes. *Angew. Chem., Int. Ed.* **2014**, *53*, 6866–6881.
 12. Lim, Y. B.; Lee, E.; Lee, M. Cell-Penetrating-Peptide-Coated Nanoribbons for Intracellular Nanocarriers. *Angew. Chem., Int. Ed.* **2007**, *46*, 3475–3478.
 13. Uesaka, A.; Ueda, M.; Makino, A.; Imai, T.; Sugiyama, J.; Kimura, S. Morphology Control between Twisted Ribbon, Helical Ribbon, and

- Nanotube Self-Assemblies with His-Containing Helical Peptides in Response to pH Change. *Langmuir* **2014**, *30*, 1022–1028.
14. Mondal, J. H.; Ahmed, S.; Ghosh, T.; Das, D. Reversible Deformation–Formation of a Multistimuli Responsive Vesicle by a Supramolecular Peptide Amphiphile. *Soft Matter* **2015**, *11*, 4912–4920.
 15. Black, M.; Trent, A.; Kostenko, Y.; Lee, J. S.; Olive, C.; Tirrell, M. Self-Assembled Peptide Amphiphile Micelles Containing a Cytotoxic T-Cell Epitope Promote a Protective Immune Response *In Vivo*. *Adv. Mater.* **2012**, *24*, 3845–3849.
 16. Rad-Malekshahi, M.; Visscher, K. M.; Rodrigues, J. P. G. L. M.; de Vries, R.; Hennink, W. E.; Baldus, M.; Bonvin, A. M. J. J.; Mastrobattista, E.; Weingarth, M. The Supramolecular Organization of a Peptide-Based Nanocarrier at High Molecular Detail. *J. Am. Chem. Soc.* **2015**, *137*, 7775–7784.
 17. Dai, B.; Li, D.; Xi, W.; Luo, F.; Zhang, X.; Zou, M.; Cao, M.; Hu, J.; Wang, W.; Wei, G.; Zhang, Y.; Liu, C. Tunable Assembly of Amyloid-Forming Peptides into Nanosheets as a Retrovirus Carrier. *Proc. Natl. Acad. Sci. U.S.A.* **2015**, *112*, 2996–3001.
 18. Pellach, M.; Atsmon-Raz, Y.; Simonovsky, E.; Gottlieb, H.; Jacoby, G.; Beck, R.; Adler-Abramovich, L.; Miller, Y.; Gazit, E. Spontaneous Structural Transition in Phospholipid-Inspired Aromatic Phosphopeptide Nanostructures. *ACS Nano* **2015**, *9*, 4085–4095.

19. Segman-Magidovich, S.; Lee, M.; Vaiser, V.; Struth, B.; Gellman, S. H.; Rapaport, H. Sheet-Like Assemblies of Charged Amphiphilic α/β -Peptides at the Air-Water Interface. *Chem. —Eur. J.* **2011**, *17*, 14857–14866.
20. Nam, K. T.; Shelby, S. a; Choi, P. H.; Marciel, A. B.; Chen, R.; Tan, L.; Chu, T. K.; Mesch, R. a; Lee, B.-C.; Connolly, M. D.; Kisielowski, C.; Zuckermann, R. N. Free-Floating Ultrathin Two-Dimensional Crystals from Sequence-Specific Peptoid Polymers. *Nat. Mater.* **2010**, *9*, 454–460.
21. Zhang, S.; Holmes, T.; Lockshin, C.; Rich, A. Spontaneous Assembly of a Self-Complementary Oligopeptide to Form a Stable Macroscopic Membrane. *Proc. Natl. Acad. Sci. U.S.A.* **1993**, *90*, 3334–3338.
22. O’Leary, L. E. R.; Fallas, J. A.; Bakota, E. L.; Kang, M. K.; Hartgerink, J. D. Multi-Hierarchical Self-Assembly of a Collagen Mimetic Peptide from Triple Helix to Nanofibre and Hydrogel. *Nat. Chem.* **2011**, *3*, 821–828.
23. Chopko, C. C. M.; Lowden, E. E. L.; Engler, A. A. C.; Griffith; Hammond; Griffith, L. G.; Hammond, P. T.; Paula, T. Dual Responsiveness of a Tunable Thermo-Sensitive Polypeptide. *ACS Macro Lett.* **2012**, *1*, 727–731.
24. Raspa, A.; Saracino, G. a. a.; Pugliese, R.; Silva, D.; Cigognini, D.; Vescovi, A.; Gelain, F. Complementary Co-Assembling Peptides: From

- In Silico* Studies to *In Vivo* Application. *Adv. Funct. Mater.* **2014**, *24*, 6317–6328.
25. Zhuang, X.; Mai, Y.; Wu, D.; Zhang, F.; Feng, X. Two-Dimensional Soft Nanomaterials: A Fascinating World of Materials. *Adv. Mater.* **2015**, *27*, 403–427.
 26. Xue, T.; Peng, B.; Xue, M.; Zhong, X.; Chiu, C.-Y.; Yang, S.; Qu, Y.; Ruan, L.; Jiang, S.; Dubin, S.; Kaner, R. B.; Zink, J. I.; Meyerhoff, M. E.; Duan, X.; Huang, Y. Integration of Molecular and Enzymatic Catalysts on Graphene for Biomimetic Generation of Antithrombotic Species. *Nat. Commun.* **2014**, *5*, 1–6.
 27. Tan, C.; Zhang, H. Wet-Chemical Synthesis and Applications of Non-Layer Structured Two-Dimensional Nanomaterials. *Nat. Commun.* **2015**, *6*, 1–13.
 28. Rao, C. N. R.; Sood, A. K.; Subrahmanyam, K. S.; Govindaraj, A. Graphene: The New Two-Dimensional Nanomaterial. *Angew. Chem., Int. Ed.* **2009**, *48*, 7752–7777.
 29. Robertson, E. J.; Olivier, G. K.; Qian, M.; Proulx, C.; Zuckermann, R. N.; Richmond, G. L. Assembly and Molecular Order of Two-Dimensional Peptoid Nanosheets through the Oil–Water Interface. *Proc. Natl. Acad. Sci. U.S.A.* **2014**, *111*, 13284–13289.
 30. Kory, M. J.; Wörle, M.; Weber, T.; Payamyar, P.; van de Poll, S. W.; Dshemuchadse, J.; Trapp, N.; Schlüter, A. D. Gram-Scale Synthesis of

- Two-Dimensional Polymer Crystals and Their Structure Analysis by X-Ray Diffraction. *Nat. Chem.* **2014**, *6*, 779–784.
31. Musevic, I.; Skarobot, M.; Tkalec, U.; Ravnik, M.; Zumer, S. Two-Dimensional Nematic Colloidal Crystals Self-Assembled by Topological Defects. *Science* **2006**, *313*, 954–958.
 32. Kunitake, T. Synthetic Bilayer Membranes: Molecular Design, Self-Organization, and Application. *Angew. Chem., Int. Ed.* **1992**, *31*, 709–726.
 33. Knowles, T. P. J.; Oppenheim, T. W.; Buell, A. K.; Chirgadze, D. Y.; Welland, M. E. Nanostructured Films from Hierarchical Self-Assembly of Amyloidogenic Proteins. *Nat. Nanotechnol.* **2010**, *5*, 204–207.
 35. Mannige, R. V.; Haxton, T. K.; Proulx, C.; Robertson, E. J.; Battigelli, A.; Butterfoss, G. L.; Zuckermann, R. N.; Whitlam, S. Peptoid Nanosheets Exhibit a New Secondary-Structure Motif. *Nature* **2015**, 2–9.
 36. Pashuck, E. T.; Stupp, S. I. Direct Observation of Morphological Transformation from Twisted Ribbons into Helical Ribbons. *J. Am. Chem. Soc.* **2010**, *132*, 8819–8821.
 37. Smith, A. M.; Williams, R. J.; Tang, C.; Coppo, P.; Collins, R. F.; Turner, M. L.; Saiani, A.; Ulijn, R. V. Fmoc-Diphenylalanine Self Assembles to a Hydrogel via a Novel Architecture Based on π - π Interlocked β -Sheets. *Adv. Mater.* **2008**, *20*, 37–41.

38. Morris, K. L.; Zibae, S.; Chen, L.; Goedert, M.; Sikorski, P.; Serpell, L. C. The Structure of Cross- β Tapes and Tubes Formed by an Octapeptide, α S β 1. *Angew. Chemie - Int. Ed.* **2013**, *52*, 2279–2283.
39. De Santis, E.; Ryadnov, M. G. Peptide Self-Assembly for Nanomaterials: The Old New Kid on the Block. *Chem. Soc. Rev.* **2015**, *44*, 8288–8300.
40. Jang, H.-S.; Lee, J.-H.; Park, Y.-S.; Kim, Y.-O.; Park, J.; Yang, T.-Y.; Jin, K.; Lee, J.; Park, S.; You, J. M.; Jeong, K.-W.; Shin, A.; Oh, I.-S.; Kwon, M.-K.; Kim, Y.-I.; Cho, H.-H.; Han, H. N.; Kim, Y.; Chang, Y. H.; Paik, S. R. *et al.* Tyrosine-Mediated Two-Dimensional Peptide Assembly and Its Role as a Bio-Inspired Catalytic Scaffold. *Nat. Commun.* **2014**, *5*, 3665.
41. Kiefer, W. Recent Advances in Linear and Nonlinear Raman Spectroscopy I. *J. Raman Spectrosc.* **2007**, *38*, 1538–1553.
42. Tuma, R. Raman Spectroscopy of Proteins: From Peptides to Large Assemblies. *J. Raman Spectrosc.* **2005**, *36*, 307–319.
43. M. Siamwiza, R. Lord, M. Chen, *Biochemistry* 1975, *14*, 4870–4876.
44. E. B. Wilson, *Phys. Rev.* 1934, *45*, 706–714.
45. E. Podstawka, A. Kudelski, P. Kafarski, L. M. Proniewicz, *Surf. Sci.* 2007, *601*, 4586–4597
46. M. C. Chen, R. C. Lord, *Biochemistry* 1976, *15*, 1889–1897.
47. C. N. Pace, G. Horn, E. J. Hebert, J. Bechert, K. Shaw, L. Urbanikova, J. M. Scholtz, J. Sevcik, *J. Mol. Biol.* 2001, *312*, 393–404.

48. Beychok, S. Circular Dichroism of Biological Macromolecules. *Science* **1966**, *154*, 1288–1299.
49. Goodman, M.; Toniolo, C.; Peggion, E. Conformational Aspects of Polypeptides. XXIX. Conformational Assignments for Some Aromatic Polypeptides by Far-UV Cotton Effects. New Results. *Biopolymers* **1968**, *6*, 1691–1695.
50. Beychok, S.; Fasman, G. D. Circular Dichroism of Poly-L-Tyrosine*. *Biochemistry* **1964**, *3*, 1675–1678.
51. Chen, Y. H.; Lo, T. B.; Yang, J. T. Optical Activity and Conformation of Cobra Neurotoxin. *Biochemistry* **1977**, *16*, 1826–1830.
52. Cameron, D. L.; Tu, a T. Characterization of Myotoxin a from the Venom of Prairie Rattlesnake (*Crotalus Viridis Viridis*). *Biochemistry* **1977**, *16*, 2546–2553.
53. Timasheff, S. N.; Bernardi, G. Studies on Acid Deoxyribonuclease: VII. Conformation of Three Nucleases in Solution. *Arch. Biochem. Biophys.* **1970**, *141*, 53–58.
54. Polese, A.; Formaggio, F.; Crisma, M.; Valle, G.; Toniolo, C.; Bonora, G. M.; Broxterman, Q. B.; Kamphuis, J. Peptide Helices as Rigid Molecular Rulers: A Conformational Study of Isotactic Homopeptides from α -Methyl- α -Isopropylglycine, [L-(α Me)Val]_n. *Chem.—Eur. J.* **1996**, *2*, 1104–1111.
55. Toniolo, C.; Polese, a; Formaggio, F.; Crisma, M.; Kamphuis, J. Circular

- Dichroism Spectrum of a Peptide 3_{10} -Helix. *J. Am. Chem. Soc.* **1996**, *118*, 2744–2745.
56. Yoder, G.; Polese, A.; Silva, R. A. G. D.; Formaggio, F.; Crisma, M.; Broxterman, Q. B.; Kamphuis, J.; Toniolo, C.; Keiderling, T. A. Conformational Characterization of Terminally Blocked L-(α Me)Val Homopeptides Using Vibrational and Electronic Circular Dichroism. 3_{10} -Helical Stabilization by Peptide–Peptide Interaction. *J. Am. Chem. Soc.* **1997**, *119*, 10278–10285. Fasman, G. D. Poly- α -Amino Acids. In *Protein Models for Conformational Studies*. Marcel Dekker: New York, **1967**.
57. Kurapkat, G.; Krüger, P.; Wollmer, a; Fleischhauer, J.; Kramer, B.; Zobel, E.; Koslowski, a; Botterweck, H.; Woody, R. W. Calculations of the CD Spectrum of Bovine Pancreatic Ribonuclease. *Biopolymers* **1997**, *41*, 267–287.
58. Goux, W. J.; Hooker, T. M. Chiroptical Properties of Proteins. 1. Near-Ultraviolet Circular Dichroism of Ribonuclease S. *J. Am. Chem. Soc.* **1980**, *156*, 7080–7087.
59. Woody, R. W.; Dunker, A. K. Aromatic and Cystine Side-Chain Circular Dichroism in Proteins. In *Circular Dichroism and the Conformational Analysis of Biomolecules*. Plenum Press: New York, **1996**; pp. 109–157.
60. Wütrich, K. *NMR of Proteins and Nucleic Acids*, John Wiley & Sons: New York, **1986**.

61. J. Cavanagh, W. J. Fairbrother, A. G. Palmer, M. Rance, N. J. Skelton, *Protein NMR Spectroscopy: Principles and Practice*, Elsevier Academic Press, 2nd Ed. **2007**.
62. Zarbock, J.; Clore, G. M.; Gronenborn, a M. Nuclear Magnetic Resonance Study of the Globular Domain of Chicken Histone H5: Resonance Assignment and Secondary Structure. *Proc. Natl. Acad. Sci. U.S.A.* **1986**, *83*, 7628–7632.
63. Bax, A. Two-Dimensional NMR and Protein Structure. *Annu. Rev. Biochem.* **1989**, *58*, 223–256.
64. Guntert, P. Automated NMR Structure Calculation with CYANA. *Methods. Mol. Biol.* **2004**, *278*, 353–78.
65. A. Moustatih and A. Garnier-suillerot, *J. Med. Chem.*, 1989, **32**, 1426–1431.
66. R. P. Briñas, M. Hu, L. Qian, E. S. Lyman and J. F. Hainfeld, *J. Am. Chem. Soc.*, 2008, **130**, 975–982.
67. C. F. Shaw, N. A. Schaeffer, R. C. Elder, M. K. Eidsness, J. M. Trooster and G. H. M. Calis, *J. Am. Chem. Soc.*, 1984, **106**, 3511–3521.
68. C. Houée-Lévin, K. Bobrowski, L. Horakova, B. Karademir, C. Schöneich, M. J. Davies and C. M. Spickett, *Free Radic. Res.*, 2015, **49**, 347–373.

69. Q. Wang, Q. Wang, M. Li, S. Szunerits and R. Boukherroub, *New J. Chem.*, 2016, **40**, 5473–5482.
70. J. Kwak, S. I. Park and S. Y. Lee, *Colloids Surf. B Biointerfaces*, 2013, **102**, 70–75.
71. P. R. Selvakannan, A. Swami, D. Srisathiyarayanan, P. S. Shirude, R. Pasricha, A. B. Mandale and M. Sastry, *Langmuir*, 2004, **20**, 7825–7836.
72. A. Barth, *Prog. Biophys. Mol. Biol.*, 2000, **74**, 141–173.
73. J. Kong and S. Yu, *Acta Biochim. Biophys. Sin.*, 2007, **39**, 549–559.
74. Rapaport, H.; Kjaer, K.; Jensen, T. R.; Leiserowitz, L.; Tirrell, D. A. Two-Dimensional Order in β -Sheet Peptide Monolayers. *J. Am. Chem. Soc.* **2000**, *122*, 12523–12529.
75. Lamm, M. S.; Rajagopal, K.; Schneider, J. P.; Pochan, D. J. Laminated Morphology of Nontwisting β -Sheet Fibrils Constructed *via* Peptide Self-Assembly. *J. Am. Chem. Soc.* **2005**, *127*, 16692–16700.
76. Benzinger, T. L.; Gregory, D. M.; Burkoth, T. S.; Miller-Auer, H.; Lynn, D. G.; Botto, R. E.; Meredith, S. C. Two-Dimensional Structure of β -Amyloid(10-35) Fibrils. *Biochemistry* **2000**, *39*, 3491–3499.
77. Hughes, M.; Xu, H.; Frederix, P. W. J. M.; Smith, A. M.; Hunt, N. T.; Tuttle, T.; Kinloch, I. A.; Ulijn, R. V. Biocatalytic Self-Assembly of 2D Peptide-Based Nanostructures. *Soft Matter* **2011**, *7*, 10032–10038.
78. Aggeli, a; Fytas, G.; Vlassopoulos, D.; McLeish, T. C.; Mawer, P. J.;

- Boden, N. Structure and Dynamics of Self-Assembling β -Sheet Peptide Tapes by Dynamic Light Scattering. *Biomacromolecules* **2001**, *2*, 378–388.
79. Mondal, S.; Adler-Abramovich, L.; Lampel, A.; Bram, Y.; Lipstman, S.; Gazit, E. Formation of Functional Super-Helical Assemblies by Constrained Single Heptad Repeat. *Nat. Commun.* **2015**, *6*, 8615.

Chapter 3. Proton conduction in a tyrosine-rich peptide/manganese oxide hybrid nanofilm

3.1 Introduction

Proton conduction in biological systems has been an important issue for a better understanding of fundamental life processes. The most well-known examples are adenosine triphosphate synthesis driven by proton pumps across mitochondrial membrane,¹ light-activated proton pumping of bacteriorhodopsin in Archaea,² and voltage-regulated proton channels triggering bioluminescence in jellyfish.³ Along with those long-range proton translocations, several biochemical reactions are closely related to proton transfer represented by proton-coupled electron transfer (PCET) occurring in photosystem II⁴ and ribonucleotide reductases.⁵ In the reactions, enzymes are in charge of facilitating the transport of electrons and protons simultaneously by using redox active amino acids such as tyrosine and tryptophan in their active site.⁶

Earlier research on proton transfer in bio-systems usually focused on

structural components at the molecular scale and suggested that exquisitely assembled water-wires and redox cofactors are indispensable to moving protons efficiently and selectively. Recently, bulk proton conduction within bioorganic materials has also been investigated. Polysaccharides functionalized with acid and base groups work as a good proton conductor in protonic field-effect transistor.⁷ Drop-casted reflectin protein films exhibit proton conductivity of 0.1 mS cm^{-1} , and it is suggested that amino acids having a carboxylic group play proton-donation or hydrogen-bond roles based on protein mutation experiments.⁸ Similarly, it was reported that shark ampullae jelly films containing a mixture of proteins and polyglycans show high proton conductivity of 2 mS cm^{-1} , which may originate from several hydrophilic groups and a sulfate group.⁹ Recent research on pigmentary biopolymers in organismal eumelanin has offered another interesting point regarding the role of proton conduction in charge transport.^{10,11} Upon absorption of water, free charge carriers, radicals and protons are generated from comproportionation reactions. Such chemical self-doping can dramatically increase hybrid electronic-protonic conductivity. However, the proton conductivity of the reported biological materials is very low compared to synthetic materials.

Proton-conducting materials are essential components of modern energy devices.^{12,13} Owing to technological needs, research on proton conduction has encompassed a broad range of materials such as ceramic oxides,^{14,15} solid acids,^{16,17} metal-organic frameworks¹⁸⁻²³ and polymeric

membranes, the most common of which is Nafion.²⁴ Hybrid composite materials have been investigated as another candidate because the introduction of hygroscopic inorganic oxides or acids into an organic matrix has potential advantages such as enhancing water absorption, proton conductivity, and mechanical and chemical stability. For example, heteropolyacids have been extensively adopted as solid conducting fillers due to the high availability of conducting protons within them.²⁵ Hydrophilic particles such as metal oxides,^{26,27} metal phosphate,²⁸ and zeolites²⁹ have been incorporated to modify the water uptake behaviour of the original polymer membrane. The consequence properties are usually more than simply the sum of its individual contribution, which are originated from extensive hybrid interface.^{30,31}

This study focused on the synergistic effect of a short peptide and inorganic oxides on proton conduction. Indeed, several amino acids take an active part as proton transporters in biological systems. In particular, amino acids having a phenol group, such as tyrosine (Tyr, Y), have been known to play a critical role in PCET interplaying with a manganese-calcium cluster in photosystem II and a di-iron cluster in ribonucleotide reductase.^{32,33} Additionally, tyrosine can be oxidized and polymerized into eumelanins,³⁴ which show hydration-dependent electrical current and high proton conductivity. (Figure 2.1) Taking advantages of the characteristics of tyrosine, here, we developed a new facile strategy for fabricating peptide/manganese oxide hybrid films. Peptide films were fabricated by using spin-coating, and the

films were immersed in KMnO_4 aqueous solution to induce crosslinking of tyrosine and hybridization with manganese oxide simultaneously. The advantages of this method are the uniformity of the film, the availability of large scale deposition, room temperature processing, thickness control, and expandability to other peptide sequences. Previously, we showed that the YYACAYY (Tyr-Tyr-Ala-Cys-Ala-Tyr-Tyr) peptide can assemble into giant nanosheets at an air/water interface.³⁵ The two-dimensional (2D) nanostructure has a strong driving force that flattens the top of the water droplet into a flat plane. Interestingly, dimerization by disulfide bonds between cysteines changes the morphology of the assembled structure and its secondary conformation. According to 2D nuclear magnetic resonance spectroscopy and circular dichroism analysis, it was found that the assembled peptide sheets had helical conformation despite the fact that the length of the sequence was generally too short to fold into a helix.³⁶ Moreover, tyrosines in the peptide sheets can catalytically trigger pyrrole polymerization, resulting in free-standing hybrid films of polypyrrole and peptides. In an effort to investigate the potential of tyrosine-rich peptide films with redox-active functions, herein, we examine the proton conductivity of tyrosine-rich peptide films when hybridized with manganese oxides by using the peptide sequence YYACAYY.

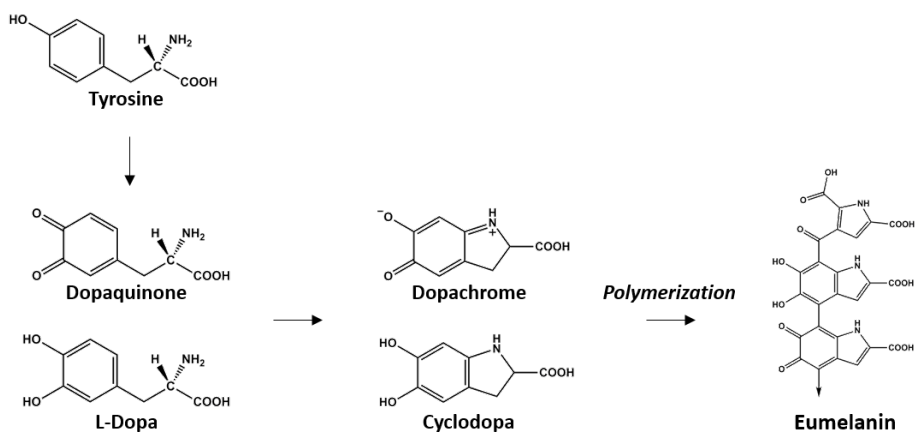


Figure 3.1 A Scheme for the natural polymerizing process of eumelanin

3.2 Experimental Procedure

3.2.1 Chemicals

All peptides (98 % purity) were purchased from GL Biochem (Shanghai, China) and used without further purifications. Potassium permanganate (≥ 99.0 % purity) and 1,1,1,3,3,3-Hexafluoro-2-propanol (99 % purity) were purchased from Sigma-Aldrich and Acros organics, respectively.

3.2.2 Fabrication of peptide/MnO_x hybrid nanofilm devices

Two-terminal devices were fabricated on either quartz or SiO₂/Si substrates. Prior to fabrication, SiO₂/Si substrates were cleaned in Piranha solution, and quartz substrates were cleaned by sequential sonication in acetone, methanol, and deionized water. 1 wt% of YYACAYY peptide were dissolved in HFIP. The solution was heated at 50°C for 30 min to completely dissolve the peptide. The solution was spin-coated onto the substrate at the spin rate of 2000 rpm and the holding time of 30 sec. The residual solvent was evaporated by mild annealing at 120°C for 30 min. The coated substrate was dipped into a KMnO₄ solution with mild stirring (100 rpm). After the reaction, the sample

was washed with deionized water with several times. Next, arrays of paired electrodes that consisted of a 5 nm chromium adhesion layer overlaid with either a 45 nm gold or a 45 nm palladium layer were electron-beam evaporated onto the substrates through a shadow mask. To form proton-injecting PdH_x electrodes, the Pd electrodes were exposed to a 5% H₂/95% argon atmosphere *in situ*.

3.2.3 Characterization

3.2.3.1 Electrical Characterization

The completed devices were characterized electrically in multiple distinct configurations. DC measurements on SiO₂/Si substrates was conducted by Agilent 4156C semiconductor analyzer. AC measurements on quartz substrates was conducted by Agilent 4294A impedance analyzer. The humidity was monitored constantly with a hygrometer during all electrical experiments. The Nyquist plot was obtained using the frequency range from 100 Hz to 110 MHz with a constant applied voltage of 100 mV.

3.2.3.2 Atomic force microscopy (AFM) analysis

AFM analysis were carried out with Bruker AFM multimode 8. The used probes for AFM were Antimony doped (n) silicon cantilevers with a spring constant of 40 Nm⁻¹ (Bruker) and the resonance frequency of 300 kHz. The observation condition was tapping mode and a scan rate was 0.9 Hz.

3.2.3.3 Transmission electron microscopy (TEM) analysis

The micrographs and selected area electron diffraction (SAED) patterns were obtained using a JEOL JEM-3000F FEG TEM instrument with an acceleration voltage of 200 kV.

3.2.3.4 X-ray photo-electron spectroscopy (XPS)

X-ray photo-electron spectroscopy (XPS) spectra were obtained by electron spectroscopy (PHI 5000 VersaProbe™, ULVAC-PHI) with a pass energy of 23.5 eV and a step size of 0.05 eV. All the binding energies are referenced to C 1s (284.5 eV).

3.2.3.6 Inductively coupled plasma mass spectroscopy (ICP-ms)

Analysis was carried out with NexION 350D and Perkin-Elmer SCIEX. The source was argon plasma (6000K) and the range of mass resolution was 0.3-3.0 amu. Its detection limit was 9Be<15ppt, 59 Co<2 ppt, 115In<0.5ppt. RF Power was 1100W and injection was performed with flow rate of 1.00 ml/min.

3.2.3.7 X-ray absorption near edge structure (XANES) analysis

Mn K-edge X-ray absorption spectra of peptide/manganese oxide hybrid film, X-ray absorption near edge structure (XANES), and extended X-ray absorption fine structure (EXAFS), were collected on the BL10C beam line (WEXAFS) at the Pohang light source (PLS-II) with top-up mode operation under a ring current of 350 mA at 3.0 GeV. From the high-intensity X-ray photons of the multipole wiggler source, monochromatic X-ray beams could be obtained using a liquid-nitrogen-cooled double-crystal monochromator (Bruker ASC) with available *in situ* exchange in vacuum between a Si(111) and Si(311) crystal pair. The Si(111) crystal pair was used for Mn K-edge XAFS measurements (absorption edge energy, 6539 eV). Higher-order harmonic contaminations were eliminated by detuning to reduce the incident X-ray intensity by ~30%. Energy calibration was simultaneously carried out for each measurement with reference Mn foil placed in front of the third ion chamber. The data reductions of the experimental spectra to normalized XANES and Fourier-transformed radial distribution functions (RDFs) were performed through the standard XAFS procedure.

3.2.3.8 Fourier transform infrared spectroscopy (FT-IR) analysis

FT-IR spectra of the hybrid film were analyzed with a Thermo Nicolet 6,700 FT-IR spectrometer equipped with an attenuated total reflection accessory. The scanned wave numbers ranged from 750 to 3,750 cm^{-1} at a resolution of 1.93 cm^{-1} . The spectra were scanned 4 times. The hybrid film was prepared on silicon oxide wafer and placed on a ZnSe/diamond. To obtain sufficient signal, 40 batches under the same condition were transferred to the substrate.

3.2.3.9 Thermal gravimetric analysis (TGA)

Thermo gravimetric measurements were performed with a Q 5000 IR TGA instrument (TA Instruments). High-temperature platinum pans loaded with 15 mg samples were used for the tests. All samples, previously dried to remove the adsorbed water by lyophilization, was heated from room temperature to 400 $^{\circ}\text{C}$ with a heating rate of 5 $^{\circ}\text{C min}^{-1}$ in air condition.

3.3 Results and Discussions

3.3.1 Morphology and structural analysis of the hybrid film

Tyrosine-containing peptide was hybridized with manganese oxide by using potassium permanganate and their characterizations were carried out. A reaction of tyrosine oxidation was used to involve manganese component into peptide film. A process for fabrication of these peptide-inorganic hybrid film was schematized in figure 1a. A 40 μL drop of YYACAYY peptide solution in HFIP (160 mg mL^{-1}) was placed on a cleaned quartz. To allow evaporation of the residual solvent, the peptide film was annealed $150 \text{ }^\circ\text{C}$ for 30 minutes. After then the film was immersed into 30 mM solution of potassium permanganate (KMnO_4) in deionized water for 15 minutes, in which a deposition of manganese oxide (MnO_x) occurred in the film and peptide/ MnO_x hybrid composite were made as products. (Figure 3.2) The hybrid film was rinsed with deionized water three times to remove the remaining solution in it and water on surface was eliminated with nitrogen blower. (Figure 3.3) The transparent peptide film had a thickness undulation along the flow direction (Figure 3.4b,c), but the surface of the peptide film exhibited a smooth topography with a root mean square roughness of 2.7 nm within microscopic area. Its thickness was

determined to be nearly $120 \text{ nm} \pm 15 \text{ nm}$. After evaporation of residual solvent by mild annealing, the film was immersed in potassium permanganate (KMnO_4) aqueous solution, in which oxidation of tyrosines and hybridization of peptide/manganese oxide occurred. The transparent peptide film became a brownish translucent hybrid film (Figure 3.4b,c,f,g). Noticeable differences were also observed in the microstructure of the film investigated by AFM (Figure 3.4d,h) and cross-section transmission electron microscopy (TEM) (Figure 3.4e,i), which showed that interposing of MnO_x into the peptide layers roughened the surface of the film.

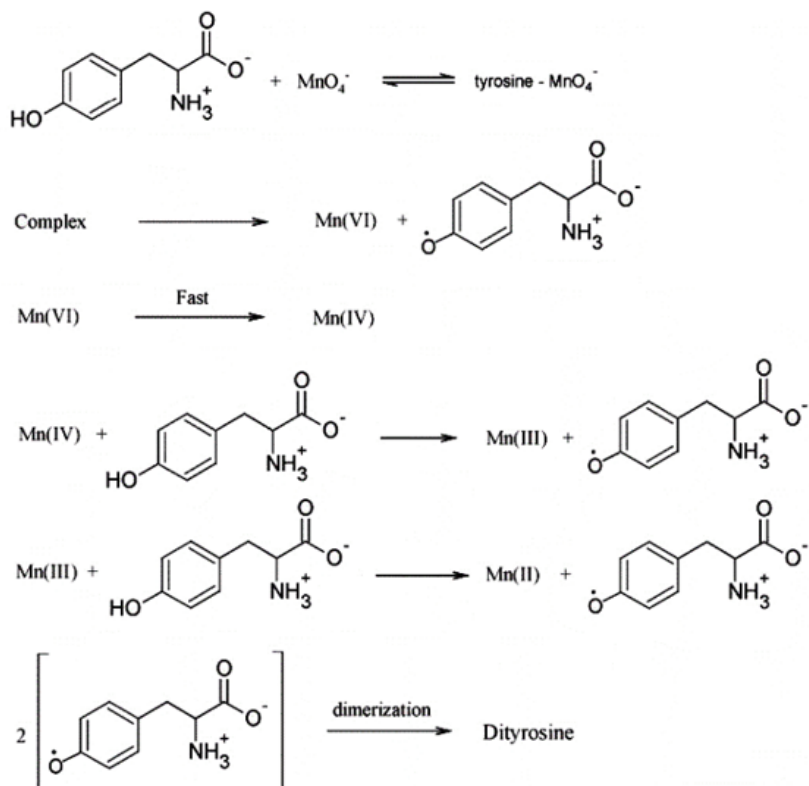


Figure 3.2 Scheme for synthesis of dityrosine using KMnO_4

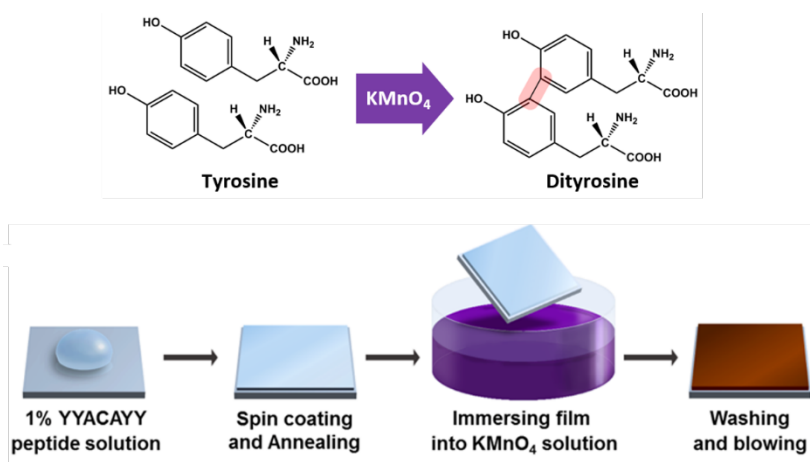


Figure 3.3 Schematic diagram describing the fabrication process of peptide/manganese oxide hybrid film.

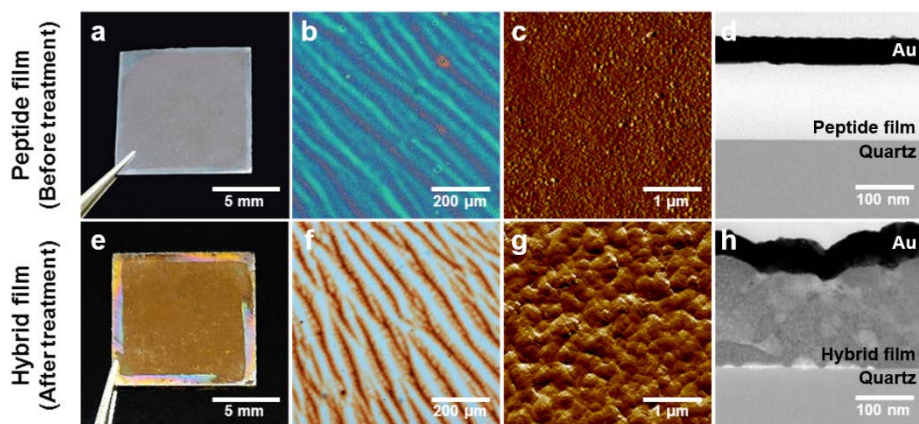


Figure 3.4 A comparison of the film before and after KMnO_4 treatment by optical images (a,e), optical microscopy images (b,f), atomic force microscopy (AFM) images (c,g) and transmission electron microscopy (TEM) images (d,h)

3.3.2 Characterizations of manganese oxides

Further detailed investigations were done for each component in peptide/MnO_x hybrid film. In this study, the electron microscopy and various spectroscopic tools were employed to analyze the materials including high resolution transmission electron microscopy (HR-TEM), x-ray absorption near-edge structure (XANES), ultraviolet-visible spectroscopy (UV-vis), and photoluminescence spectroscopy (PL).

Manganese components were analyzed with HR-TEM and XANES. In observation of high resolution TEM images (Figure 3.5) it was founded that crystalline MnO_x particles were embedded in peptide film and their diameter were 4~12 nm. Clear lattice fringes observed in HRTEM and the corresponding fast Fourier transform (FFT) diffraction pattern revealed the crystallinity and structural phase of the synthesized MnO_x. The values of interlayer spacing and points in the FFT patterns accord with the phases of Mn₃O₄, MnO, and Mn₂O₃. These results suggested that the hybrid film composed with various kinds of partially crystalline MnO_x. To understand the chemical nature of MnO_x in hybrid film, we carried out X-ray absorption spectroscopy which provides information about molecular structure and valence state of the materials. Based on Edge shift data from the K-edge XANES spectra of the film and other representative manganese oxides (Figure 3.6), the average valence of

manganese in the film was calculated 3.28. We also carried out X-ray photoelectron spectroscopy (XPS) to identify the Mn valence state. Figure 2b shows the deconvolution of the Mn2p XPS spectrum. A spin-orbit doublet of Mn2p_{1/2} and Mn2p_{3/2} with a binding energy gap of 11.5 eV was observed in the Mn 2p spectrum. The deconvoluted Mn2p spectrum shows four peaks with binding energies of 640.6 eV, 641.8 eV, 643.0 eV, and 644.6 eV, which correspond to Mn²⁺, Mn³⁺, Mn⁴⁺, and a shakeup peak, respectively. The shakeup peak that is typical of Mn²⁺ originates from charge transfer from the outer electron shell to an unoccupied orbit with higher energy during the photoelectron process.³⁷ It can be seen that Mn²⁺ and Mn³⁺ are dominant species with relative intensities of 40% and 36%, respectively, with a small amount of Mn⁴⁺. It is intriguing that several manganese oxides having various oxidation states coexist in the hybrid film while MnO₂ has been known as the main product of the oxidative reaction using KMnO₄ with organic components.³⁸⁻⁴⁰ An energy-dispersive X-ray spectroscopy (EDX) mapping analysis of the film's cross-section showed that MnO_x was formed in both the interior and the surface of the hybrid film, indicating that water and ions can easily diffuse into the inner structure of the film. (Figure 3.7) The results showed MnO_x were formed throughout the film and they accounted for 30.5 % of the hybrid film which confirmed by inductively coupled plasma - mass spectroscopy (ICP-MS) (Table 3.1).

Peptide before and after KMnO₄ treatment were studied with several

spectroscopic tools. In Figure 3.8, the only peak was observed at 280 nm in peptide film which is a known value of tyrosine and it came from aromatic side chain of tyrosine.⁴⁴ In spectrum of the hybrid film it was founded that this peak was remaining after reacting with KMnO_4 , which indicated that products still had 4-hydroxyphenyl group. Broadening of its bandwidth up to ~320 nm was ascribing to formation of extended π -conjugate system and it has been known that the amount of this red shift depends on the degree of conjugation in the molecule.^{45,46} Importantly, a new absorbance appeared at approximately 400 nm with a broad and wide shoulder that originated from manganese oxide.⁴⁷⁻⁴⁹ The wide plateau region between 350 and 410 nm was mainly attributed to the allowed $\text{O}^{2-} \rightarrow \text{Mn}^{2+}$ and $\text{O}^{2-} \rightarrow \text{Mn}^{3+}$ ligand-to-metal charge transfer transition, and the broad shoulder peak up to 700 nm was related to d-d crystal field transitions.⁴⁸⁻⁵⁰

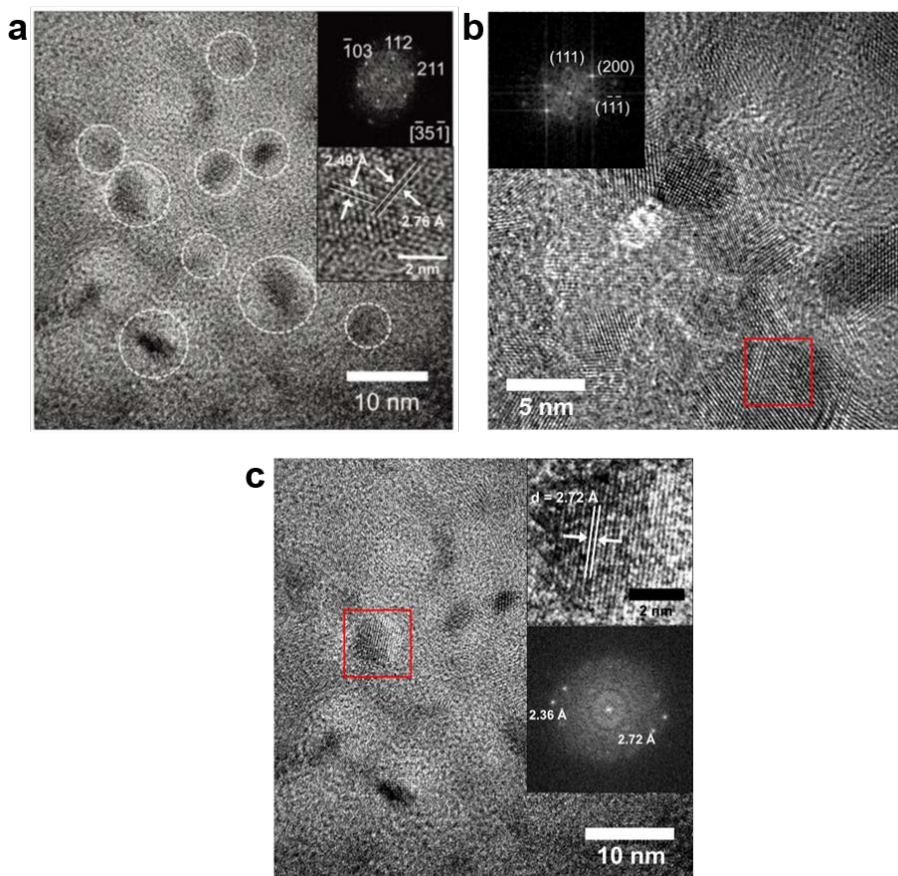


Figure 3.5 HRTEM images of the hybrid film (a) FFT diffraction clearly shows Mn_3O_4 phase. (b) FFT diffraction clearly shows MnO phase. (c) d-spacing value of the lattice fringes is matched with the major diffraction peak of Mn_2O_3 phase though other diffraction spot related to other plane didn't appear in FFT diffraction pattern.

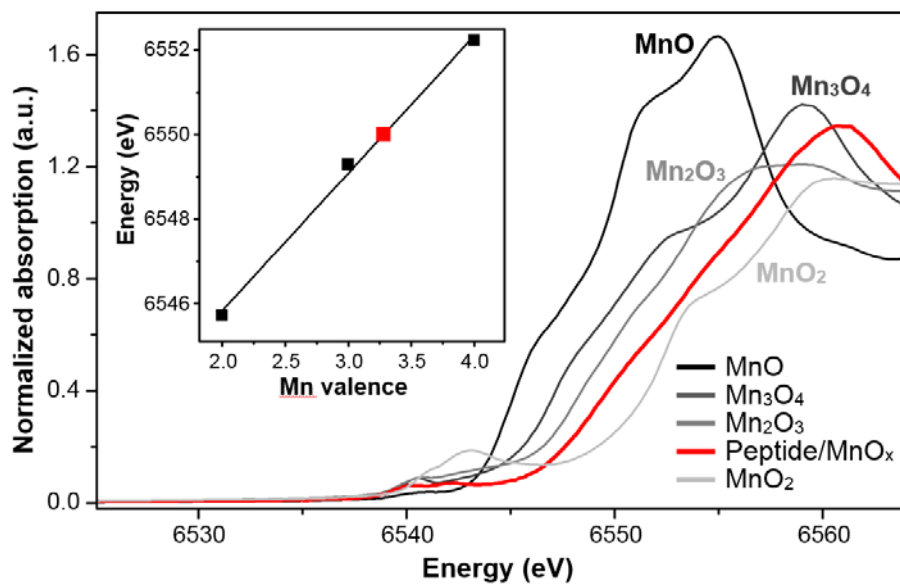


Figure 3.6 X-ray absorption near edge structure (XANES) spectra at the Manganese (Mn) K-edge for various Manganese oxide and the hybrid film. The inset is a fitted linear relationship between energy and oxidation state of Mn.

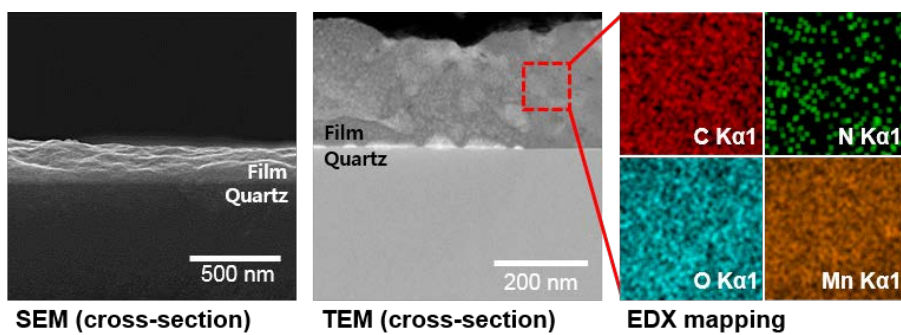


Figure 3.7 Energy-dispersive X-ray spectroscopy (EDX) mapping in TEM images of a thin sample milled by focused ion beam (FIB)

ICP-MS Data Sheet	
Sample	Mn
Mn-Peptide	269585704.3
*All samples were analyzed three times and averaged(Mean).	

Table 3.1 The concentration of elements in samples (ppb= $\mu\text{g}/\text{kg}$).

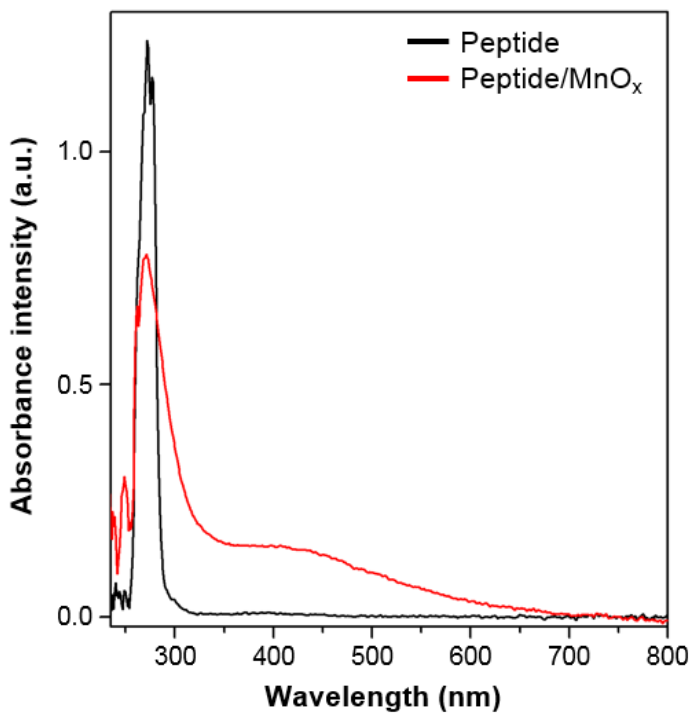


Figure 3.8 UV-VIS spectra of peptide film (black) and hybrid film (red)

3.3.3 Characterizations of peptide in hybrid films

The peptides before and after KMnO_4 treatment were studied with spectroscopic tools. Generally, oxidation reactions of tyrosine and the oxidation products depend on an oxidizing agent, the pH and the condition of the reaction mixture.^{41,42} It is reported that oxidation of tyrosine using permanganate proceeds via a one-electron redox mechanism resulting in the formation of a tyrosyl radical.⁴³ The generated radical can induce radical coupling and yield an ortho-ortho dimer, dityrosine, due to the bulky substituent in the para position. In addition, since radical species are highly reactive, they can couple with other positions to yield a variety of oxidation products. In Figure 3.8, the only peak in the peptide film was observed at 280 nm, corresponding to tyrosine absorption.⁴⁴ In the absorption spectrum of the hybrid film, the peak at 280 nm still existed with decreased intensity, indicating that the hybrid film had the phenolic group of tyrosine. As we mentioned in the previous part, broadening of its bandwidth up to 320 nm implied formation of an extended pi conjugate system, while the extent of this redshift depends on the degree of conjugation in the molecule.^{45,46}

To investigate tyrosine derivatives formed after KMnO_4 treatment and find direct evidence of extended conjugation in the molecule, photoluminescence (PL) properties were measured. As shown in Figure 3.9, in

situ PL emission spectra of 280 nm and 350 nm excitation were collected by titration of a KMnO_4 solution into the peptide solution. In the emission scan spectrum from excitation at 280 nm, a band appeared at 305 nm that is characteristic of tyrosine⁵¹, and its intensity was decreased by increasing the quantity of KMnO_4 solution. In accordance with UV-vis data, this result indicates that the amount of tyrosine decreases during KMnO_4 treatment. At the same time, upon excitation at 350 nm, the fluorescence spectrum of the products displayed new emission bands with gradual enhancement of their peak intensity during the reaction. The region of 410–415 nm in the emission spectrum has been used for detecting the existence of dityrosine fluorometrically.⁵² Additionally, Fourier transform infrared (FT-IR) analysis shows that there are changes related to substitution in the benzene ring and hydroxyl group of phenol (Figure 3.10). These results clearly confirmed that dityrosine was formed during the oxidation reaction, and they also correlate with the UV-vis analysis, suggesting the formation of an extended conjugate system.

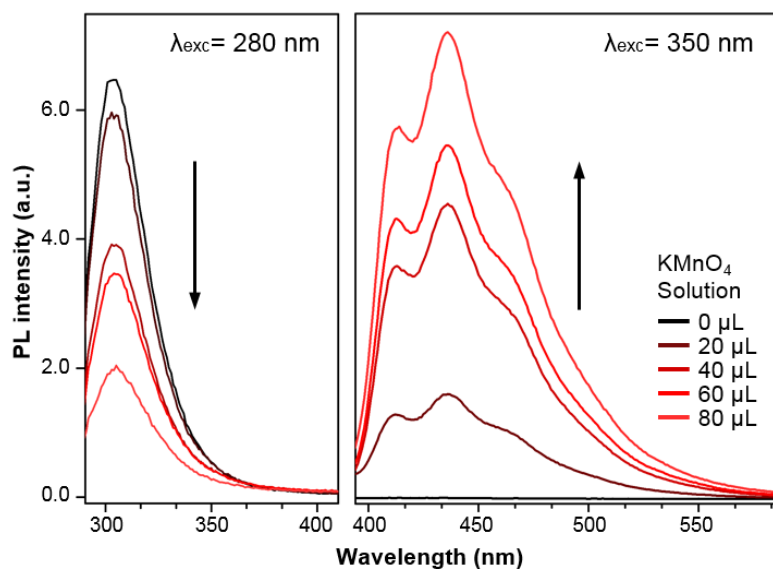


Figure 3.9 Photoluminescence spectrum of 280 nm and 350 nm excitation recorded by titration of KMnO_4 solution. The color changed from black (peptide only) to red.

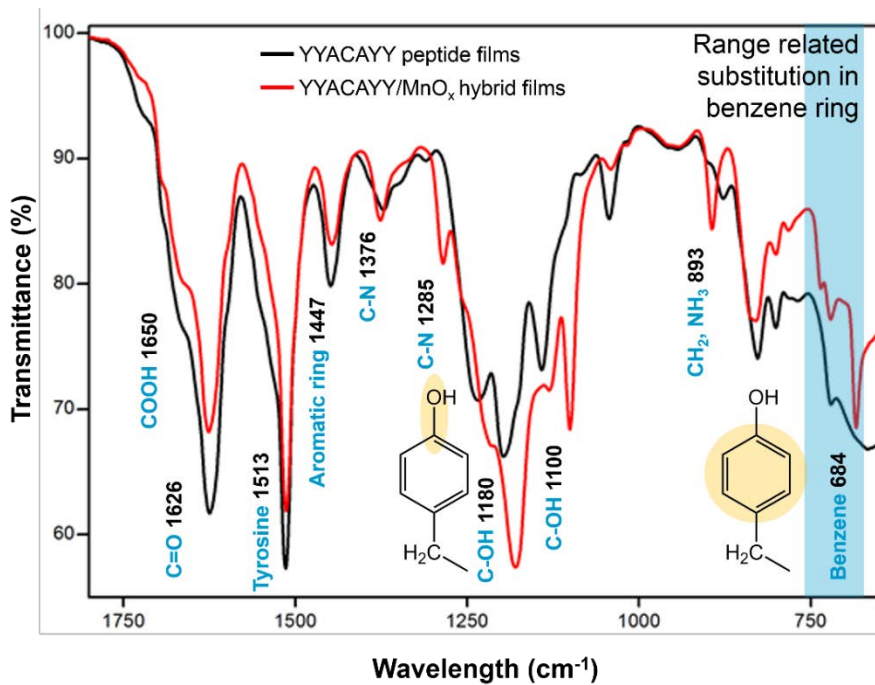
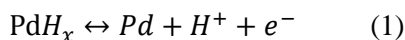


Figure 3.10 FT-IR measurements of the peptide film and the hybrid film

3.3.4 Electrical property of hybrid films depending on humidity

To characterize the electrical response of the hybrid film, we performed current voltage (I-V) measurements in planar two-electrode configuration with gold contacts and palladium (Pd) contacts (Figure 2.10). To prevent the effect of water electrolysis, the maximum applied voltage was limited to 1 V, the thermoneutral voltage of which is known to be 1.5 V. Palladium hydride (PdH_x) electrodes are considered to be suitable metal for measuring protonic current with their ability to inject and drain protons,^{7,54} whereas conventional ion-blocking metal induces significant hysteresis due to accumulation of ion species at the interface.^{8,11} According to an electrochemical reaction (Equation 1),



the hydrogenated palladium facilitates a quantity of protonic movement by completing the circuit for the injected proton with the involved electron from the reaction. Upon I-V measurement, the device was exposed to 5% hydrogen/95% argon gas, which ensured the formation of PdH_x electrical contacts *in situ* (Figure 3.11). While voltage was applied to the device from -1.0 V to +1.0 V, the current was recorded under conditions with a certain degree of relative humidity (RH) from vacuum to 90% RH. As shown in Figure 3.10, the conductivity of the film was found to be highly affected by RH, and the film became more conductive as the surroundings became more humid, which

agrees with the behaviour of other reported water-mediating proton conductors.^{7,8,24} When I-V measurements were performed using proton blocking gold contacts, hysteresis between the forward and backward sweep increased as RH increased, indicating the existence of capacitive effects and/or ionic charge transport in the hydrated hybrid film.⁵⁵

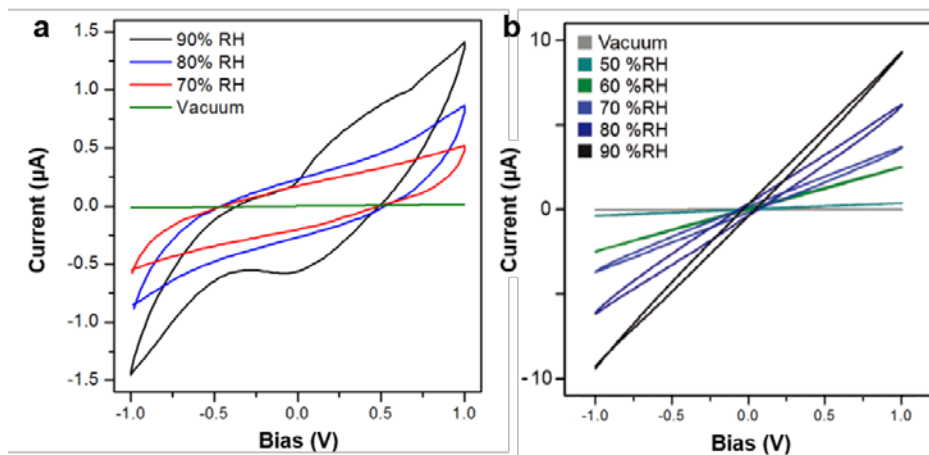


Figure 3.11 IV sweep plots (current versus voltage) of a peptide/manganese oxide hybrid film with (a) gold contacts and (b) PdH_x contacts as a function of humidity. The device had a length of 10 µm, a width of 1 mm and a thickness of 120 nm.

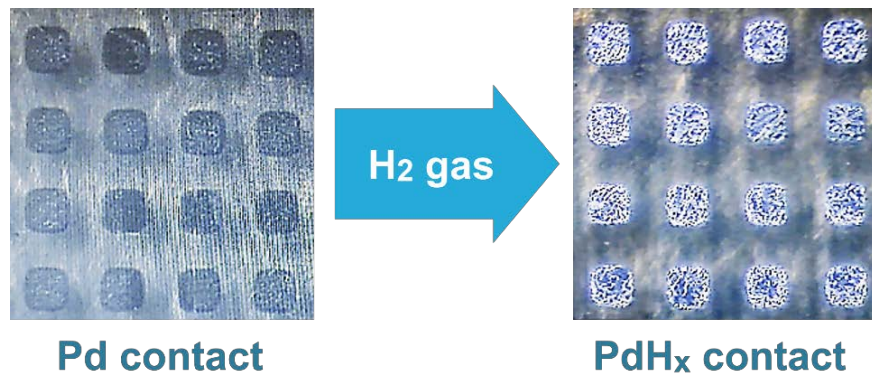


Figure 3.12 Upon IV measurement, the device was exposed to 5% H₂-balanced Ar gas, resulting in the formation of PdH_x electrical contacts *in situ*.

3.3.5 Electrochemical impedance spectroscopy analysis

We conducted electrochemical impedance spectroscopy (EIS) to precisely measure the ionic conductivity of the materials using two-electrode configuration with proton blocking gold contacts. To measure the impedance behaviour of the samples, alternating current (AC) was applied, and the obtained signals were represented in a complex-impedance-plane called a Nyquist plot (Figure 3.12). The Nyquist plot exhibited a semi-circle and an inclined tail, which is a typical shape of the impedance model for equivalent circuits proposed by Randle consisting of charge transfer resistance and a Warburg element.^{56,57} Such a shape of the graph is a characteristic of proton conductors contacted by an ion blocking electrode, in which the semi-circle curve at high frequencies represents the bulk resistance of the material, and the inclined line at low frequency corresponds to impedance arising from the accumulation of ions at the film/electrode interface.^{55,56} Indeed, the bulk conductivity of the hybrid film can be calculated by fitting the Nyquist plot to an resistor-capacitor circuit that is typically used for modelling proton exchange membranes (Figure 3.13).⁵⁸ As shown in Figure 3.14, the hybrid film exhibited a marked increase in its conductivity as RH increased, with the conductivity reaching $1.86 \times 10^{-2} \text{ S cm}^{-1}$ at 90% RH at 25 °C, which is a considerably high value in comparison with other values reported for proton-conducting materials

and bio-materials so far. These I-V and EIS measurement results implied that proton conduction was dominant in the hydrated hybrid film.

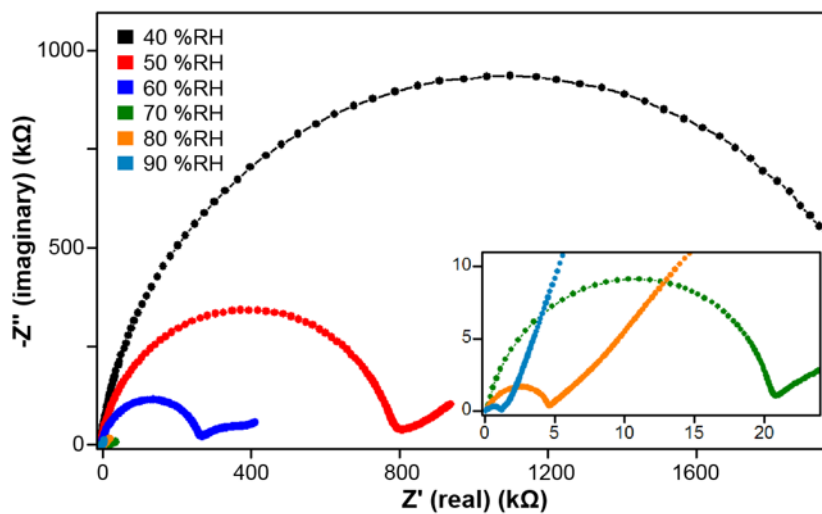


Figure 3.13 Typical Nyquist plots of the imaginary part of the impedance (Z'') versus the real part of the impedance (Z') by relative humidity for a gold electrode two-terminal device fabricated from peptide/manganese oxide hybrid material.

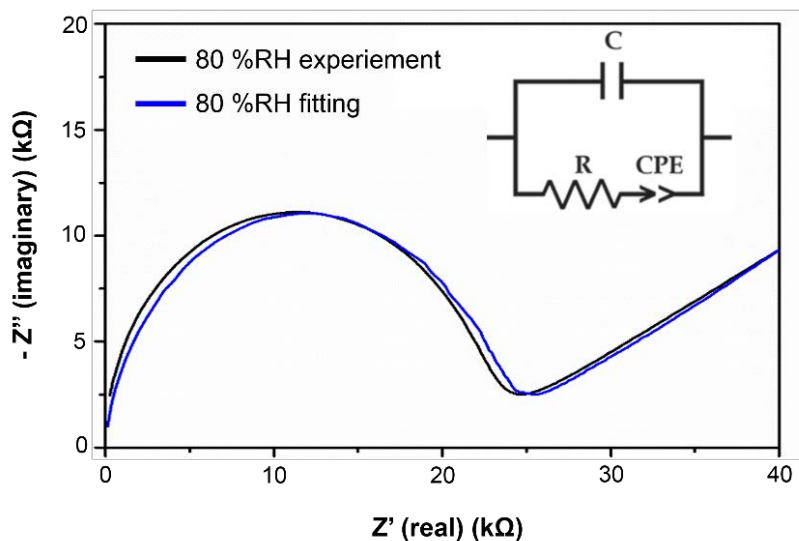


Figure 3.14 Nyquist plots acquired from impedance spectroscopy measurements. Blue line represent the fitting results obtained for the suggested equivalent circuit. (inset) Diagram of the equivalent circuit used to analyze the impedance data. R corresponds to the bulk resistance of the system, and the constant phase element (CPE) corresponding to a distributed capacitive contribution of the network indicates an imperfect dielectric behavior. The parallel capacitive term, C, is attributed to the film/electrode interface capacitance.

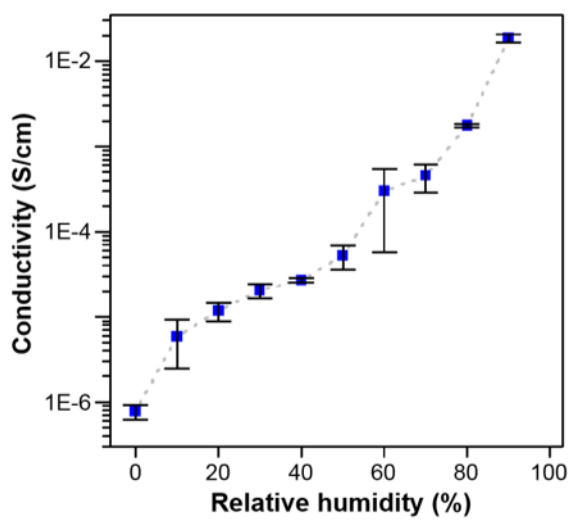


Figure 3.15 Calculated conductivity of the devices based on Nyquist plots by relative humidity.

3.3.6 Deuterium kinetic isotope effect on conductivity

For a better understanding of the origin of humidity-dependent conductivity, the deuterium (D) kinetic isotope effect (KIE) on the conductivity of the hybrid film was explored. The KIE on conductivity was measured using EIS in the presence of deuterium oxide (D₂O) vapour. As shown in Figure 3.15, we observed a distinct isotope effect, in which the conductivity of H₂O-humidified film was ~3.3 times higher than that of D₂O-humidified film at 80% RH. Such a large KIE value makes it clear that a vehicle mechanism where proton transport only occurs by hydronium diffusion cannot be operating because the ideal isotope effect of vehicle transport equals the viscosity ratio, ~1.2.⁵⁹ Instead, proton conduction may occur by the Grotthuss mechanism, consisting of proton hopping between neighbouring molecules in a hydrogen bond network accompanied by an additional reorganization of the proton solvating environment.⁶⁰ The theoretical KIE value of proton hopping is $\sqrt{2}$ according to classical theory, where the attempt frequency to overcome the energy barrier of hopping is dependent on the effective mass of the atom.^[46] Although the exact mechanism is still under debate, such deviation from the theoretical value can also be found in other literature about proton conductors working at room temperature.^{8,62,63} This kinetic isotope experiment shows that the main charge carriers of the hybrid film are protons from water vapour.

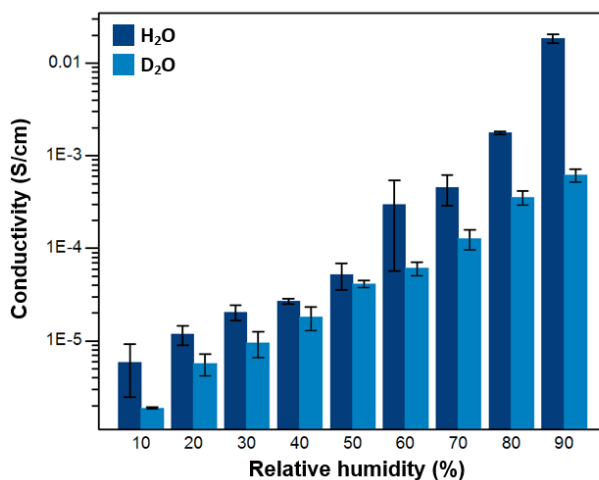
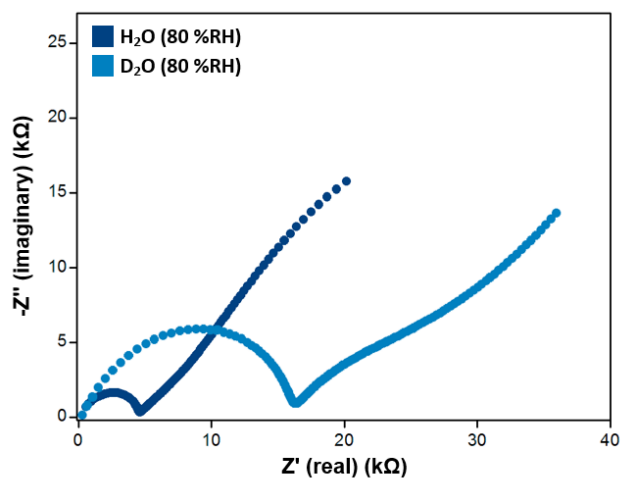


Figure 3.16 Nyquist plots in the presence of water vapor or deuterium oxide vapor (RH of 80%) and the calculated conductivity based on Nyquist plots by the relative humidity in presence of H₂O or D₂O vapor.

3.3.7 Transient current measurements

Transient current measurements were carried out to find direct evidence of proton accumulation at the electrode. The measurements were performed in two-terminal devices of hybrid film with gold contacts. The current was recorded by applying constant 150 mV bias for 5 minutes and turning off the bias for another 5 minutes sequentially (Figure 3.16a,b). At 80% RH conditions, when applying the bias the film showed initial current of 182 nA, and this was followed by a huge current drop in a few seconds. Then, only 1.3% of the initial current was maintained after 20 seconds. It was speculated that the formation of an electrical double layer from the protons blocked at the contact causes the current to rapidly decrease to 2.3 nA. Because gold contacts block ions, it can be inferred that a relatively high initial current would be originated from the motion of protons and capacitive charging at the electrodes. It is noteworthy that switching the bias to zero at a steady state resulted in an abrupt decrease of the current to -48 nA, followed by a rapid increase to -0.1 nA, displaying the transient response of an RC circuit. Unlike the results at a high degree of hydration, in a vacuum, only small constant current of 260 pA was obtained with applied bias, and no reverse current was observed after removing the bias. This behaviour reflected that protons were not piled up at the electrode, and the current came solely from electrons. Thus,

we can conclude that the accumulation of protons occurred upon exposure to continuous bias in humid conditions, and the relatively high current in the humid environment was attributed to the presence of proton carriers.

To decouple the contribution of protonic current from the mixed electrical properties of the hybrid film, the extent of proton contribution was estimated by transient current measurements with proton-permeable PdH_x contacts. Measurements were conducted at 90% RH with either gold or PdH_x contacts. As shown in Figure 3.16c, the steady-state current of the device with PdH_x contacts was enhanced by a factor of fifty over that of the device with gold contacts. By subtracting the steady-state current measured at 90% RH with PdH_x contacts from that with Au contacts, the proton conductivity can be calculated to be $3.4 \times 10^{-3} \text{ S cm}^{-1}$. This value is slightly lower but comparable to the conductivity measured by EIS ($1.86 \times 10^{-2} \text{ S cm}^{-1}$). Generally, differences between conductivity values from DC and EIS measurements arise from resistance of the contacts and time-dependent current drop in the PdH_x contacted device. Although PdH_x can inject and drain proton carriers, a transient current drop can occur when the diffusion of hydrogen to the PdH_x surface is slower than the proton conduction in the sample.⁹ Additionally, it was also observed that the extent of the steady state current increased with higher degrees of hydration, which is consistent with the results of AC measurement (Figure 3.16d). This is clear evidence that the protonic contribution to the

steady state current is increased at higher humidity, corresponding to the typical tendency of water-mediated proton-conducting materials.

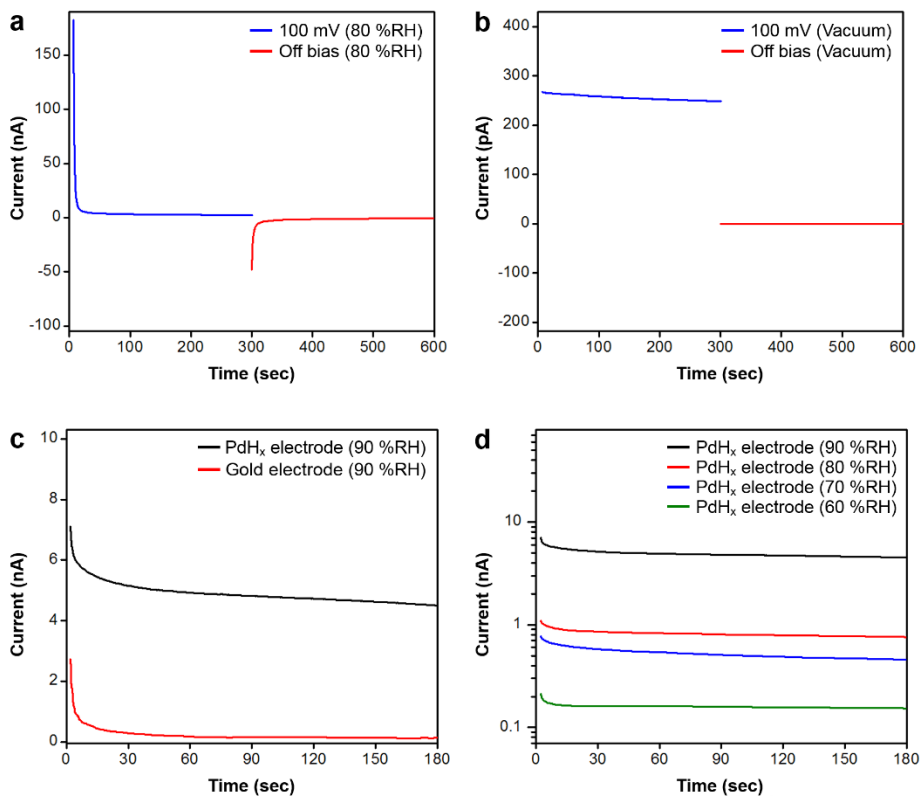


Figure 3.17 Transient current measurement of two-terminal devices. a,b) Comparison of the electrical characteristics of two-terminal devices fabricated from hybrid film. The current was recorded with constant 100 mV bias for 300 seconds and another 300 seconds with no bias. Transient current measurement of the devices with gold electrodes at 80% RH (a) and under vacuum (b). c) Transient current measurement of devices with PdH_x electrodes (black) and gold electrodes (red). d) Recorded current as a function of relative humidity with PdH_x electrodes.

3.3.8 Synergistic effect on proton conduction of peptide and manganese oxides

To understand how the peptide and manganese species interrelate when conduction occurs in the hybrid film, the roles of each component were investigated. To explore the role of MnO_x in the film, we controlled the concentration (10, 30, 50, 100 mM) of the KMnO_4 solution and the treatment time of the hybridization process. As a result, it was observed that higher concentration of the reactant solution and longer dipping time made the film thicker after the treatment (Figure 3.18), which indicated that more manganese oxide species were deposited on the film. However, the hybrid film almost dissolved when the concentration of KMnO_4 was 10 mM. The results indicated that the reaction inducing tyrosine crosslinking and manganese oxide formation also enhanced the adhesion and mechanical properties of the hybrid film. Thus, when the KMnO_4 concentration is lower than 10 mM, the hybrid film cannot maintain its structure and dissolves into the solution. The conductivity of the device with these films was measured with DC measurement, and the calculated values were plotted (Figure 3.19). As the reaction time and concentration of KMnO_4 increased, the conductivity of the hybrid film decreased (Figure 3.19). It is notable that the conductivity of the hybrid film at 90% RH is two orders of magnitude higher than that of pure peptide film. These results show that MnO_x

contributes significantly to increased proton conductivity at first, but it also leads to lower conductivity as the amount of MnO_x increases. To elucidate the contribution of the peptides to conductivity, we eliminated the peptides by an annealing process. The hybrid film was annealed at 400 °C, which was set from thermal gravimetric analysis (TGA) of the hybrid film (Figure 3.20) because it was a sufficiently high temperature to decompose the peptides while allowing MnO_x to remain without entailing a significant change in phase.⁶⁴⁻⁶⁷ During the annealing process, most of the peptide moieties combusted and the structural/surface water molecules in MnO_x were removed from the solid phase. In a comparison of conductivity with the original state, it was founded that the devices of annealed film lost the hydration dependence of their conductivity and showed increased conductivity of 0.7 S cm^{-1} (Figure 3.19). The results indicate that the major charge carriers in the hybrid film became electrons, and the contribution to total current from protons is negligible after eliminating the peptides. Thus, we think that the high proton conductivity of the hybrid film came from a synergistic effect of peptides and MnO_x .

Interestingly, the peptide sequence also affects the proton conductivity. To identify the role of tyrosine in proton conduction, YFACAFY, with fewer tyrosines than YYACAYY, was selected. We expected that if there was less tyrosine, lower amounts of crosslinked oxidized species and MnO_x would be formed, and the conversion of tyrosine into phenylalanine would reduce the hydrophilic hydroxyl groups, which can affect the hydrogen bonding network.

As shown in Figure 3.21, the device fabricated from YFACAFY sequence presents a current of 0.06 μA at 1 V and its conductivity is $2 \times 10^{-4} \text{ S cm}^{-1}$ at 80% RH calculated from impedance analysis, which is approximately an order of magnitude lower than that of the YYACAYY sequence. EDX mapping and cross-section TEM images of the YFACAFY-based hybrid film showed that manganese oxide also forms entirely inside of the film, which is similar to that of the YYACAYY sequence (Figure 3.22). However, the proton conductivity is much lower than that of YYACAYY-based hybrid film. This indicated that tyrosine plays an important role in proton conduction.

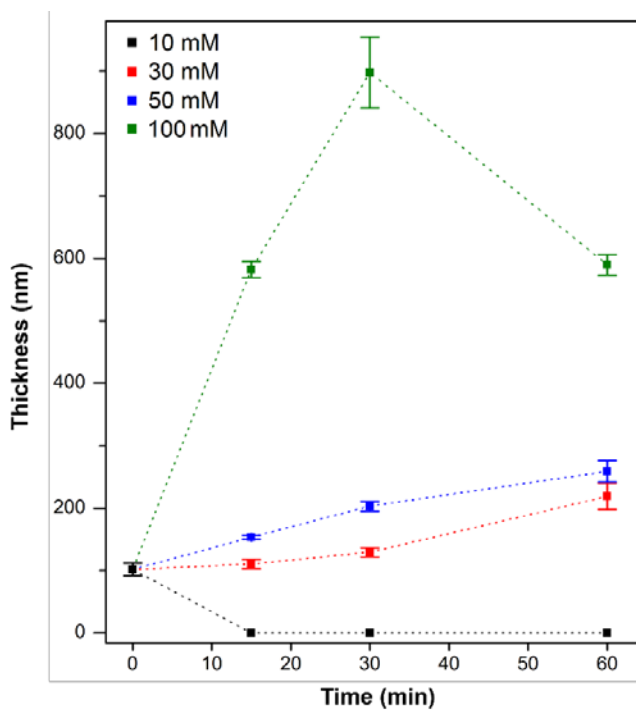


Figure 3.18 Thickness of pristine peptide films and hybrid films of various concentration of KMnO_4 solution by treatment time.

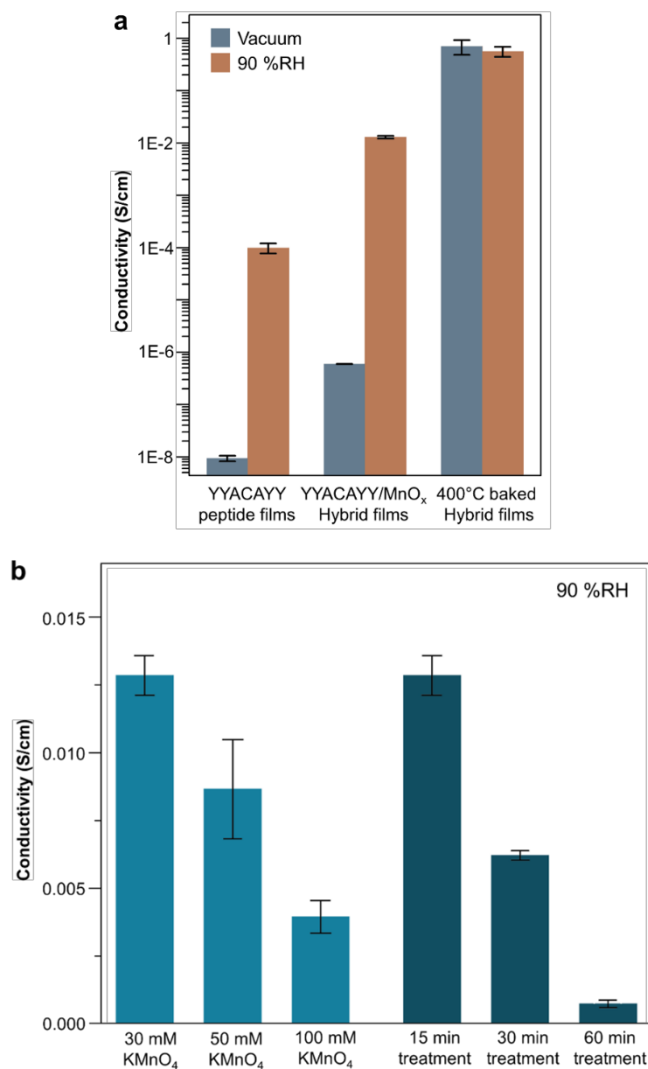


Figure 3.19 Conductivity differences of hybrid films. a) Conductivity chart for peptide film, hybrid film and 400 °C annealed film under vacuum (grey) or RH of 90% (brown). b) Conductivity comparison at RH of 90% and varying treatment conditions of KMnO₄. The conductivity was calculated from DC measurements.

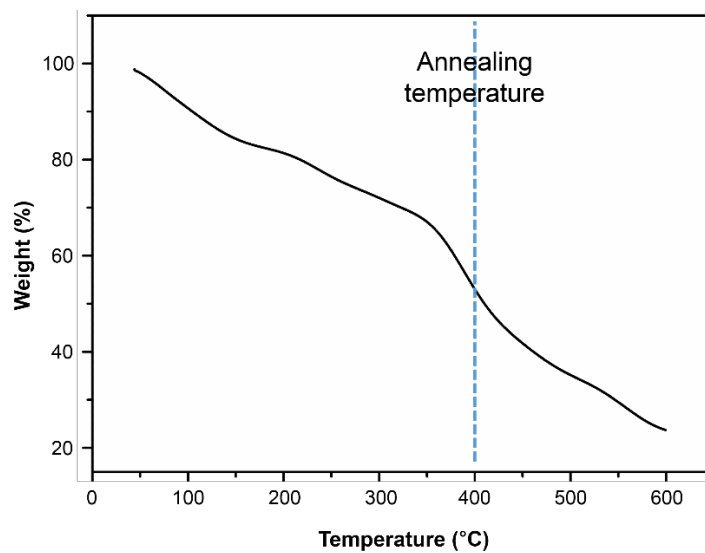


Figure 3.20 Thermal gravimetric analysis of the hybrid film in air condition.

Below 250°C, the hybrid film loses structural water and surface water.

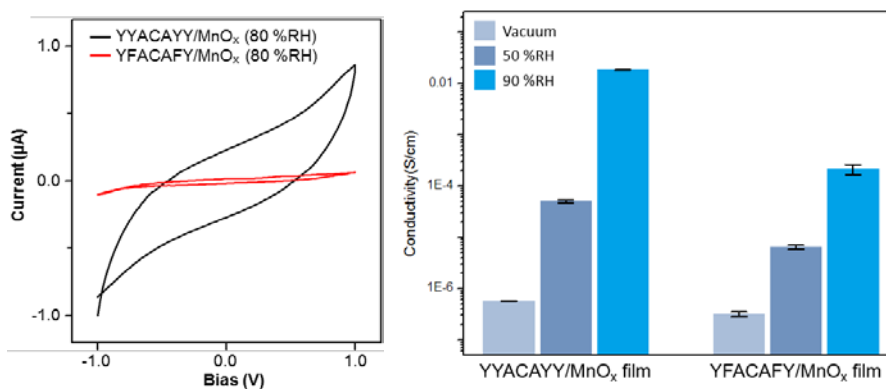


Figure 3.21 IV sweep plots of hybrid films from YYACAYY (black) and YFACAFY (red) peptides at 80 %RH. Calculated conductivity of hybrid films from YYACAYY or YFACAFY peptides through EIS measurements as a function of humidity

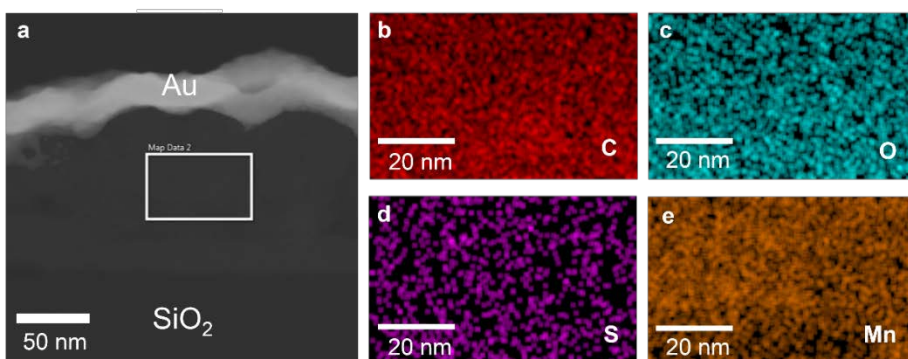


Figure 3.22 Cross-section TEM images and EDX mapping analysis of hybrid film synthesized with YFACAFY sequence peptide.

3.4 Conclusion

Such high proton conductivity for a peptide/MnO_x hybrid material is unprecedented even though it is reported that certain phases of manganese oxides and peptide/protein containing a large amount of carboxylic groups or hydrophilic moieties exhibit moderate proton conduction at room temperature. Comparison with literature data on low-temperature proton conductors showed that the conductivity of the peptide/MnO_x hybrid film is the highest among biomaterial-based proton conductors (Figure 3.23). The value is comparable to that of metal-organic frameworks, and it is only an order of magnitude lower than the proton conductivity of Nafion, the state-of-the-art proton conductor.

Considering the relatively high value (3.3) of the kinetic isotope effect on proton conductivity, there will be another pathway of proton translocation that is different from the conventional Grotthuss mechanism. Such high KIE values were observed when proton moves by PCET reaction or by tunnelling effect. These alternative pathways have never been reported for synthetic proton conductors, but the phenomena were usually observed in biological systems such as enzymes.^{74,75} Further study is required to understand the exact mechanism.

In summary, we have presented a new approach to proton conductors based on hybrid materials of peptides and manganese oxides. The peptide/MnO_x hybrid nanofilm can be synthesized by using a simple two-step

process at room temperature. The electrical properties of the hybrid film were investigated by I-V measurement, EIS, and transient current measurement. From the measurements, it turns out that the major charge carriers of the hybrid film were protons, and the proton conductivity reached $1.86 (\pm 0.20) \times 10^{-2} \text{ S cm}^{-1}$ at 90% RH. To the best of our knowledge, no other biomaterial-based proton conductor or manganese oxide has shown such high proton conductivity. Interestingly, the crosslinking and oxidation of tyrosine species simultaneously lead to hybridization with MnO_x , resulting in rather strong synergetic effects on proton conduction. Moreover, we predict that the proton conduction across the hybrid film could be further improved by incorporating more tyrosine groups or acidic functional groups into the peptide sequence. The exploration of peptide-based hybrid films as novel proton conductors has not been documented and has significant implications for both biology and technology. This study suggests that peptide-based hybrid films can be a promising new class of proton conductor.

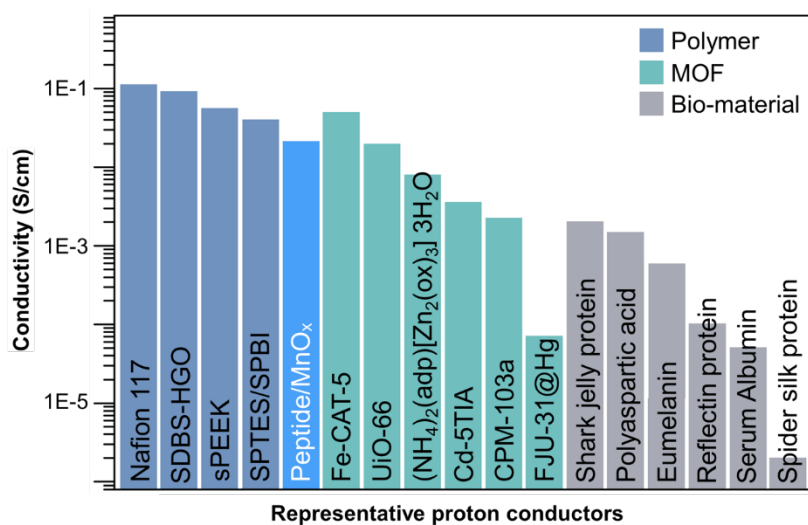


Figure 3.23 Comparison chart of proton conductivity of other representative proton conducting materials such as polymers^{24,54}, metal-organic framework (MOF)¹⁸⁻²³, and biomaterial^{8,9,11,71-73} at room temperature.

3.5 References

1. Pansini, A.; Guerrieri, F.; Papa, S. Control of Proton Conduction by the H⁺-ATPase in the Inner Mitochondrial Membrane. *Eur. J. Biochem.* **1978**, *92*, 545–551.
2. Lozier, R. H.; Bogomolni, R. A.; Stoerkenius, W. Bacteriorhodopsin: A Light Driven Proton Pump in Halobacterium Halobium. *Biophys. J.* **1975**, *15*, 955–962.
3. Tombola, F.; Ulbrich, M. H.; Isacoff, E. Y. The Voltage-Gated Proton Channel Hv1 Has Two Pores, Each Controlled by One Voltage Sensor. *Neuron* **2008**, *58*, 546–556.
4. Meyer, T. J.; Huynh, M. H. V; Thorp, H. H. The Possible Role of Proton-Coupled Electron Transfer (PCET) in Water Oxidation by Photosystem II. *Angew. Chemie - Int. Ed.* **2007**, *46*, 5284–5304.
5. Reichard, P.; Ehrenberg, A. Ribonucleotide Reductase--a Radical Enzyme. *Science* **1983**, *221*, 514–519.
6. Croce, R.; Amerongen, H. Van; van Amerongen, H.; Amerongen, H. Van. Natural Strategies for Photosynthetic Light Harvesting. *Nat. Chem. Biol.* **2014**, *10*, 492–501.
7. Zhong, C.; Deng, Y.; Roudsari, A. F.; Kapetanovic, A.; Anantram, M. P.; Rolandi, M. A Polysaccharide Bioprotonic Field-Effect Transistor. *Nat. Commun.* **2011**, *2*, 476.

8. Ordinario, D. D.; Phan, L.; Walkup Iv, W. G.; Jocson, J.-M.; Karshalev, E.; Hüskén, N.; Gorodetsky, A. a. Bulk Protonic Conductivity in a Cephalopod Structural Protein. *Nat. Chem.* **2014**, *6*, 596–602.
9. Josberger, E. E.; Hassanzadeh, P.; Deng, Y.; Sohn, J.; Rego, M. J.; Amemiya, C. T.; Rolandi, M. Proton Conductivity in Ampullae of Lorenzini Jelly. *Sci. Adv.* **2016**, *2*, e1600112–e1600112.
10. Mostert, a. B.; Powell, B. J.; Pratt, F. L.; Hanson, G. R.; Sarna, T.; Gentle, I. R.; Meredith, P. Role of Semiconductivity and Ion Transport in the Electrical Conduction of Melanin. *Proc. Natl. Acad. Sci.* **2012**, *109*, 8943–8947.
11. Wünsche, J.; Deng, Y.; Kumar, P.; Di Mauro, E.; Josberger, E.; Sayago, J.; Pezzella, A.; Soavi, F.; Cicoira, F.; Rolandi, M.; *et al.* Protonic and Electronic Transport in Hydrated Thin Films of the Pigment Eumelanin. *Chem. Mater.* **2015**, *27*, 436–442.
12. Kreuer, K.-D. Proton Conductivity: Materials and Applications. *Chem. Mater.* **1996**, *8*, 610–641.
13. Yu, N.; Yin, H.; Zhang, W.; Liu, Y.; Tang, Z.; Zhu, M. Q. High-Performance Fiber-Shaped All-Solid-State Asymmetric Supercapacitors Based on Ultrathin MnO₂ Nanosheet/Carbon Fiber Cathodes for Wearable Electronics. *Adv. Energy Mater.* **2016**, *6*, 1–9.
14. Paddison, S. J. Proton Conduction Mechanisms At Low Degrees of Hydration in Sulfonic Acid-Based Polymer Electrolyte Membranes.

- Annu. Rev. Mater. Res.* **2003**, *33*, 289–319.
15. Iwahara, H. Proton Conducting Ceramics and Their Applications. *Solid State Ionics* **1996**, *86–88*, 9–15.
 16. Uda, T.; Haile, S. M. Thin-Membrane Solid-Acid Fuel Cell. *Electrochem. Solid-State Lett.* **2005**, *8*, A245–A246.
 17. Boysen, D. a; Uda, T.; Chisholm, C. R. I.; Haile, S. M. High-Performance Solid Acid Fuel Cells through Humidity Stabilization. *Science* **2004**, *303*, 68–70.
 18. Nguyen, N. T. T.; Furukawa, H.; Gándara, F.; Trickett, C. A.; Jeong, H. M.; Cordova, K. E.; Yaghi, O. M. Three-Dimensional Metal-Catecholate Frameworks and Their Ultrahigh Proton Conductivity. *J. Am. Chem. Soc.* **2015**, *137*, 15394–15397.
 19. Phang, W. J.; Jo, H.; Lee, W. R.; Song, J. H.; Yoo, K.; Kim, B.; Hong, C. S. Superprotonic Conductivity of a Uio-66 Framework Functionalized with Sulfonic Acid Groups by Facile Postsynthetic Oxidation. *Angew. Chemie - Int. Ed.* **2015**, *54*, 5142–5146.
 20. Sadakiyo, M.; Yamada, T.; Kitagawa, H. Rational Designs for Highly Proton-Conductive Metal-Organic Frameworks. *J. Am. Chem. Soc.* **2009**, *131*, 9906–9907.
 21. Panda, T.; Kundu, T.; Banerjee, R. Self-Assembled One Dimensional Functionalized Metal–organic Nanotubes (MONTs) for Proton Conduction. *Chem. Commun.* **2012**, *48*, 5464–5466.

22. Zhai, Q. G.; Mao, C.; Zhao, X.; Lin, Q.; Bu, F.; Chen, X.; Bu, X.; Feng, P. Cooperative Crystallization of Heterometallic Indium-Chromium Metal-Organic Polyhedra and Their Fast Proton Conductivity. *Angew. Chemie - Int. Ed.* **2015**, *54*, 7886–7890.
23. Xiang, S.; Ye, Y.; Wu, X.; Yao, Z.-Z.; Wu, L.; Cai, Z.; Wang, L.; Ma, X.; Chen, Q.; Zhang, Z. Metal-Organic Frameworks with Large Breathing Effect to Host Hydroxyl Compounds for High Anhydrous Proton Conductivity over a Wide Temperature Range from Subzero to 125 OC. *J. Mater. Chem. A* **2016**, *4*, 4062–4070.
24. Liu, L.; Chen, W.; Li, Y. An Overview of the Proton Conductivity of Nafion Membranes through a Statistical Analysis. *J. Memb. Sci.* **2016**, *504*, 1–9.
25. Shao, Z. G.; Xu, H.; Li, M.; Hsing, I. M. Hybrid Nafion-Inorganic Oxides Membrane Doped with Heteropolyacids for High Temperature Operation of Proton Exchange Membrane Fuel Cell. *Solid State Ionics* **2006**, *177*, 779–785.
26. Sahu, a. K.; Selvarani, G.; Pitchumani, S.; Sridhar, P.; Shukla, a. K. A Sol-Gel Modified Alternative Nafion-Silica Composite Membrane for Polymer Electrolyte Fuel Cells. *J. Electrochem. Soc.* **2007**, *154*, B123.
27. Saccà, A.; Carbone, A.; Passalacqua, E.; D'Epifanio, A.; Licoccia, S.; Traversa, E.; Sala, E.; Traini, F.; Ornelas, R. Nafion-TiO₂ Hybrid Membranes for Medium Temperature Polymer Electrolyte Fuel Cells

- (PEFCs). *J. Power Sources* **2005**, *152*, 16–21.
28. Mistry, M. K.; Choudhury, N. R.; Dutta, N. K.; Knott, R.; Shi, Z.; Holdcroft, S. Novel Organic - Inorganic Hybrids with Increased Water Retention for Elevated Temperature Proton Exchange Membrane Application. *Chem. Mater.* **2008**, *20*, 6857–6870.
29. McKeen, J. C.; Yan, Y. S.; Davis, M. E. Proton Conductivity of Acid-Functionalized Zeolite Beta, MCM-41, and MCM-48: Effect of Add Strength. *Chem. Mater.* **2008**, *20*, 5122–5124.
30. Zheng, J.; Wu, Y.; Deng, K.; He, M.; He, L.; Cao, J.; Zhang, X.; Liu, Y.; Li, S.; Tang, Z. Chirality-Discriminated Conductivity of Metal-Amino Acid Biocoordination Polymer Nanowires. *ACS Nano* **2016**, *10*, 8564–8570.
31. Qin, B.; Chen, H.; Liang, H.; Fu, L.; Liu, X.; Qiu, X.; Liu, S.; Song, R.; Tang, Z. Reversible Photoswitchable Fluorescence in Thin Films of Inorganic Nanoparticle and Polyoxometalate Assemblies. *J. Am. Chem. Soc.* **2010**, *132*, 2886–2888.
32. Yachandra, V. K.; Sauer, K.; Klein, M. P. Manganese Cluster in Photosynthesis: Where Plants Oxidize Water to Dioxygen. *Chem. Rev.* **1996**, *96*, 2927–2950.
33. Stubbe, J. Di-Iron-Tyrosyl Radical Ribonucleotide Reductases. *Curr. Opin. Chem. Biol.* **2003**, *7*, 183–188.
34. Riley, P. A. Melanin. *Int. J. Biochem. Cell Biol.* **1997**, *29*, 1235–1239.

35. Jang, H.-S.; Lee, J.-H.; Park, Y.-S.; Kim, Y.-O.; Park, J.; Yang, T.-Y.; Jin, K.; Lee, J.; Park, S.; You, J. M.; *et al.* Tyrosine-Mediated Two-Dimensional Peptide Assembly and Its Role as a Bio-Inspired Catalytic Scaffold. *Nat. Commun.* **2014**, *5*, 3665.
36. Zheng, J.; Wu, Y.; Deng, K.; He, M.; He, L.; Cao, J.; Zhang, X.; Liu, Y.; Li, S.; Tang, Z. Chirality-Discriminated Conductivity of Metal-Amino Acid Biocoordination Polymer Nanowires. *ACS Nano* **2016**, *10*, 8564–8570.
37. Tang, Q.; Jiang, L.; Liu, J.; Wang, S.; Sun, G. Effect of Surface Manganese Valence of Manganese Oxides on the Activity of the Oxygen Reduction Reaction in Alkaline Media. *ACS Catal.* **2014**.
38. Huang, K. C.; Hoag, G. E.; Chheda, P.; Woody, B. A.; Dobbs, G. M. Kinetics and Mechanism of Oxidation of Tetrachloroethylene with Permanganate. *Chemosphere* **2002**, *46*, 815–825.
39. Krapcho, a. P.; Larson, J. R.; Eldridge, J. M. Potassium Permanganate Oxidations of Terminal Olefins and Acetylenes to Carboxylic Acids of One Less Carbon. *J. Org. Chem.* **1977**, *42*, 3749–3753.
40. Huang, X.; Yue, H.; Attia, A.; Yang, Y. Preparation and Properties of Manganese Oxide/Carbon Composites by Reduction of Potassium Permanganate with Acetylene Black. *J. Electrochem. Soc.* **2007**, *154*, A26.
41. Jacob, J. S.; Cistola, D. P.; Hsu, F. F.; Muzaffar, S.; Mueller, D. M.;

- Hazen, S. L.; Heinecke, J. W. Human Phagocytes Employ the Myeloperoxidase-Hydrogen Peroxide System to Synthesize Dityrosine, Trityrosine, Pulcherosine, and Isodityrosine by a Tyrosyl Radical-Dependent Pathway. *J. Biol. Chem.* **1996**, *271*, 19950–19956.
42. Winterbourn, C. C.; Parsons-Mair, H. N.; Gebicki, S.; Gebicki, J. M.; Davies, M. J. Requirements for Superoxide-Dependent Tyrosine Hydroperoxide Formation in Peptides. *Biochem. J.* **2004**, *381*, 241–248.
43. Malik, M. A.; Basahel, S. N.; Obaid, A. Y.; Khan, Z. Oxidation of Tyrosine by Permanganate in Presence of Cetyltrimethylammonium Bromide. *Colloids Surfaces B Biointerfaces* **2010**, *76*, 346–353.
44. Goodwin, T. W.; Morton, R. A. The Spectrophotometric Determination of Tyrosine and Tryptophan in Proteins. *Biochem J* **1946**, *40*, 628–632.
45. Suzuki, H. *Electronic Absorption Spectra and Geometry of Organic Molecules: An Application of Molecular Orbital Theory*, Elsevier, **2012**
46. Kalsi, P. S. *Spectroscopy of Organic Compounds*, New Age International, **2007**.
47. Barakat, N. A. M.; Woo, K. Do; Ansari, S. G.; Ko, J. A.; Kanjwal, M. A.; Kim, H. Y. Preparation of Nanofibers Consisting of MnO/Mn₃O₄ by Using the Electrospinning Technique: The Nanofibers Have Two Band-Gap Energies. *Appl. Phys. A Mater. Sci. Process.* **2009**, *95*, 769–776.
48. Jin, K.; Seo, H.; Hayashi, T.; Balamurugan, M.; Jeong, D.; Go, Y. K.;

- Hong, J. S.; Cho, K. H.; Kakizaki, H.; Bonnet-Mercier, N.; *et al.* Mechanistic Investigation of Water Oxidation Catalyzed by Uniform, Assembled MnO Nanoparticles. *J. Am. Chem. Soc.* **2016**, *139*, 2277–2285.
49. Wells, C. F.; Davies, G. A Spectrophotometric Investigation of the Aquomanganese (III) Ion in Perchlorate Media. *J. Chem. Soc. A Inorganic, Phys. Theor.* **1967**, 1858–1861.
50. hua Yu, W.; hui Zhou, C.; shen Tong, D.; ning Xu, T. Aerobic Oxidation of 4-Tert-Butyltoluene over Cobalt and Manganese Supported Hexagonal Mesoporous Silicas as Heterogeneous Catalysts. *J. Mol. Catal. A Chem.* **2012**, *365*, 194–202.
51. Nevin, A.; Cather, S.; Anglos, D.; Fotakis, C. Analysis of Protein-Based Binding Media Found in Paintings Using Laser Induced Fluorescence Spectroscopy. *Anal. Chim. Acta* **2006**, *573–574*, 341–346.
52. Heineckes, J. W.; Li, W.; Daehnke, H. L.; Goldstein, J. A. Dityrosine, a Specific Marker of Oxidation,. **1993**, 202.
53. Yoon, Y.-G.; Pyun, S.-I. Hydrogen Transport through Pd Electrode: Current Transient Analysis. *Electrochim. Acta* **1997**, *42*, 1701–1708.
54. Morgan, H.; Pethig, R.; Stevens, G. T. A Proton-Injecting Technique for the Measurement of Hydration-Dependent Protonic Conductivity. *J. Phys. E.* **1986**, *19*, 80.
55. Barsoukov, B.; Macdonald, J. R. *Impedance Spectroscopy: Theory*,

Experiment, and Applications, John Wiley & Sons, **2005**.

56. Huggins, R. a. Simple Method to Determine Electronic and Ionic Components of the Conductivity in Mixed Conductors a Review. *Ionics* **2002**, 8, 300–313.
57. Taylor, S. R.; Gileadi, E. Physical Interpretation of the Warburg Impedance. *Corrosion* **1995**, 51, 664–671.
58. Garrido, L.; López-González, M.; Tlenkopatchev, M.; Riande, E. Proton Diffusion in Polyelectrolytes Based on Hydrogenated Polynorbornenes with Imide Side Groups in the Repeat Unit as Determined by NMR and Impedance Spectroscopies. *J. Memb. Sci.* **2011**, 380, 199–207.
59. Davis, C. M.; Jarzynski, J. Liquid Water—Acoustic Properties: Absorption and Relaxation. In *The Physics and Physical Chemistry of Water*; Springer New York: Boston, MA, **1972**; 443–461.
60. Agmon, N. The Grotthuss Mechanism. *Chem. Phys. Lett.* **1995**, 244, 456–462.
61. Bonanos, N.; Huijser, A.; Poulsen, F. W. H/D Isotope Effects in High Temperature Proton Conductors. *Solid State Ionics* **2015**, 275, 9–13.
62. Karim, M. R.; Hatakeyama, K.; Matsui, T.; Takehira, H.; Taniguchi, T.; Koinuma, M.; Matsumoto, Y.; Akutagawa, T.; Nakamura, T.; Noro, S.; *et al.* Graphene Oxide Nanosheet with High Proton Conductivity. *J. Am. Chem. Soc.* **2013**, 135, 8097–8100.
63. Nagao, Y.; Matsui, J.; Abe, T.; Hiramatsu, H.; Yamamoto, H.; Miyashita,

- T.; Sata, N.; Yugami, H. Enhancement of Proton Transport in an Oriented Polypeptide Thin Film. *Langmuir* **2013**, *29*, 6798–6804.
64. Cho, S. Y.; Yun, Y. S.; Lee, S.; Jang, D.; Park, K.-Y.; Kim, J. K.; Kim, B. H.; Kang, K.; Kaplan, D. L.; Jin, H.-J. Carbonization of a Stable β -Sheet-Rich Silk Protein into a Pseudographitic Pyroprotein. *Nat. Commun.* **2015**, *6*, 7145.
65. Amdursky, N.; Beker, P.; Koren, I.; Bank-Srouer, B.; Mishina, E.; Semin, S.; Rasing, T.; Rosenberg, Y.; Barkay, Z.; Gazit, E.; *et al.* Structural Transition in Peptide Nanotubes. *Biomacromolecules* **2011**, *12*, 1349–1354.
66. Mattelaer, F.; Bosserez, T.; Martens, J. A.; Dendooven, J.; Detavernier, C. Manganese Oxide Films with Controlled Oxidation State for Water Splitting Devices through a Combination of Atomic Layer Deposition and Post-Deposition Annealing. *RSC Adv.* **2016**, *6*, 98337–98343.
67. Ruetschi, P.; Giovanoli, R. Cation Vacancies in MnO₂ and Their Influence on Electrochemical Reactivity. *J. Electrochem. Soc.* **1988**, *135*, 2663–2669.
68. Jiang, Z.; Shi, Y.; Jiang, Z.-J.; Tian, X.; Luo, L.; Chen, W. High Performance of a Free-Standing Sulfonic Acid Functionalized Holey Graphene Oxide Paper as a Proton Conducting Polymer Electrolyte for Air-Breathing Direct Methanol Fuel Cells. *J. Mater. Chem. A* **2014**, *2*, 6494.

69. Wang, R.; Wu, X.; Yan, X.; He, G.; Hu, Z. Proton Conductivity Enhancement of SPEEK Membrane through N-BuOH Assisted Self-Organization. *J. Memb. Sci.* **2015**, *479*, 46–54.
70. Dong, B.; Wang, Y.; Pang, J.; Guan, S.; Jiang, Z. High Proton Conductivity of Sulfonated Methoxyphenyl-Containing Poly(Arylene Ether Ketone) for Proton Exchange Membranes. *RSC Adv.* **2015**, *5*, 107982–107991.
71. Nagao, Y.; Kubo, T. Surface Proton Transport of Fully Protonated Poly(Aspartic Acid) Thin Films on Quartz Substrates. *Appl. Surf. Sci.* **2014**, *323*, 19–24.
72. Amdursky, N.; Wang, X.; Meredith, P.; Bradley, D. D. C.; Stevens, M. M. Long-Range Proton Conduction across Free-Standing Serum Albumin Mats. *Adv. Mater.* **2016**, *28*, 2692–2698.
73. Steven, E.; Park, J. G.; Paravastu, A.; Lopes, E. B.; Brooks, J. S.; Englander, O.; Siegrist, T.; Kaner, P.; Alamo, R. G. Physical Characterization of Functionalized Spider Silk: Electronic and Sensing Properties. *Sci. Technol. Adv. Mater.* **2011**, *12*, 055002.
74. Roston, D.; Islam, Z.; Kohen, A. Kinetic Isotope Effects as a Probe of Hydrogen Transfers to and from Common Enzymatic Cofactors. *Arch. Biochem. Biophys.* **2014**, *544*, 96–104.
75. Salna, B.; Benabbas, A.; Sage, J. T.; van Thor, J.; Champion, P. M. Wide-Dynamic-Range Kinetic Investigations of Deep Proton

Tunnelling in Proteins. *Nat. Chem.* **2016**, *8*, 874–880.

Chapter 4. Concluding remarks

One of the important challenges in the development of protein-mimetic materials is understanding the sequence specific assembly behavior and dynamic folding change. Conventional strategies for constructing two-dimensional (2D) nanostructures from peptides have been limited to using β -sheet forming sequences as building blocks due to their natural tendency to form sheet-like aggregations. In Chapter 2, we have identified a new peptide sequence (YFCFY) that can form dimers via a disulfide bridge, fold into a helix and assemble into macroscopic flat sheets at the air/water interface. Due to the large driving force for 2D assembly and high elastic modulus of the resulting sheet, the peptide assembly induces flattening of the initially round water droplet. We found that the disulfide bond between the monomers stabilizes the helical conformation, resulting in strong molecular interactions and reinforced mechanical strength of the assembled structure. It was a key determinant for maintaining macroscopic flatness over a few tens of centimeters even with a uniform thickness of less than 10 nm. In an effort to expand the 2D peptide assembly system and further hybridize with gold nanoparticles, we introduced redox-mediated 2D assembly using Au^{3+} , which can induce disulfide bonds and be reduced by tyrosine and cysteine. At first, Au^{3+} rapidly oxidizes cysteine to form disulfide bonded peptide while it is reduced to Au^{1+} . Simultaneously, the dimer peptide assembles into 2D nanosheets at the air/water interface and

oxidative phenolic groups in tyrosine produce gold nanoparticles adsorbed onto the peptide sheets. This study shed light on the peptide sequence-encoded assembly ability that the control of the folding nature can induce very stable 2D nanostructure even with helical peptides. Furthermore, the ability to transfer the sheets from a water droplet to another substrate allows for multiple stacking of 2D peptide nanostructures, suggesting possible applications in biomimetic catalysis, biosensors, and 2D related electronic devices.

In Chapter 3, we focus on a short tyrosine-rich peptide (YYACAYY) that has redox-active and cross-linkable phenol groups. Tyrosine is known to play a critical role in proton-coupled electron transfer, interacting with metal clusters in reaction centres. Additionally, eumelanin, a natural proton-electron mixed conductor, is synthesized from the oxidation reaction of tyrosine. Inspired by this attractive feature of tyrosine, a new hybrid proton conductor was synthesized and its superb proton conductivity was evaluated. The spin-coated peptide nanofilm is immersed into potassium permanganate solution to induce crosslinking and oxidation, simultaneously leading to hybridization with manganese oxide (MnO_x). Surprisingly, our new peptide-based hybrid material exhibits the best proton conductivity of 18.6 mS cm^{-1} , which is at least 100 times higher than the recently reported value of biomaterials, and the value is comparable to the highest proton conductivity of metal organic frameworks and covalent organic framework. Our new peptide-based hybrid material is a remarkable example of biomimicry, as the proton conduction in the hybrid film

mimics many of the fundamental principles found in biological processes.

- (a) Specific peptide sequence – when protons move over a significant distance, the process necessarily involves many elementary proton transfer steps and needs a significant structural component or path. Bio-systems utilize specific peptide sequences to construct exquisite proton transport channels.
- (b) Active centre of an enzyme – during enzymatic catalysis, a metal ion and neighbouring peptide moiety cooperatively deliver an electron and proton simultaneously.

Therefore, this work stands as a remarkable experimental demonstration of generating future proton-conducting materials. We think that it provides important insight into proton conduction in biological systems where tyrosine and metal ions work in cooperation within enzymes and membranes. This work also lays the foundation for a new class of sequence-specific peptide hybrid materials.

The significant meaning of this research is the construction of tyrosine peptide-based 2D nanomaterials and the possibility of extension to a variety of biomimetic scaffold with atomically defined structure. Scientifically, it provides an importance to understand the dynamic conformation and electrochemical behavior of tyrosine-rich short peptide in the aqueous solution and the air/water interface. The conducted research would advance my understanding how the short peptide can alter the folding structure depending

on the environment and interact with metal ions. This understanding would allow development of tyrosine-based hybrid materials with unique and highly tunable properties with broad applications.

국 문 초 록

단백질 기반의 생체 모방 재료를 연구함에 있어서 가장 중요한 주제 중 하나는 단백질의 구성 요소인 펩타이드의 서열에 따른 접힘 구조와 그로부터 결정되는 단백질의 3차 구조의 기능을 이해하여 짧은 펩타이드의 서열특이적 구조로부터 독특한 기능을 유도하는 일이다. 본 연구에서는 자연계에서 전자전달 및 단백질의 구조 형성에 매우 중요한 역할을 하고 있는 아미노산인 타이로신과 페닐알라닌을 기반으로 아미노산 5개 길이의 펩타이드를 디자인하여 대면적 2차원 자기조립 구조를 유도하고자 하였다. YFCFY 서열의 펩타이드는 물방울 표면에서 높은 탄성계수를 갖는 10 nm 두께의 균일한 나노시트를 형성하였고, 이 자기조립 구조체는 다양한 기판에 옮겨질 수 있음을 확인하였다. 이러한 자기 조립 구조체는 나선형 구조를 단위체로 구성되었으며 이는 시스테인의 이황화결합에 의한 생성된 이합체의 접힘구조의 안정화로 인해 가능하였다. 또한 펩타이드에 금 이온을 도입함으로써 공기/물 계면에서 금 나노 입자로 장식된 거대한 하이브리드 나노 시트를 만들었다. 사실, 펩타이드 자체가 가지고 있는 카이랄 성질로 인하여 펩타이드 기반 시스템에서 평평하고 매우 얇은 대면적 2 차원 자기조립 구조를 구현하는 것은 근본적으로 어려운 문제이다. 지금까지 펩타이드 기반 2 차원 자기조립 구조를 형성하기 위하여 사용한 접근법의 대부분은 베타 시트와 같은 단위 조립체 또는 얽힌 섬유 집합 구조를 기반으로 하였던 것도 위와 같은 맥락이다. 하지만 이 연구를 통해 이황화결합으로 나선형 구조를 안정화시킨 짧은 펩타이드를 이용하여 대면적 2 차원 자기조립 구조를 구현할 수 있음을 밝혔고 이는 추후 펩타이드 재료 연구에 큰 기여가 될 것이라고 생각된다.

더 나아가 산화 환원 활성 기능을 갖는 티이로신이 풍부한 펩타이드의 기능성을 조사하기 위해 우리는 망간 산화물과 하이브리드화된 펩타이드 필름의 수소이온전도성을 조사하였다. 생체 시스템에서 수소이온전도는 근본적인 생명 메커니즘을 이해하기 위해 매우 중요한 문제이다. 이러한 생체 시스템에서 수소이온전도를 이해하고 이를 사용하기 위해 최근 다양한 생체 기반 물질의 수소이온전도도가 측정되어왔다. 그러나 펩타이드 재료의 전도도 및 이들의 서열 특이적 행동에 대해서는 거의 알려지지 않았다. 본 연구에서는 산화 환원 활성 및 가교성 폐놀을 가진 티이로신이 풍부한 펩타이드에 중점을 두어 연구를 진행하였다. 티이로신은 광계2에서 칼슘-망간 클러스터와 상호 작용하여 전자와 수소이온을 동시에 전달하는 중요한 역할을 하는 것으로 알려져 있다. 또한 수화 정도에 따라 반도체와 유사한 거동을 보이는 가교 결합된 폴리머인 멜라닌으로 중합될 수 있다. 이로부터 우리는 티이로신 산화 반응을 통해 망간 산화물과 하이브리드 화하여 2차원 수소이온전도체를 만들었습니다. 펩타이드/망간 산화물 하이브리드 필름은 효율적으로 수소이온을 전달할 수 있었으며 수소이온전도도는 18.6 mS/cm 이었다. 이 값은 기존 보고된 생체 재료보다 훨씬 높은 수치이며 최근 보고되고 있는 합성 재료인 금속유기 골격체와 비슷한 수준이다. 이러한 결과는 펩타이드 기반 하이브리드 재료가 새로운 수소이온전도체로 충분히 사용될 수 있음을 시사한다. 생물 전자 공학 및 추가 응용의 관점에서 볼 때 이는 생체 적합 물질을 갖는 생체 기능 소자를 위한 다용도 플랫폼을 설계하는 좋은 예가 될 것이다. 위와 같은 일련의 연구를 통하여 본 연구에서는 통상적인 티이로신의 역할로 알려져 있는 자기조립 모티프와 자연계에서 전자와 수소이온을 전

달하는 매개체로써 타이로신의 역할이 결합될 수 있다는 것을 보여 주었다.